
Decay pathways of atomic and small
molecular ions after visible or extreme
ultraviolet photoabsorption



PhD Dissertation

Lasse Sloth Harbo
Aarhus University
May, 2015

Preface

This dissertation has been submitted to the Graduate School of Science and Technology at Aarhus University in order to fulfill the requirements for obtaining a PhD degree in Physics. The work has been carried out under supervision of associated professor Henrik B. Pedersen at the Department of Physics and Astronomy, Aarhus University.

Acknowledgements

First and foremost I would like to thank Henrik B. Pedersen for his support and guidance. He has been an great supervisor ever since I started in the research group as a bachelor student. His extensive knowledge and memory of various details is amazing. I really appreciate all your constructive proposals for improving methods, figures and text, despite the hassle of the actual implementation. Your strive for perfection and efficiency is inspiring.

During my PhD study I have shared office space with several people and I would like to thank all of you for our fruitful discussions and, not least of all, the needed breaks during the day with random small talk.

The experiments at FLASH during my PhD study could not have been performed without the staff at DESY. I want especially to thank Siarhei Dziarzhyski, Natalia Guerassimova, Günter Brenner and Holger Weigelt for the assistance during beam times and for lending a hand when old

parts were exchanged or new parts were installed. Your ability to always find a solution, a missing gasket or have a part, that just did not fit where it was supposed to, machined on the fly is amazing.

During my PhD study I had the pleasure to visit the group of Uwe Hergenhahn in Berlin, Germany. I gained valuable insight into the research of another group and I was impressed with the swiftness and feasibility of doing electron spectroscopy from a neutral gas jet at a synchrotron radiation source. It gave me a new perspective on doing electron spectroscopy under FEL conditions. I would like to thank both Uwe and Marko Förstel for the interesting and rewarding stay.

I would like to thank Karin Vittrup and Peter Harbo for proofreading my dissertation.

Finally, I would like to thank my daughter and wife, Laura and Helene, for your patience, understanding and support during my study.

I acknowledge and express my gratitude for the financial support from the Lundbeck foundation and the Graduate School of Science and Technology (Aarhus university).

Dansk resume

In denne afhandling beskrives henfaldskanalerne for anslåede tilstande i tre forskellige ioner: Oxygen anionen (O^-), Vandkationen (H_2O^+) og den protonerede vand dimer ($H_5O_2^+$). I alle tre tilfælde er ionerne blevet anslået ved fotoabsorption og eksperimenterne er foretaget ved TIFF opstillingen, der er placeret som en endestation ved fri elektron laseren, FLASH, i Hamborg, Tyskland.

TIFF opstillingen består af elektronspektrometre, ionfælder og hurtige, positions- og tidsfølsomme detektorer, så elektroner og positive, neutral og negative partikler kan detekteres samtidig.

Den store tæthed af fotoner fra FLASH i det ekstremt ultraviolette område giver en høj reaktionssandsynlighed for hver fotonpuls, selv i en krydset beamgeometri med en lille strøm af ioner i gasfasen ($I_{\text{Ion}} = 1 - 50\text{nA}$).

Kombinationen af TIFF og FLASH har gjort det muligt at studere både enkelt og dobbelt ionisation fra oxygen anionen ved $\lambda = 41.7\text{nm}$ i samme forsøg og bestemme det relative tværsnit til:

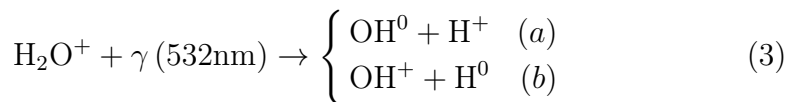
$$\frac{\sigma_{O^0}}{\sigma_{O^+}} = 4.12 \pm 0.17, \quad (1)$$

mens det absolutte tværsnit for enkelt ionisation er blevet bestemt til:

$$\sigma_{O^0} = 2.1 \pm 0.6 \cdot 10^{-19} \text{cm}^2. \quad (2)$$

Målinger af fotoelektroner og neutralt oxygen i koincidens indikerer, at oxygen ender i de mindst anslåede tilstande, O^0 (3P og 1D).

Efter enkelt fotoabsorption i vandkationen (H_2O^+) ved $\lambda = 532\text{nm}$, er det blevet fastslået at en dissociation finder sted fra de laveste, vibrationelle tilstande i $\tilde{B} \ ^2B_2$ tilstanden, og to åbne kanaler er blevet fundet:



Forgreningsforholdet mellem disse er blevet bestemt til

$$\frac{\sigma_a}{\sigma_b} = 1.3 \pm 0.3. \quad (4)$$

Ved at aktivere en ionfælde er levetiden af kanal (a) blevet bestemt til at være $\tau_{\tilde{B} \ 2B_2} = 198 \pm 11 \mu\text{s}$.

Ved fotofragmentering af H_5O_2^+ ved $\lambda = 42.1\text{nm}$ er forgreningsforholdet mellem 10 aktive kanaler blevet bestemt og for den kraftigste er den frigjorte kinetiske energy blevet bestemt til:

$$E_{\text{KER}}(\text{H}_5\text{O}_2^{2+} \rightarrow \text{H}_3\text{O}^+ + \text{H}_2\text{O}^+) = 1.8 \pm 0.5\text{eV}. \quad (5)$$

Contents

Preface	i
Acknowledgements	i
Dansk resume	iii
1 Introduction	1
2 Theoretical foundation	5
2.1 Introduction to molecular physics	5
2.2 Photoabsorption	13
2.3 Photoionization	16
2.4 Fragmentation of small molecules	18
2.5 The fast ion beam technique	19
3 Experimental setup	23
3.1 The ion source	25
3.2 Ion beam guidance	26
3.3 Mass separation	28
3.4 Ion trap	28
3.5 The interaction region	30
3.6 Electron spectrometer	32
3.7 The detection region	33
3.8 Free Electron Laser in Hamburg	34

3.9	Nd:YAG laser system	37
4	Data acquisition and analysis	39
4.1	Particle and photon detection	39
4.2	Digitalization	42
4.3	Sorting impact times	44
4.4	Experimental scheme	47
5	Coincidence analysis	49
5.1	Analysis scheme	50
5.2	Proof of concept	52
5.3	Discussion	57
6	Simulations	59
6.1	SIMION	59
6.2	Fragmentation reactions in SIMION	60
6.3	4π electrons to one detector	62
6.4	DET3: KER and angular distribution	66
7	XUV detachment from O^-	79
7.1	The oxygen anion	80
7.2	The experiment	82
7.3	Results	84
7.4	Discussion	89
7.5	Conclusion	91
8	Lifetimes of an excited state of H_2O^+	93
8.1	The water cation	93
8.2	The experiment	96
8.3	Results	98
8.4	Discussion	108
8.5	Conclusion	109
9	XUV fragmentation of the Zundel cation $H_5O_2^+$	111
9.1	The Zundel ion	112
9.2	The experiment	113
9.3	Results	115

CONTENTS

9.4 Discussion 131

9.5 Conclusion 135

10 Summary **139**

List of publications **141**

 Included in this dissertation 141

 Other articles 141

Bibliography **143**

Introduction

During the last century the field of atomic and molecular physics has provided an ever increasing insight to the structure and dynamics of atoms, ions and molecules. As atoms, ions and molecules are found both on Earth and in space the application of the obtained knowledge ranges just as wide. Understanding the emission spectra from comets and composition of the atmosphere are but two examples. Besides accumulating empirical information this have been of paramount importance to improve and judge the validity of theoretical models and their predictions.

Atoms, ions and molecules have been very thoroughly investigated in the infrared (IR), visible and ultra violet (UV) range as a testimony to the great advances within laser physics. Explorations in the extreme ultra violet (XUV) and x-ray region however have been difficult to facilitate.

Conventional lasers are unable to reach the XUV range ($\lambda_\gamma = 10\text{-}120\text{nm}$) with a noticeable intensity. Synchrotron radiation sources do provide photons in both the XUV and x-ray range and with repetition rates just below the GHz regime in multi bunch mode the number of photons per second is very high.

In experiments with dilute gas targets like ion beams the reaction probability depends on the photon count in the individual photon bunches and for such applications the intensity of synchrotrons yield only low reaction rates. As a consequence long measuring times are needed to obtain sufficient statistics. Collinear beam geometries have been adopted to increase

the reaction rates by having several meters of overlap between the photon and the ion beam.

Two complications arise from the high repetition rate and the collinear beam geometry. In time resolved measurements the repetition rates are actually too high. Even single bunch mode with the order of 100ns between photon pulses poses a technical challenge to link detected particles to a certain photon pulse. In a collinear beam geometry neutral particles can not be detected as their path coincide with the photon path.

With the commission of the first free electron laser (FEL) FLASH at DESY (Hamburg, Germany) in 2005 an entirely new era of photon science was introduced. The photon count in a single bunch reached an even higher level than which was necessary to conduct experiments on dilute ion beam target in a crossed beam geometry. Later upgrades have increased the intensity at FLASH to the order of 10^{13} photons/pulse in the wavelength range $\lambda = 6.9-47\text{nm}$. By utilizing a FEL both the complications from high repetition rates and collinear beam geometries can be circumvented.

Since the commissioning of FLASH two other FELs have started operation; the LCLS at the SLAC National Accelerator Laboratory (Menlo Park, California) and SACLA at the RIKEN Harima Institute (Hyōgo, Japan). At present two new FEL sources are under construction: the SwissFEL at the Paul Scherrer Institute (Würenlingen, Switzerland) and the European x-ray free electron laser (XFEL) (Hamburg, Germany).

At the trapped ion fragmentation with a FEL (TIFF) ion beam setup a crossed beam geometry is implemented and by utilizing two electron spectrometers and several fast, position and time sensitive detectors, electrons as well as positive, neutral and negative fragments can be detected simultaneously. The TIFF ion beam setup is located at the PG2 beam line of FLASH.

In this dissertation I will present the results from three measurements conducted at TIFF. Two of the experiments utilizes the FEL while the last merely exploits the ion beam setup.

In the extreme ultra violet (XUV) study of the photodetachment from the negative oxygen anion the branching ratios between the single and double photodetachment are investigated and the feasibility to perform photoelectron spectroscopy under FEL conditions is proven to be possible though with a greatly reduced photon flux.

A fragmentation study of the water cation has been performed with a Nd:YAG laser and photon energies below the threshold for dissociation of the ground state of the water cation. Both the branching between the $\text{OH}^0 + \text{H}^+$ and the $\text{OH}^+ + \text{H}^0$ channel and the life time of the second excited state ($\tilde{\text{B}}^2\text{B}_2$) were obtained.

Finally the branching ratios of several open fragmentation channels from the protonated water dimer after XUV exposure have been found and the energy of the major channel has been estimated.

The remaining part of this dissertation is divided into 9 chapters (chapter 2-10) and outlined as follows.

Chapter two sketches the theoretical foundation for working with molecules, photoabsorption and fast ions. This provides the necessary basis for the context of the experiments presented.

Chapter three outlines the experimental setup from ion creation, through beam guidance and mass selection to photon-ion interaction and subsequent particle detection. A presentation of the employed photon sources concludes the chapter.

Chapter 4 describes the data acquisition (DAQ) process at TIFF from a particle impact on a detector to the information is pre-processed and ready for a kinematic analysis. Furthermore a four mode DAQ scheme to obtain a background subtracted photon induced signal is described.

Chapter 5 presents the software based coincidence analysis implemented at TIFF to isolate simultaneously detected particles, suppress random contributions and retrieve further information from a photoinduced process.

Chapter 6 introduces the numerical software package SIMION utilized to estimate voltages to be applied during experiments and to interpret the obtained data. Through user programs the trajectories of particles from physical reactions like electron detachment and fragmentation can be simulated.

Chapter 7, 8 and 9 present the three primary experiments conducted during my PhD study. The structure of these chapters will be identical. The first section will give a description of the particle investigated while the second section summarizes the actual experimental setting for that study. The results and discussion is presented in separate sections to clearly mark the difference between results and possible implications.

Chapter 10 summarizes the results of this dissertation.

Theoretical foundation

The Born-Oppenheimer approximation is a corner stone in molecular physics. Even when not applicable it is often the starting point for more elaborate models. The following introduction to molecular physics will therefore give a brief brush up of the Born-Oppenheimer approximation in order to ensure concepts like orbitals and potential energy surfaces are introduced in a proper contexts. The potential energy surface picture will be used to introduce photoabsorption, -ionization and -fragmentation.

Key concepts for working with fast moving ions and the definition of some generalized coordinates to calculate momentum changes and kinetic energy releases in fragmentation processes in a fast moving ion beam will conclude the theoretical basis needed in this dissertation.

2.1 Introduction to molecular physics

A molecule is a group of atoms bound together by the Coulomb attraction between the nuclei and electrons. Molecular physics is the study of the properties, structures and dynamics of molecules. In a quantum mechanical approach this is achieved by finding the set of eigenfunctions (Ψ_q) that satisfy the time-independent Schrödinger equation:

$$H\Psi_q = E_q\Psi_q, \quad (2.1)$$

where H is the molecular hamiltonian and E represents the energies of the eigenfunctions. The hamiltonian can be approximated by the sum of three operators

$$\begin{aligned} H &= T_e + T_N + V_c \\ &= -\frac{\hbar^2}{2m_e} \sum_i \frac{\partial^2}{\partial r_i^2} - \sum_I \frac{\hbar^2}{2M_I} \frac{\partial^2}{\partial R_I^2} + V_c(r, R) \end{aligned} \quad (2.2)$$

where r and R are the coordinates for the electrons and nuclei, respectively, T_e is the kinetic energy operator of the electrons, T_N is the kinetic energy operator of the nuclei and V_c is the Coulomb interaction between all the electrons, between the electrons and the nuclei and between all the nuclei. So far only Coulomb interactions are included. Knowing the molecular eigenfunctions, Ψ_q , and energies, E_q , will reveal information about the properties, structures and dynamics of the molecule. However, even for molecules with a few nuclei and electrons calculating the eigenfunctions become a tremendous task, and some simplifications are needed.

2.1.1 The Born-Oppenheimer approximation

The forces acting on the electrons and nuclei are in most cases of the same magnitude, but as the nuclei are far heavier, the acceleration of the nuclei are negligible compared to that of the electrons. As a result of this, a part of the molecular hamiltonian can be rephrased as an electronic hamiltonian

$$H_{e,R}(r) = T_e(r) + V_{c,R}(r) \quad (2.3)$$

where the electrons only parametrically depend on the nuclear positions (R) through the Coulomb potential. From the electronic hamiltonian a complete, orthonormal set of eigenfunctions $\chi_{i,R}(r)$ and energies $E_i(R)$ can be calculated for each fixed set of nuclear positions (R). A molecular eigenfunction can then be expanded as a linear combination of the complete set of electronic eigenfunctions

$$\Psi_q = \sum_i \Phi_i(R) \chi_{i,R}(r) \quad (2.4)$$

where the expansion coefficients $\Phi_i(R)$ are eigenfunctions representing the nuclear motion when the electronic system is in state i . This can be realized by inserting the molecular wavefunction into the time-independent Schrödinger equation and projecting onto the complete set of functions $\chi_{s,R}(r)$. This gives the set of coupled equations

$$\sum_i \langle \chi_{s,R}(r) | T_e + T_N + V_c | \chi_{i,R}(r) \rangle \Phi_i(R) = \sum_i \langle \chi_{s,R}(r) | E_q | \chi_{i,R}(r) \rangle \Phi_i(R), \quad (2.5)$$

Utilizing the orthonormality of the electron eigenfunctions ($\langle \chi_s | \chi_i \rangle = \delta_{si}$) and $[T_e(r) + V_{c,R}(r)] \cdot \chi_{i,R}(r) = E_i(R) \chi_{i,R}(r)$.

$$\sum_i \langle \chi_{s,R} | T_N | \chi_{i,R}(r) \rangle \Phi_i(R) + (E_s(R) - E_q) \Phi_s(R) = 0, \quad (2.6)$$

The set of equations can be uncoupled by taking advantage of the slow velocity of the nuclei compared to the velocities of the electrons. This is equivalent to the electronic eigenfunctions varies only slowly with respect to the nuclear coordinates (R) and therefore the partial derivatives $\frac{\partial}{\partial R} \chi_{i,R}(r)$ can be neglected compared to $\frac{\partial}{\partial R} \Phi(R)$. The kinetic energy operator (T_N) can then be taken outside the integration and as the electronic eigenfunctions are chosen to be orthonormal ($\langle \chi_s | \chi_i \rangle = \delta_{si}$) only the diagonal terms ($i = s$) remains. This is known as the Born-Oppenheimer approximation [1] (or see [2, p. 480-5] for a more recent introduction).

The coupled set of equations hence reduces to a Schrödinger equation for the nuclear motion, where the electronic energies will constitute an effective potential.

$$H_N \Phi_s(R) = E_q \Phi_s(R), \quad (2.7)$$

where $H_N = T_N + E_s(R)$.

Another consequence of the Born-Oppenheimer approximation is that the full molecular wavefunction can be reduced to a single term.

$$\Psi_q = \Phi_s(R) \chi_{s,R}(r) \quad (2.8)$$

The electronic energies are functions of the nuclear coordinates, $E_s(R)$, and are called potential energy surfaces (PES). A PES minimum signifies a bound geometry, and a PES sloping down toward ever increased nuclear

distance signifies a dissociative path. A PES reveals the binding energy as well as the optimal geometry; angles and internuclear distances (also known as the bond length). PES are often illustrated by keeping all but one variable fixed.

Figure 2.1 shows the potential energy for the three lowest states in the water cation (H_2O^+) as a function of the O-H bond length and the HOH angle. The lowest state ($\tilde{X} \ ^2\text{B}_1$) is the stable ground state. The second ($\tilde{A} \ ^2\text{A}_1$) and third ($\tilde{B} \ ^2\text{B}_2$) lowest states are also binding, though at different OH separation and HOH angles.

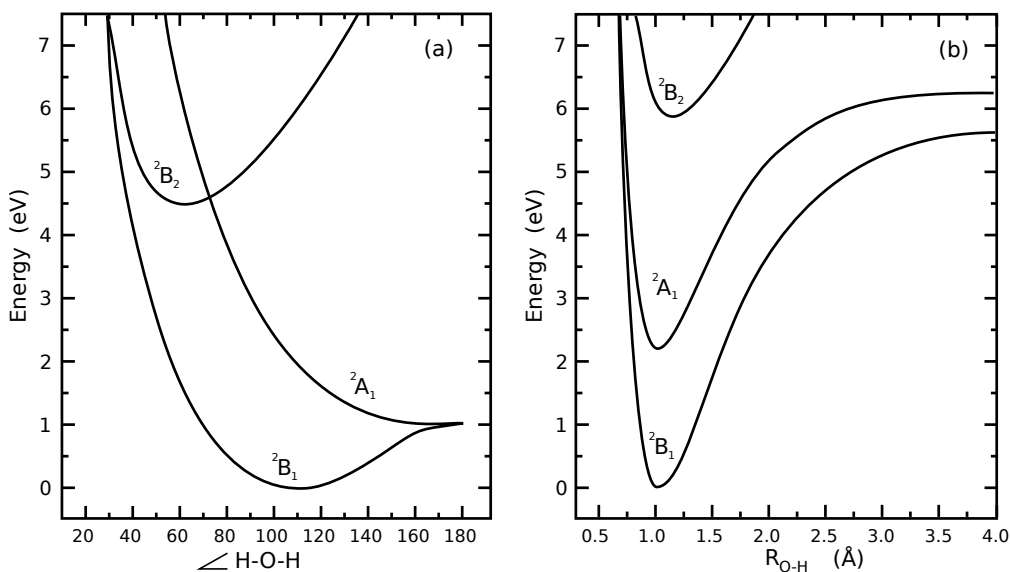


Figure 2.1: The potential energy for the lowest state in the water cation as a function of: (a) the HOH angle while keeping the bond length $R_{\text{O-H}} = 1.03 \text{ \AA}$ fixed. (b) the bond length $R_{\text{O-H}(2)}$ while keeping $R_{\text{O-H}(1)} = 1.03 \text{ \AA}$ and the HOH angle = 102.5° fixed at the calculated equilibrium values. Reproduced after Sage et al. [3].

2.1.2 Corrections to the BO approximation

Suppressing the nuclear motion with the BO approximation cannot be valid when finding the exact wavefunctions. Furthermore, only Coulomb

interactions have been considered so far. However, if the deviation between the exact hamiltonian and the BO-approximated hamiltonian is small, perturbation theory can be utilized with the BO-approximated hamiltonian as a zeroth order hamiltonian ($H^0 = H^{BO}$) and a suitable perturbation (H') can be applied to better describe the exact hamiltonian.

$$H^{exact} = H^{BO} + H' \quad (2.9)$$

The contribution from the perturbation must be much smaller than the zero order hamiltonian. It can therefore be more convenient to extend the BO hamiltonian to include some of the ignored couplings between electronic and nuclear wavefunctions, and then choose a basis set, in which the full hamiltonian splits in a diagonalizable part H^0 and a small state mixing perturbation H' with non-zero off-diagonal element. In the different basis sets different operators commute and constitute good quantum numbers. The basis set and set of good quantum numbers must, hence, be chosen to minimize the size and nature of the needed perturbations between the exact and zero order hamiltonian.

Two different approaches are used to add the coupling elements to the BO hamiltonian, the diabatic and adiabatic.

In the diabatic picture non-zero off-diagonal elements of the electron hamiltonian is included $\langle \chi_i | H_e | \chi_j \rangle \neq 0$ while still ignoring part of the electron-electron repulsion (the single configuration approximation). Hereby PES of difference symmetry are allowed to mix and have states with the same energy for the same nuclear coordinates. It is only in single points two PES meet and these points are called conical intersections.

In the adiabatic picture the electronic wavefunctions dependence on the nuclear coordinates is included, $\langle \chi_i | T_N | \chi_i \rangle \neq 0$. This gives a small correction of the PES, resulting in adiabatic PES and can describe the effect of rotation and vibration of the nuclei coupling to the electron motion, shortened to rovibronic couplings.

The picture to use depends on the system to analyze and phenomena to describe. Furthermore, the hamiltonian can be extended to include the relativistic spin-orbit perturbation and so fort. A more elaborate presentation of the terms neglected in the BO approximation can be found in [4].

2.1.3 Molecular orbitals

With the introduced BO approximation it is possible to calculate the electronic part ($\chi_{s,R}$) of the molecular wavefunctions (Ψ_q). This is, however, still complicated and finding exact wavefunctions for molecules more complicated than a few atoms is a tremendous task. The electron-electron repulsion entangles the wavefunctions. To overcome the entanglement, the central field approximation allows the calculation of the wavefunction of each electron in turn, treating the rest as a charged cloud mainly distributed around each nucleus. The single electron wavefunctions ($\phi_m(r_i)$) are called orbitals and the full electronic wavefunction for N_e electrons is given as the product of the all the orbitals.

$$\chi_{s,R} = \phi_a(r_1)\phi_b(r_2) \dots \phi_z(r_{N_e}) \quad (2.10)$$

where $m = a, b, \dots, z$ labels the individual orbital and r_i are the coordinates of electron i . The total electronic energy will be the sum of the individual electron energies.

The self-consistent field method (SCF) calculates the orbital of each electron in turn and uses initial trial-function to describe to the central field from all the other electrons. The resulting orbitals are iteratively improved by recalculations until the output charge distribution converges to the input distribution of electrons. It is then apparent that good initial guesses will greatly reduce the number of iterations needed. The analytically calculated orbitals from atomic hydrogen centered on each nucleus in the molecule will constitute fairly good trial-functions.

The full electronic wavefunction must obey the Pauli exclusion principle and take the electron spin into account by being antisymmetric, that is change sign under interchange of any two electrons. The spin can be introduced by multiplying with spin wavefunctions (q_x). To cover the different spin combinations full electronic wavefunction can be written as a Slater determinant [2, p. 356].

$$\chi_{s,R} = \frac{1}{\sqrt{N!}} \begin{vmatrix} q_a\phi_a(r_1) & q_b\phi_b(r_1) & \dots & q_z\phi_z(r_1) \\ q_a\phi_a(r_2) & q_b\phi_b(r_2) & \dots & q_z\phi_z(r_2) \\ \vdots & & & \\ q_a\phi_a(r_{N_e}) & q_b\phi_b(r_{N_e}) & \dots & q_z\phi_z(r_{N_e}) \end{vmatrix} \quad (2.11)$$

The Hartree-Fock method combines the self-consistent field method with a variational approach to iterative calculate and find the lowest possible energy electronic energy and the related electron orbitals [5, p. 295-9].

For molecules the trail-functions can be improves by using linear combinations of atomic hydrogen orbitals (LCAO) centered on each nuclei.

$$\phi = \sum_i c_i \phi_i^{AO} \quad \text{LCAO (2.12)}$$

Where c_i is expansion coefficients and ϕ^{AO} is the hydrogenic orbitals. These linear combinations are called molecular orbitals.

The linear combination for each molecular orbital must, in principle, be infinite to minimize the deviation from the exact solution, though smaller sets can give acceptable results. The smallest basis to describe a water molecule (H_2O) will be; H_{1s_A} , H_{1s_B} , O_{2s} , O_{2p_x} , O_{2p_y} and O_{2p_z} . Where A and B labels the two hydrogen atoms. The oxygen orbitals are shown in Figure 2.2. The 1s orbital on oxygen does not participate in the bonding and hence does not contribute to the molecular orbitals.

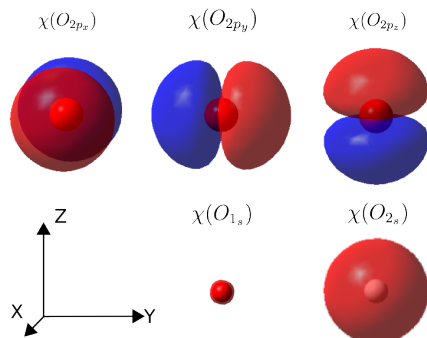


Figure 2.2: Oxygen orbitals for first and second shell.

the molecule. The SALCs are then used in the linear combination with orbitals from the remaining atoms. SALCs of different symmetry are orthogonal and hence diagonalizes the electronic Schrödinger equation in a

If the molecule expresses some symmetry, the molecular orbitals must reflect this and only atomic orbitals that, due to their place and orientation share this symmetry, will have a non-zero contribution to a particular molecular wavefunction. Hence, symmetry can reduce the size of the basis set needed to span the molecular orbitals.

Extending the LCAO approach, the orbitals from each atom of the same type can be used to form symmetry adapted linear combinations (SALC), reflecting their positions in

block diagonal form with one block per symmetry in the molecule.

For water two SALC wavefunctions can be made for the hydrogens 1s orbitals, see Figure 2.3

$$\begin{aligned}\chi(A_1) &= \chi(H_{1s_A}) + \chi(H_{1s_B}) \\ \chi(B_2) &= \chi(H_{1s_A}) - \chi(H_{1s_B})\end{aligned}\tag{2.13}$$

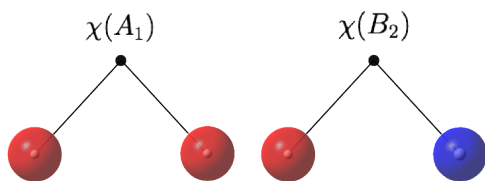


Figure 2.3: SALC wavefunctions made from the hydrogens in water.

These can be combined with oxygen orbitals, to make only three SALCs to describe the orbitals in water

$$\begin{aligned}\chi(a_1) &= c_1\chi(O_{2s}) + c_2\chi(O_{2p_z}) + c_3\chi(A_1) \\ \chi(b_1) &= \chi(O_{2p_x}) \\ \chi(b_2) &= c_4\chi(O_{2p_y}) + c_5\chi(A_1)\end{aligned}\tag{2.14}$$

Thereby the basis set have been reduced from 6 independent atomic orbitals to 3 orthogonal molecular orbitals and the electron configuration for the ground state of neutral water will be $(1a_1)^2(2a_1)^2(1b_2)^2(3a_1)^2(1b_1)^2$.

The name of the SALC orbitals refers to their symmetry point group. The symmetry is described by the set of operations that can be performed on the orbital while leaving it unchanged. There are five types of symmetry operations:

- The identity operation, E . Does nothing and hence belongs to all molecules.
- The inversion operator, i . Inverts the molecule through a center of symmetry.

- Mirror operations, σ . Mirrors the molecule in a plane.
- An n -fold rotation operation around an axis C_n . These are specified as the number (n) of times the molecule can be rotated around this axis before it is back to the starting point. If the molecule can be turned at an arbitrary angle, and still be unchanged, this is written as C_∞
- A rotation-reflection operator, S_n . A rotation followed by a reflection.

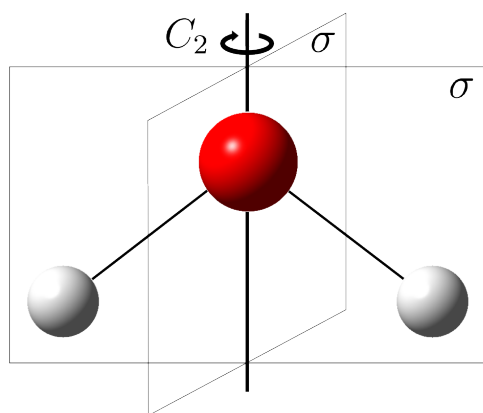


Figure 2.4: A water molecule possesses the following symmetry operators; The identity, a two fold rotation (C_2) and two mirror planes (σ).

The set of symmetry operations can furthermore be used to describe the symmetry of the molecule itself. E.g. water in its ground state possesses the identity, a two-fold rotation and two mirror operators placing it in the C_{2v} point group (see Figure 2.4) according to the Schönflies notation. A more extensive introduction to point groups and a scheme for assignment can be found in [5, p. 126-130].

2.2 Photoabsorption

A particle (atom, ion or molecule) interacting with electromagnetic radiation can in the weak-field limit be treated as a perturbation to the time independent wavefunction of the particle. Single photon absorption is a

first order perturbation where a photon with energy $\hbar\omega$ couples the initial state $|i\rangle$ to the final state $|f\rangle$. The electromagnetic field will be assumed to be linearly polarized in the \hat{e} -direction. The probability for a process to take place can be expressed as a reaction cross section. The cross section can classically be explained as the likelihood for the photon with a given extent to collide with one of the particles constituting a total area to hit, and the cross section can be found to be [2, p 191]

$$\sigma_{fi} \propto \langle f | \hat{e} \cdot \hat{D}_{fi} | i \rangle^2 \quad (2.15)$$

where \hat{D}_{fi} is the electric dipole moment operator. The factor $\langle f | i \rangle$ is known as the Franck-Condon factor, measuring the overlap between the initial and final state. The absorption of a photon is a fast process compared to the motion of the nuclei of a molecule. Hence, in the PES picture a photon absorption will be a vertical transition to a state with higher energy, as sketched with the vertical black arrow on Figure 2.5. Both states must have a high probability density for the same nuclear coordinates. The final state is most likely not in an equilibrium position and will hence start to evolve after the absorption. For molecules this can induce rotations and vibrations. For higher energies the final state might be dissociative, leading to a fragmentation of the molecule (green curve in Figure 2.5). The final state can be quasi stable with some tunneling to a dissociative part of the PES (blue curve) or a stable state (red curve). From an excited state the molecule can either emit excessive energy through radiation or couple to a dissociative state. The latter process is called predissociation. Relaxation can even occur through non-dissociative, non-radiative process where system slides down coupled PES from different states.

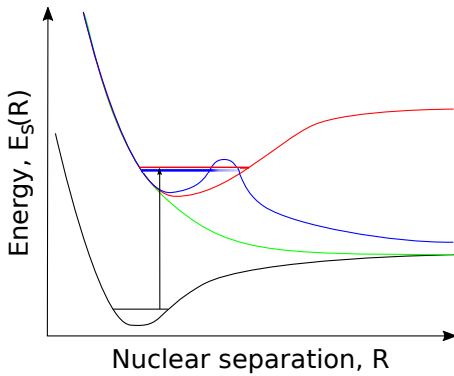


Figure 2.5: A schematic photo absorption process from an initial stable state (black curve) to a final state which is either dissociative (green curve), stable (red curve) or quasi stable with possible tunneling to a dissociative part of the PES (blue curve).

If more than one final state or several pathways from $|i\rangle$ to $|f\rangle$ exist, each process can have a different cross section, and the sum of these will constitute the total cross section for a process to occur

$$\sigma_{total} = \sum_i \sigma_i \quad (2.16)$$

The probability for one particle to absorb a photon in the time interval $[t; t+dt]$ is $P(dt) = \phi_\gamma \sigma dt$, where $\phi_\gamma = N_\gamma / (A_\gamma dt)$ is the photon flux, N_γ is the number of photons and A_γ is the cross section area of the photon beam. Hence, the probability to absorb a photon in the time interval Δt is

$$P(\Delta t) = 1 - e^{-\phi_\gamma \sigma \Delta t} \sim \phi_\gamma \sigma \Delta t \quad (2.17)$$

where the last step is a Taylor expansion when the field is weak ($\phi_\gamma \sigma \Delta t \ll 0$).

Hence, assuming a low photon flux, the number of reactions (R) to occur is given by the initial number of particles (N_I) in the photon path.

$$R = \phi_\gamma N_I \sigma \Delta t \quad (2.18)$$

If the photon flux is high, the particle sample might deplete, introducing a deviation from the linear dependency.

For experimental purposes the photon flux as well as the number of ions are not directly observable. Measurable quantities are the photon

wavelength (λ), photon pulse energy (E_γ), profile of the beams and the ion current (I_I), charge (q_I) and energy (E_I). With this in mind the number of photons is given by $N_\gamma = \frac{E_\gamma}{E_\lambda}$ and the number of ions can be expressed as a linear density $l_I = \frac{I_I}{q_I \cdot v_I}$ where the velocity is given by the ion energy and mass $v_I = \sqrt{2E_I/m_I}$. While the geometrical overlap of the two beams can be expressed by a vertical overlap factor [6]

$$F = \int g_\gamma(y)g_{\text{ions}}(y)dy \quad (2.19)$$

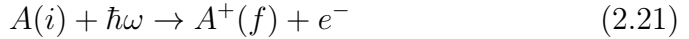
, where g_X is the vertical profile of the photon ($X = \gamma$) and ion beam.

The number of reactions can then be expressed as

$$R = N_\gamma \cdot l_I \cdot F \cdot \sigma \quad (2.20)$$

2.3 Photoionization

When a particle absorbs a photon with more energy ($E_\gamma = \hbar\omega$) than the binding energy of an electron, an electron can be detached, leaving the particle ionized. A photoionization reaction for a particle A can be written as



where i and f refer to the internal state of the particle.

The electron will then leave the system with the kinetic energy released

$$E_{\text{KER}}(e^-) = E_i + E_\gamma - E_f \quad (2.22)$$

where E_f and E_i are the initial and final energy of the particle, respectively. After losing an electron the particle are not necessarily in an equilibrium state and can relax as mentioned above.

The probability for an electron to be emitted in a specific direction can be found from the differential cross section for ionizing an unpolarized molecular target by a linear polarized photon beam with polarization direction $\hat{\epsilon}$ [2, p. 745-747]

$$\frac{d\sigma_{fi}}{d\Omega} = \frac{\sigma_{fi}}{4\pi} (1 + \beta P_2(\cos(\theta))) \quad (2.23)$$

Where $P_2(x) = \frac{1}{2}(3x^2 - 1)$ is the second order Legendre polynomial and θ is the angle between the photon beam polarization $\hat{\epsilon}$ and the direction of the emitted electron ν . σ_{fi} is the total cross section for ionization and β is the asymmetry parameter. For the differential cross section to be non-negative at all angles β must be between -1 and 2. A value of $\beta = -1$ corresponds to the electrons being ejected perpendicular to the photon beam polarization, $\hat{\epsilon} \perp \nu$. $\beta = 2$ gives an ejection parallel to the polarization, $\hat{\epsilon} \parallel \nu$, while for $\beta = 0$ the emission angle is independent of $\hat{\epsilon}$ and any angle is equally likely.

The intensity ($I(\Omega)d\Omega$) of emitted electrons in the solid angle $d\Omega$ is given directly from the differential cross section by

$$I(\Omega)d\Omega = \frac{d\sigma_{fi}}{d\Omega}d\Omega \quad (2.24)$$

Writing the solid angle as $d\Omega = \sin(\theta)d\theta d\phi$, inserting the Legendre polynomial and integrating with respect to ϕ over the interval $\phi = [0; 2\pi]$ returns an expression more directly applicable

$$I(\theta)d\theta = \frac{\sigma_{fi}}{2} \left(1 + \frac{\beta}{2} (3 \cos^2(\theta) - 1) \right) \sin(\theta)d\theta \quad (2.25)$$

From an angular distribution of photoelectrons ($I(\theta)$) it is hence possible to find β and possibly to predict the orbital geometry before ionization.

So far only single photon absorption has been considered. Where more photons are absorbed the photons can either be absorbed simultaneous or sequential and if more than two are absorbed even combinations can occur. However, in general the probability for an ionization involving N photons is on the form [7, p. 94]

$$P(\Delta t) = 1 - e^{\phi_\gamma^N \sigma^{(N)} \Delta t} \sim \phi_\gamma^N \sigma^{(N)} \Delta t. \quad (2.26)$$

Where the Taylor expansion assumes a low photon flux. For sequential absorption the cross section can be expanded to include a series of $(N-1)$ unobservable, intermediate states. For two photon absorption this will be

$$\sigma^{(2)} \propto \left| \sum_j \frac{\langle f | \hat{\epsilon} \cdot \hat{\mu} | j \rangle \langle j | \hat{\epsilon} \cdot \hat{\mu} | i \rangle}{[E_{ji} - \hbar\omega]} \right|^2 \quad (2.27)$$

where j is the intermediate states and E_{ij} is the energy difference between state i and j . For further details on multiphoton absorption and ionization see P. Lambropoulos [7].

2.4 Fragmentation of small molecules

A molecule AB breaking in two fragments A and B can be written as



For stable molecules there must be a source of excess energy e.g. photo absorption to overcome the binding. For such a twobody break up momentum conservation demands that the fragments move in opposite directions, splitting the kinetic energy released (KER)

$$\begin{aligned} 0 &= m_A \cdot v_A + m_B \cdot v_B \\ \Delta E_{\text{KER}} &= E_A + E_B \end{aligned} \quad (2.29)$$

Following this the energy of the fragments will be

$$\begin{aligned} E_A &= \frac{m_B}{m_A + m_B} \Delta E_{\text{KER}} \\ E_B &= \frac{m_A}{m_A + m_B} \Delta E_{\text{KER}} \end{aligned} \quad (2.30)$$

The angular distribution of photofragments from diatomic molecules have been investigated by R. N. Zare [8]. If the photon beam is linear polarized with a polarization vector $\hat{\epsilon}$, then Zare finds, that the intensity of fragments ($I(\theta)d\theta$) at the angle $d\theta$ relative to the photon polarization $\hat{\epsilon}$ will have the form of a dipole radiation pattern

$$I(\theta)d\theta = \frac{1}{2} \left(1 + \frac{\beta}{2} (3 \cos^2(\theta) - 1) \right) \sin(\theta)d\theta, \quad (2.31)$$

Similar to the photoelectron angular distribution (2.25). β is the asymmetry parameter must be between -1 and 2. A value of $\beta = -1$ corresponds to the fragments being ejected perpendicular to the photon beam polarization,

$\hat{\epsilon} \perp \nu$. $\beta = 2$ gives an ejection parallel to the polarization, $\hat{\epsilon} \parallel \nu$, while for $\beta = 0$ the angular distribution will be isotropic.

If the molecule can break up into more than two fragments the different combinations of fragments are called channels and each channel can have a different energy release and cross section for occurring. E. g. for three fragments



2.5 The fast ion beam technique

So far all molecules have been treated as stationary. However, molecules in the gas phase are hard to fixate to one point in space and after a reaction one would need detectors in all possible directions to observe all electrons and fragments. Furthermore, electrons and fragments from the parent molecules must be differentiable from other molecules in the target area. At the expense of only being capable of investigating charged molecules, these difficulties can be overcome by utilizing a fast ion beam setup, where the kinetic energy of the molecules to be investigated are far higher than other molecules residing in the target area. Thereby, all fragments from the charged parent molecule are projected in one direction and can be caught within a smaller space angle. Fragments from random molecules might drift into the detection system however at a different time scale and these fragments will be delocalized in time.

For a fast moving, though not relativistic, molecule moving parallel to the Z-axis in the laboratory reference frame (LAB) with velocity $v_{z,LAB}$, the Galilean transformation to the molecular center of mass (CM) reference frame will be

$$\begin{aligned}
 x_{CM} &= x_{LAB} \\
 y_{CM} &= y_{LAB} \\
 z_{CM} &= z_{LAB} - v_{LAB,z} \cdot t_{LAB} \\
 t_{CM} &= t_{LAB}
 \end{aligned}
 \tag{2.33}$$

If not otherwise specified the laboratory reference frame will be assumed and of course a change in velocity, e.g. due to the kinetic released energy in a fragmentation process, will be independent of the reference frame.

The impact position (x, y, z) of a fragment on a detector and time of flight (TOF) from the point of reaction (x_0, y_0, z_0) to a detector surface can be defined in generalized dimensionless coordinates [6] for the position ρ and time τ independent of the geometry of the detection system

$$\begin{aligned}\rho_F &= \frac{\sqrt{(x - x_0)^2 + (y - y_0)^2}}{z - z_0} \\ \tau_F &= \frac{TOF}{(z - z_0)/v_I}\end{aligned}\tag{2.34}$$

where $r = \sqrt{(x - x_0)^2 + (y - y_0)^2}$ is the transverse distance from the interaction point, $\tilde{z} = z - z_0$ is the distance transversed by a straight incident ion orbit through the interaction point to the detector surface, and v_I is the speed of the molecule before fragmentation. The normalized coordinates thus indicate the displacement of the fragments relative to a non-deflected and non-retarded fragment emerging with the initial velocity of the parent molecule. The velocity of the parent molecule can be obtained from the kinetic energy, $v_I = \sqrt{2 \cdot E_{KER}/m_I}$.

The longitudinal (Δp_F^{\parallel}) and transverse (Δp_F^{\perp}) momentum changes relative to the initial momenta (p_F) can be obtained directly from the normalized coordinates [9] as

$$\begin{aligned}\frac{\Delta p_F^{\parallel}}{p_F} &= \frac{\Delta p_F}{p_F} \cos(\theta) = - \left(1 - \frac{1}{\tau_F}\right) \\ \frac{\Delta p_F^{\perp}}{p_F} &= \frac{\Delta p_F}{p_F} \sin(\theta) = \frac{\rho_F}{\tau_F}\end{aligned}\tag{2.35}$$

The kinetic energy released to a fragment can be obtained [10] as

$$E_F = \frac{m_F}{m_I} \left(\left(\frac{\rho_F}{\tau_F} \right)^2 + \left(1 - \frac{1}{\tau_F} \right)^2 \right) E_I\tag{2.36}$$

Where m_F is the fragment mass and m_I is the mass of the ion. The total kinetic energy released (KER) in a breakup process will be the sum over the fragments.

$$E_{\text{KER}} = \sum_F E_F \quad (2.37)$$

The angle of emission relative to the photon polarization for a polarization in the y_{LAB} direction is [10]

$$\theta = \arccos \left(\frac{(y - y_0)/(z - z_0)}{\sqrt{(\rho/\tau)^2 + (1 - 1/\tau)^2}} \right) \quad (2.38)$$

while for polarization in the z_{LAB} direction [6]

$$\theta = \arctan \left(\frac{\rho/\tau}{1/\tau - 1} \right) \quad (2.39)$$

Experimental setup

The experimental setup used for the present studies is the trapped ion fragmentation with a free electron laser (TIFF) [6], situated as an end station of the plane grating monochromator beamline PG2 [11], at the free electron laser in Hamburg (FLASH) [12, 13] at Deutsches Elektronen-Synchrotron (DESY). DESY is a German science facility, hosting several particle accelerators including a linear electron accelerator and free electron lasers (FEL) for production of intense photon beams from the extreme ultraviolet to hard x-rays.

At TIFFF positive and negative ions can be produced and accelerated to form a collimated, mass-selected and focused ion beam, which can be crossed with a laser. The setup includes two ion traps. One before and one at the crossing point of the photon and ion beam. The interaction and detection region contain two electron spectrometers and a total of 5 MCP detectors with delay line anodes. This enables simultaneously detection of electrons and positive, neutral and negative ions. The setup is illustrated in Figure 3.1 and will be presented as an ion experiences it from the ion source and towards the detectors. The available photon sources are FLASH and a pulsed, optical Nd:YAG laser.

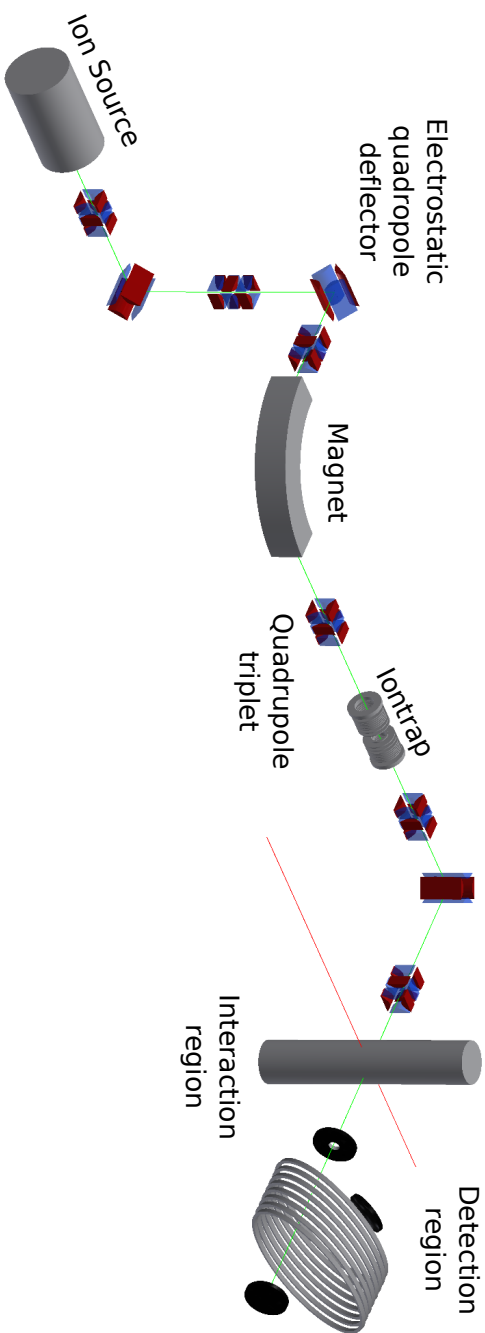


Figure 3.1: Schematic illustration of the ion beam setup TIFP at FLASH. The red line illustrates the FLASH beam path while the solid green line shows the ion beam path from the ion source (to the left) through several electrostatic steering elements and a mass separation magnet to the interaction region and the detectors. Plate deflectors, Einzel lenses and various faraday cups and apertures have been omitted for simplicity.

3.1 The ion source

The ion source is a hollow cathode source and can produce both positive and negative ions. A schematic is shown on Figure 3.2. The source comprises a hollow anode placed close to a hollow cathode. Both with inner diameters of 10mm and separated by 10mm. By applying a large electric potential difference ($U_{\text{Discharge}} = 1\text{-}2\text{kV}$) between the anode and cathode and filling the space between with a small amount of gas ($p_{\text{Source}} = 0.5\text{-}2$ Torr) a discharge will ignite a plasma. For small voltages and low gas pressure the resistance between the anode and cathode is almost infinite, and increasing the potential does not lead to a noticeable current increase. From the point where the first spark is struck the resistance drops to an almost vanishing value. To maintain a load on the power supply a resistor ($R = 22\text{k}\Omega$) is coupled in the circuit. From this point the discharge will be current limited and a small increase of voltage will increase the current and the intensity of the plasma. Typical values to maintain the discharge are a potential of $U_{\text{Discharge}} = [0.6\text{-}1.5]\text{kV}$ with a current of $I_{\text{Discharge}} = [30\text{-}60]\text{mA}$.

Gas is led in through the anode and to confine the gas to the region between the two electrodes a bias electrode with the same potential as the anode and with only a small central hole ($\phi \approx 0.4\text{mm}$) is placed on the other side of the cathode, creating an inclosure with only a small exit. After the bias electrode an extraction electrode is placed to extract ions from the plasma. The extraction potential is on the order of $U_{\text{Extraction}} = 0\text{-}4\text{kV}$.

The entire ion source is raised to a potential of $U_{\text{Platform}} = 1.5\text{-}5\text{kV}$. The ions generated in the plasma and leaving the source hence obtain a kinetic energy of ($U_{\text{Platform}} \approx 1.5\text{-}5\text{keV}$), corresponding to the applied potential.

$$E_{ion} = q \cdot U_{\text{Platform}} \quad (3.1)$$

Depending on the point of extraction in the plasma, a small offset can occur. This has previously been measured to $45 \pm 10\text{eV}$ with a source potential of 4.2kV [6] but the actual offset might vary with different discharge settings, gasses and pressures in the ion source.

With an inlet of water vapor the hollow cathode ion source produces in the order $1\mu\text{A}$ of ions and possibly electrons in negative ion mode.

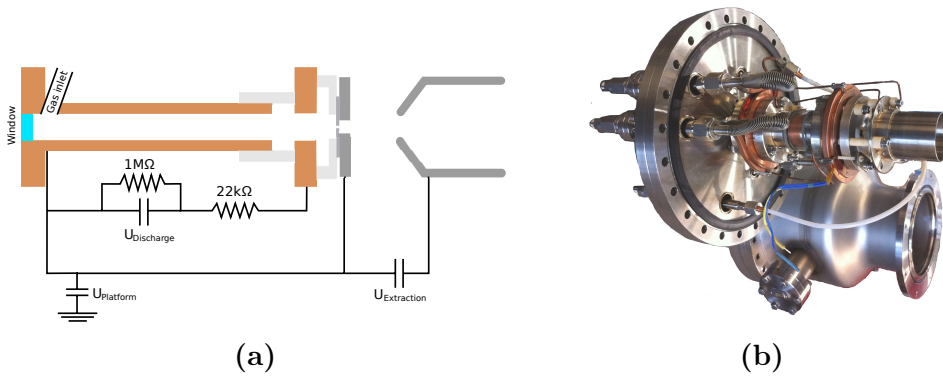


Figure 3.2: The TIFFF hollow cathode ion source. (a) Schematic view. The sign of the platform and extraction voltage depend on the operation mode, positive or negative ions. (b) A picture of the actual ion source mounted on a CF200 flange. The vacuum chamber is placed just below

3.2 Ion beam guidance

A series of electrostatic devices are used to guide and collimate the ion beam.

To achieve 90° bending of the ion beam electric quadrupoles are utilized. An electric quadrupole comprises four electrodes with hyperbolic surfaces, one electrode placed at each corner of a square. The two opposing electrodes have the same charge polarity while the other two have the same charge but opposite polarity. Thereby, the electric potential is zero on the center line, bisecting the sides of square and dividing it into two rectangles. The ion beam is sent in through one side of the square between two electrodes and bend 90° to pass out through an other side of the square. The quadrupole arrangement gives the advantage of bending the ion beam while still allowing free visibility through a 1cm slit all the way down each section of the beam line. This is useful when installing and aligning elements on the beam line.

For small corrections and rough steering deflector plates are used, which consist of two metal plates of opposite charge, placed on each side of the ion beam.

The focus of the beam is partly controlled with Einzel lenses. Three ring shaped electrodes placed shortly after one another with a ground potential on the two outer rings and potential of the same polarity as the beam on the center ring.

Quadrupole triplets are used for asymmetrical, two dimensional focusing and steering of the beam. A quadrupole triplet consists of three quadrupoles placed shortly after one another with the beam passing on the centerline between the four electrodes.

The focus and path of the ion beam can be analyzed with several movable elements placed between the guiding electrodes. At several positions the ion beam can be confined to a path through a fixed hole (1-5mm in diameter) aligned to the center of the vacuum chamber.

$\sim 0.5\text{m}$ and $\sim 1\text{m}$, respectively, before the interaction region two systems of plates are installed. These can be used to confine the ion beam to a rectangular area, not necessarily centered in the vacuum chamber, to better optimize the geometric overlap between the photon and ion beam.

A total of 11 Faraday cups are used to measure and optimize the ion current at different positions along the beam line. In principle, a Faraday cup is an electric conductor, which is charged by the ions or electrons impacting on it and discharges through an ampere meter to ground. However, when an ion hits the conductor, electrons might be emitted, thereby giving an incorrect measurement of the beam current. This effect has been tested at TIFF by installing a specially designed Faraday cup. Here, the conductor is enclosed in a negative biased housing where bias potential can be adjusted. Using a positive ion beam the bias potential was slowly reduced from $U_{\text{Bias}} = 0\text{V}$ while monitoring the measured ion current. Below $U_{\text{Bias}} < -120\text{V}$ the measured ion current is no longer affected by the bias potential and has a lower value than without the bias, indicating that no electrons are escaping. To avoid steering the beam with the faraday cup, the bias housing is shielded behind a grounded housing. Of course both housings have a center hole to allow the ions to hit the conductor.

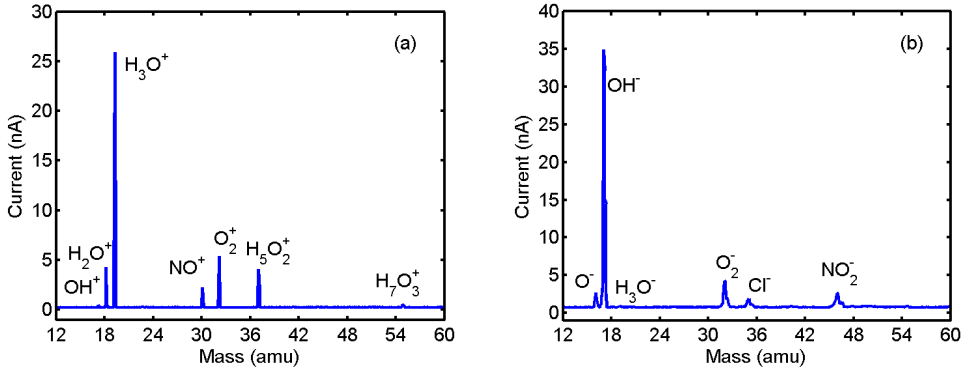


Figure 3.3: A mass scan of positive (a) and negative (b) ions using a faraday cup, located a few meters behind the separation magnet. The hollow cathode ion source with an inlet of water vapour was used for both scans.

3.3 Mass separation

The ions from the source are mass analyzed in a separating magnet. A relation for the mass (M) to charge (q) ratio can be obtained from the relation between speed (v) and acceleration (a) in a uniform circular motion of radius (R) $v^2 = aR$ combined with Newtons second law of motion ($F = Ma$), the Lorentz force ($F = q(E + B \times v)$) and (3.1)

$$\frac{M}{q} = \frac{R^2 B^2}{2U_{\text{Source}}} \quad (3.2)$$

where B is the size of the magnetic field applied perpendicular to the ion beam and assuming no electric fields (E) are present.

A mass scan for both positive and negative operation mode recorded in August and March of 2012, respectively, are shown in Figure 3.3. Both are recorded in a faraday cup approximately 3m after the magnet.

3.4 Ion trap

After the magnet the ions with the selected mass-charge ratio enter an electrostatic iontrap [14,15]. This trap is used to trap ions and chop the ion

beam in bunches to reduce the number of particle impacts on the detectors. An illustration of the ion trap and an overview of the signal logics is given in Figure 3.4. The electrode, S, is a grounded shield to minimize the electric fields outside the ion trap. The electrodes M1 to M8 constitute an electrostatic mirror. By switching the potential on electrode M1 to a lower value the mirror can be made transparent to the ions. In this way ions can be injected into the iontrap by opening the entrance mirror. The exit mirror is operated symmetrically. By switching the exit M1 electrode bunches of ions can be extracted from the ion trap. Extracting ion bunch of 2-4 μ s and only when they will overlap with photons in the interaction region can be greatly reduce the load on all detectors.

In order for the trap to respond on an sub μ s-time scale both the entrance and the exit of the trap are supplied by a high voltage switch attached to large capacity banks ($C = 4\text{-}5\mu\text{F}$). Caution is required when switching the polarity of this module! The switch operation is controlled by low voltage TTL-signals.

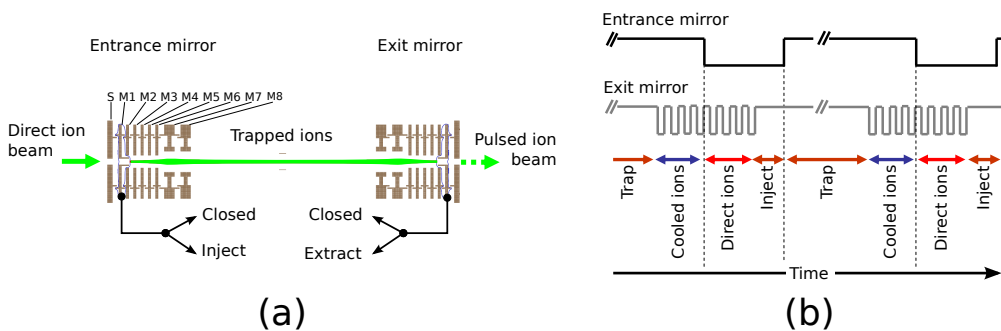


Figure 3.4: One of the two ion traps at TIFFF. (a) The electrode configuration. The shield S is kept at ground potential, electrodes M2-8 have a constant high value, while M1 can be switched between a low value, where ions can pass through the mirror, and a high value, where the ions are reflected. (b) Overview of the signal logics to operate the ion trap. Switching the exit M1 electrode every 2.5 μ s bunches of ions can be extracted. The bunched operation mode greatly reduces the load on the detection system. [14]

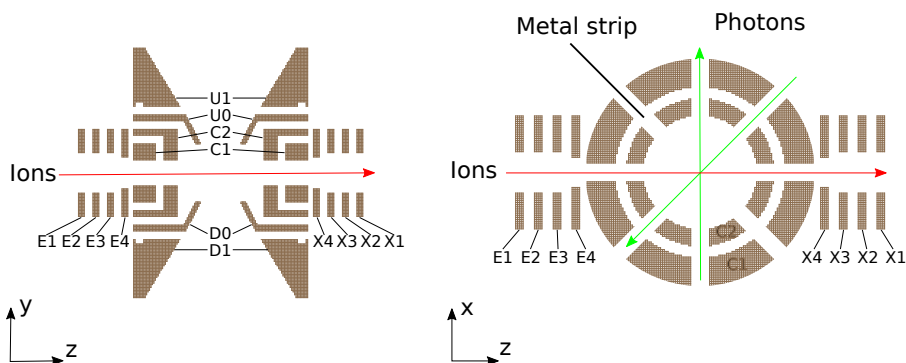


Figure 3.5: The electrode configuration of the TIFF interaction region in a sideview (YZ) and a top view (XZ). The electrodes $E1$ - $E4$ and $X1$ - $X4$ constitute a linear iontrap. $C1$, $C2$, $D0$ and $U0$ are used to form a saddle point potential or bias the entire region to a potential. $D1$ and $U1$ are the first electrodes in the electron spectrometer directly attached to the interaction region. The ions are injected from the left, while there are two possible entry point for photon beams. A metal strip can be inserted and be used to scan the vertical profile of all beams.

3.5 The interaction region

The interaction region consist of several electrodes arranged to either produce an electric field guiding the electrons, with minimal effect on the fragments and the parent molecules, or the manipulate the potential energy of the ions. The configuration of the electrodes are shown in Figure 3.5. The electrodes at the interaction region can be operated in four different modes.

1. Field free mode with all electrodes at ground potential.
2. Saddle point mode to extract electrons to eDET1 and eDET2.
3. Bias mode to differentiate charged fragments with different mass to charge ratio.
4. Ion trap mode.

In the field free mode, all fragments proceed completely undisturbed and for the fragments hitting DET1 or DET2 the impact position and TOF directly reflects the momentum of each fragments after an reaction. The kinetic energy and angular distribution of a fragments can be calculated as described in section 2.5.

In the saddle point mode, the electric field must serve to guide photodetached electrons to either the top or bottom of this region, in order for them to enter an electron spectrometer. At the same time the field must stop electrons from outside the interaction zone from entering. The ions will pass at the saddle point, where the potentials are lowest, and owing to their high forward momentum continue their path through the area mostly uninfluenced by the comparably weak field (below $\pm 200\text{V}$ at the electrodes and close to zero at the saddle point).

In the bias mode, an applied potential (U_{Bias}) will change the potential energy of charged molecules entering the region, and cause the beam to slow down before reaction, assuming both potential and molecules have same polarity, positive or negative. Hence, the fragments will be born with a lower kinetic energy. As the charged fragments leave the region they will be accelerated by the potential while the neutral fragments will remain at the lowered velocity. To simplify calculations it can be assumed that the extent of the bias potential is vanishing. With that assumption, the molecule will decelerate and charged fragments reach the new speed instantaneously after the reaction. The fragment kinetic energies (E_F) can be approximated as

$$E_F = (E_M - q_M \cdot U_{\text{Bias}}) \cdot \frac{m_F}{m_M} + q_F \cdot U_{\text{Bias}} \quad (3.3)$$

where E_M is the energy of the parent molecule, q_M is the charge of the parent molecule, U_{Bias} is the bias, m_F is the fragment mass, m_M is the parent mass and q_F is the charge of the fragment. The expected time of flight (TOF) can then be calculated from simple mechanics. Alternatively expected TOF distributions can be found from simulations, which can include the physical extent of the bias potential and even a distribution of kinetic energy releases in a fragmentation process, see chapter 6.

In the ion trap mode, the electrodes E1-4 and X1-4 will be operated as a linear ion trap with the possibility to switch both electrode E1 and X1,

as described in section 3.4.

Three beams can be crossed in the plane spanned by the ion and photon beams velocity vectors in the region. For one ion beam and one laser beam the angle between ions and the laser can either be 45° or 90° , depending on the laser path used.

The profile and position of both ion and photon beams can be scanned simultaneously in the interaction region by inserting 1mm wide metal strip and moving the strip vertically through the beams while monitoring the intensities. This, of course, gives the intensity drop when blocking each 1mm section of the beam. The real beam profile (g_b), where b is ions (I) or photons (γ), can be found by deconvolution of the measured intensity profile of the beam (G_b) and the rectangular shape (s) of the metal strip blocking 1mm of the beam.

$$G_b(y) = \int g_b(y')s(y - y')dy' \quad (3.4)$$

3.6 Electron spectrometer

Just above and below the interaction region there are a series of electrodes and a multi channel plate (MCP) detector with a delay line anode (See section4.1).

Each set of electrodes can be operated in time of flight (TOF) mode or Velocity Map Imaging (VMI) mode. In TOF mode the electron energy can be measured directly, as the time it takes the electron to fly from the interaction region to the detector (14cm). With VMI mode the electrons' velocity transverse to the direction of the detector can be determined as the transverse distance the electron travels before it hits the detector.

The TOF mode is the normal mode of operation. By carefully choosing the voltages applied the electrons can be retarded and the TOF for a desired energy range can be extended to increase the resolution. However, for too broad distributions small energy differences can be hard to recognize. The proper retardation to apply will depend on the specific energies to measure and resolve.

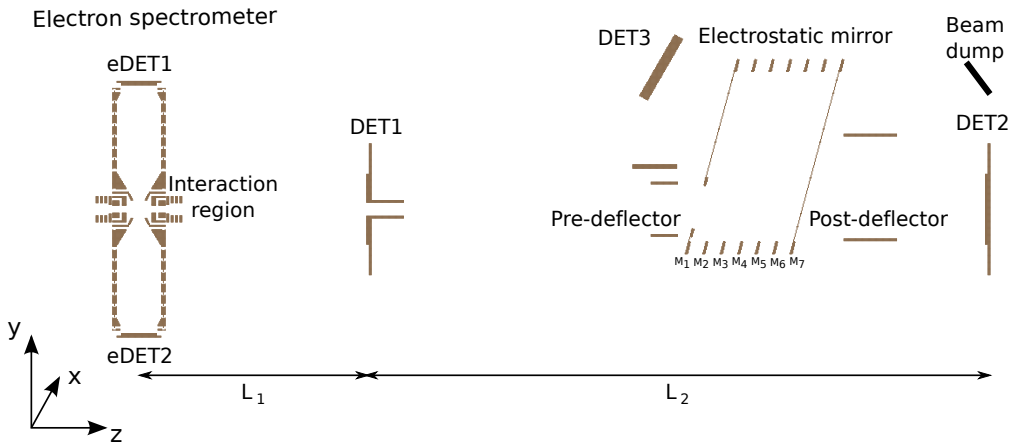


Figure 3.6: An illustration of the electrode configuration of the electron spectrometer, interaction and detection region of the TIFF setup. Ions arrive from the left and are crossed with with a photon beam at the center point of the interaction region. The interaction region are depicted in greater detail in Figure 3.5. An electron spectrometer are placed both above and below the interaction region whereby all electrons can be detected regardless of the direction of emission. DET1 has a central hole. This allows heavier particles to pass while light fragments with a not too small velocity perpendicular to ion beam can be detected. DET2 is normally reserved for detection of neutral, heavy fragments, while the electrostatic mirror deflects charged heavy fragments towards DET3. The setting of the mirror must ensure that the parent beam is dumped as far from any detectors as possible.

3.7 The detection region

After the interaction region (in the ion beams direction of travel) a detector with a central hole is placed, called DET1. See Figure 3.6. This causes ions with a low mass (1-2amu) and a good sized velocity perpendicular to the beam direction to impact on the detector, while ions with a higher mass will pass through the detector to arrive at the electrostatic mirror in the detection region.

The electrostatic mirror can bend the trajectories of charged ions towards DET3, while neutral fragments will pass unhindered to DET2. Fragments

with the opposite charge as the polarity of the mirror will of course pass through the mirror and be accelerated while inside the high potentials (\sim kV). By choosing proper potentials for the mirror the parent ion beam can pass through the mirror and be bent, by applying a voltage to the post deflectors, onto a phosphor screen, acting as a beam dump and a live feed to show the stability of the ion beam.

All three fragment detectors at TIFF are multi channel plate (MCP) detectors with delay line anodes (See section 4.1).

3.8 Free Electron Laser in Hamburg

The free electron laser (FEL) used at TIFF is the free electron laser in Hamburg (FLASH) at DESY.

FELs are accelerator based light sources and consist of an electron accelerator system and a linear single-pass undulator. An undulator is a series of alternating dipole magnets and forces charged particles to oscillate rapidly in the direction perpendicular to the direction of motion, hereby creating synchrotron radiation in the forward direction. As an electron bunch enters an undulator spontaneous photon emission (shot noise) occurs in the forward direction. With sufficient intensity these photons will interact with the electrons further along in the electron bunch, perturbing the electron distribution to be in phase with the light. Some electrons will gain and others lose energy, resulting in electrons piling up at intervals of the radiated wavelength described by

$$\lambda_r = \lambda_u \frac{1 + K^2}{2 \cdot \gamma^2} \quad (3.5)$$

where λ_u is the undulator period, γ is the relativistic parameter and K is the undulator strength parameter given by

$$K = \frac{e \cdot B_u \cdot \lambda_u}{2\pi \cdot m_e \cdot c}$$

where B_u is the r.m.s. value of the undulator field, e and m_e are the charge and mass of the electron, respectively, while c is the speed of light, [12]. Hence, the wavelength of the radiated photons can be adjusted either by

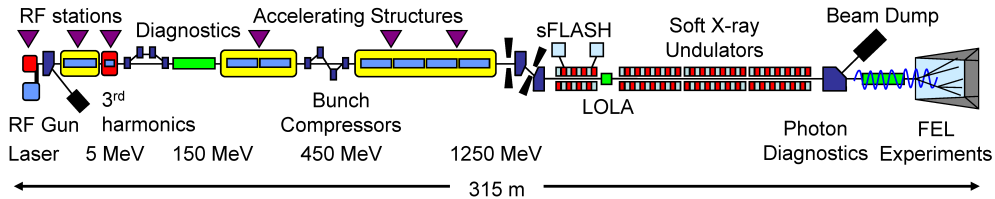


Figure 3.7: Schematics of the FLASH layout after the upgrade 2009/2010. [18]

changing the period of the undulator, the strength of the magnetic field or the kinetic energy of the electron bunches.

The bunching of the electrons is called micro-bunching and enhances the power gain and makes the radiation coherent, however, resulting in a chaotic intensity distribution within the photon bunch. The intensity gain depends exponentially on the undulator length ($L_{\text{Undulator}}$) until saturation [12]. The overall process is called Self-Amplified Spontaneous Emission (SASE) owing to the spontaneous nature of the initial radiation and for this reason each photon pulse will differ in intensity, spectral distribution and temporal structure [13].

It is possible to overcome the stochastic nature of the initial photon emission by seeding the undulator with photons tuned to the undulators resonance wavelength. Down to the ultraviolet range this is achievable with high harmonic generation from conventional lasers. However, for the extreme ultraviolet and x-rays range no conventional lasers exist. As demonstrated at LCLS it is thus possible to self-seed an FEL, by using a monochromator between two sections of undulators [16].

FLASH is a SASE FEL and has, since 2005, been operated as a user facility and provided laser-like radiation in the range $\lambda = 6.9\text{-}47\text{nm}$ with photon pulses energies of $E_{\gamma} = 10\text{-}50\mu\text{J}$ and some higher order harmonics e.g. third $\lambda \approx 2.3\text{nm}$ and fifth $\lambda \approx 1.4\text{nm}$ [13]. Construction of FLASH2 commenced in 2012 and is currently ongoing (spring, 2015). FLASH2 has a variable gap between the magnets in the undulator and is expected to produce photons in the range $\lambda = 4\text{-}80\text{nm}$ with single pulse energies of $E_{\gamma} = 1\text{-}500\mu\text{J}$ [17].

The FLASH setup is shown in Figure 3.7. From the accelerator end

Table 3.1: Overview of the characteristics of FLASH and the Nd:YAG laser.

	FLASH, [13]	Nd:YAG, [19]
Rate (Hz)	1-10	1-15
Pulses pr train	1-800	1
Effective rate	1-8000	1-15
Pulse duration	10-250fs	3-7ns
# photons pr pulse	10^{13}	10^{17} @ 1064nm
Photon energy, E_λ (eV)	180-26/	1.2 / 1064 / 28mJ
Wavelength, λ (nm) /	6.9-47 /	2.3 / 532 / 12mJ
Pulse energy, E_γ	10-50 μ J	3.5 / 355 / 4mJ
(average)	(3rd and 5rd harmon- ics of 13.7nm)	4.7 / 266 / 2mJ

FLASH consists of a RF electron gun and a pre-accelerator, hereafter the electron bunches enters a bunch compressor and 1GeV superconducting linear accelerator. After this the bunch energy is sufficient to start the SASE process. Optionally, the sFLASH section of FLASH1 can be used to seed the FEL process for some wavelength, but normally the photon production commences in the subsequent undulators. FLASH1 has 6 undulatory units, each $L_{\text{Undulator}} = 4.5\text{m}$ long with a fixed $L_{\text{Gap}} = 12\text{mm}$ gap permanent magnet device with a period length of $L_{\text{period}} = 2.73\text{cm}$ and a peak magnetic field of $B_{\text{Peak}} = 0.47\text{T}$ [12].

Before the newly generated photon beam enters the experimental hall it passes a magnet, deflecting the electron bunches to an electron beam dump. Along the photon beam line several diagnostic units are placed, which are used to optimize and control the beam. The last of these tools are a gas monitor and a gas attenuator. The monitor detects the intensity of the individual photon bunches and the attenuator can reduce the intensity using Nitrogen for wavelength between $\lambda = 19\text{-}60\text{nm}$ and a combination of xenon and krypton for the interval $\lambda = 9\text{-}19\text{nm}$. In the experimental hall the photon beam line branches out into two sections, one direct beam line (BL) and one with a plane grating monochromator (PG). Both branches are then further divided into more beam lines. The FEL can serve only one beam line at the time. The TIFF setup is placed at the PG2 beam

line about two meters before the FEL focus. At the location of TIFF the spot size of the photon beam is about $w = 1\text{mm}$, while the spot size in the focus is about $w = 50\mu\text{m}$, depending on wavelength and monochromator settings, [13].

The parameters of FLASH is summarized in Table 3.1.

3.9 Nd:YAG laser system

The Continuum Minilite laser is a compact Q-switched Neodymium doped Yttrium Aluminium Garnet (Nd:YAG, $\text{Nd:Y}_3\text{Al}_5\text{O}_{12}$) laser made as a power supply unit and a laser head with a closed water cooling system. The laser has a pulse energy of $E_\gamma = 28\text{mJ}$ at $\lambda = 1064\text{nm}$, and is supplied with crystals to obtain $\lambda = 532\text{nm}$, $\lambda = 355\text{nm}$ and $\lambda = 266\text{nm}$ at pulse energies up to $E_\gamma = 12\text{mJ}$, $E_\gamma = 4\text{mJ}$ and $E_\gamma = 2\text{mJ}$, respectively, with a repetition rate of 1-15Hz and a pulse length of 3-7ns. For an overview of the Nd:YAG laser, see Table 3.1.

The setup to focus and overlap the Nd:YAG laser with the ion beam is shown in Figure 3.8. The HeNe laser pointer is a low power laser and is

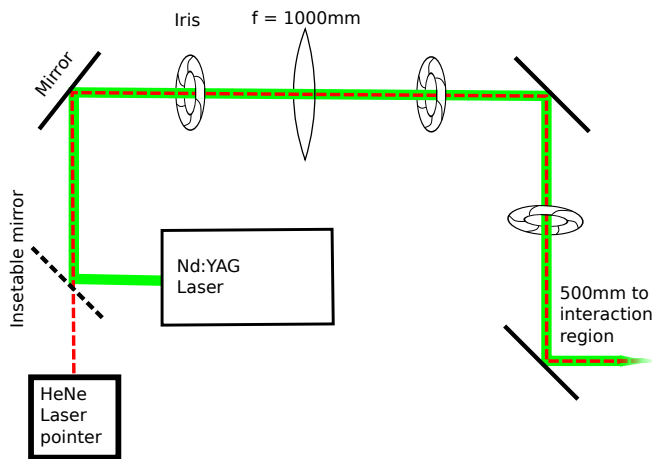


Figure 3.8: Mirror and lens configuration for transporting and focussing the photons from the Nd:YAG laser in the interaction region.

used to make a first adjustment of the mirrors, so that when the insertable mirror is raised and the Nd:YAG laser is turned on, the light will be guided to the interaction region. In order for the Nd:YAG laser to follow exactly the same path as the HeNe laser three irises are inserted.

Data acquisition and analysis

The data acquisition (DAQ) process at TIFF, from an impact on a detector to the information is pre-processed and ready for a kinematic analysis, is described in the following chapter. This will include the working principle for a multi channel plate (MCP) detector with a delay line anode and the digitalization scheme implemented. The measured values are digitalized with time-to-digital converters (TDC) or analog-to-digital converters (ADC) and send on to be saved in a computer. The individual channels from the TDCs and ADCs are then ordered to constitute the physical impacts on the detectors. A short overview of the DAQ process is given in Figure 4.1.

The implemented DAQ scheme systematically alternates between having ions, photons, neither or both ions and photons present in the interaction region to determine the actual number of background-subtracted, photo-induced impacts.

4.1 Particle and photon detection

The data to obtain from an ion beam experiment can be boiled down to a time of flight (TOF) and an impact position relative to the point of interaction. The obtainable temporal and positional resolution will depend on the hardware installed, and there is a handful of different detectors to choose from. Some detectors will give a high temporal resolution and only the positional information that the detector was hit (Channeltron, [20, 21]).

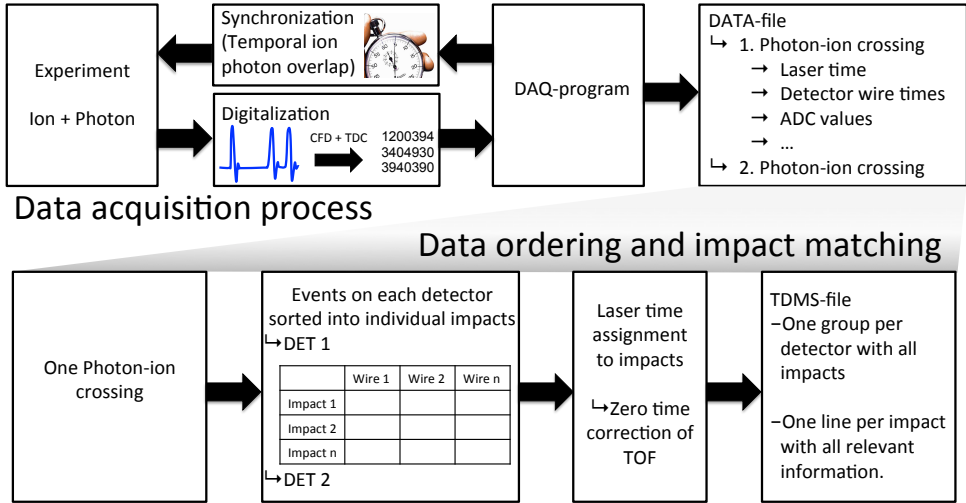


Figure 4.1: Flowchart of the data process from acquisition to the first analysis step. The DAQ program synchronizes the timing of the photon and ion beams to ensure a temporal overlap. The analog signals from an experiment are digitalized and stored to a data file with the information from all individual channels of all the TDCs and ADC. After (or during) an experiment the information in the data files are calibrated and sorted to constitute physical impacts.

Some can record the position of several simultaneous impacts while not directly giving the time associated with each impact (MCP with a phosphor screen and camera). A few can give high temporal and positional precision, while still handling almost simultaneous impacts (MCP with delay line anode [22]).

All detectors at TIFF are RoentDek MCP detectors with delay line anodes, which constitute fast, high resolution position and time detectors [23].

A MCP is a $\sim 1.5\text{mm}$ slab of a highly resistive material ($R > 10^7\Omega$) with many, regularly spaced channels leading from one side to the other, [24]. The channel diameter is around $25\mu\text{m}$ and the center to center distance is around $32\mu\text{m}$ [23]. The channels have a small angle to the plate surface ($\sim 8^\circ$), so when a particle impacts on the plate, and hits a pore, the tilt of

the pores ensures that the particle hits the channel wall, thereby knocking off electrons. By applying a high voltage across the MCP, the electrons will be accelerated into another part of the channel wall, knocking off more electrons, starting a cascade effect down the pore and resulting in a small electron cloud which leave the back side of the MCP. To obtain a larger pulse at the expense of a wider time distribution, MCPs are often stacked with an opposite tilt between two adjacent plates. Two MCPs are called a chevron stack, while three are called a z-stack.

The activated channels will have a recovery time (dead time) of $T_{\text{Dead}} \sim 10\text{ms}$ before they are ready for the next impact, however due to the larger number of holes, working almost independently, the effective dead time is $T_{\text{Dead, Eff}} \approx 10\text{ns}$ if the same holes are not activated twice, [24].

Though there are many holes on a MCP there is a finite area between holes, which leads to a maximal geometrical efficiency of a MCP of roughly $\epsilon = 0.5$, though some have reported higher efficiencies explained by capture of secondary electrons, from impact on the MCP surface, by the electric field at the surface [24].

An impact will correspond to a voltage change as electrons are kicked free, and the power supply has to recharge the plate. Monitoring either the front or back side of the MCP will give a precise time of impact (T_B). The time difference between the front and back signal corresponds to the travel time of the electrons through the MCP, roughly 2ns for a 3mm thick chevron MCP stack with a 3kV bias applied.

A delay line anode consists of a long wire (order of meters) wrapped up to form two parallel planes of closely spaced, parallel wires. Between the two planes a copper plate is placed to block the electron cloud from hitting both the upper and lower layers [23]. When a cloud of electrons hits the delay line, an electrical pulse is induced and transmitted to both ends of the wire.

Each particle impact on a detector will (theoretically) give rise to a signal on the MCP back at time (T_B) and a signal at each end of delay line n at time T_{n1} and T_{n2} , respectively. This is schematically shown in Figure 4.2. In order to locate a position on the detector at least two non-parallel delay line wires must be activated.

The zero point for the time in the experiment is defined by the photons arriving in the interaction region. The laser time (T_L) is recorded by

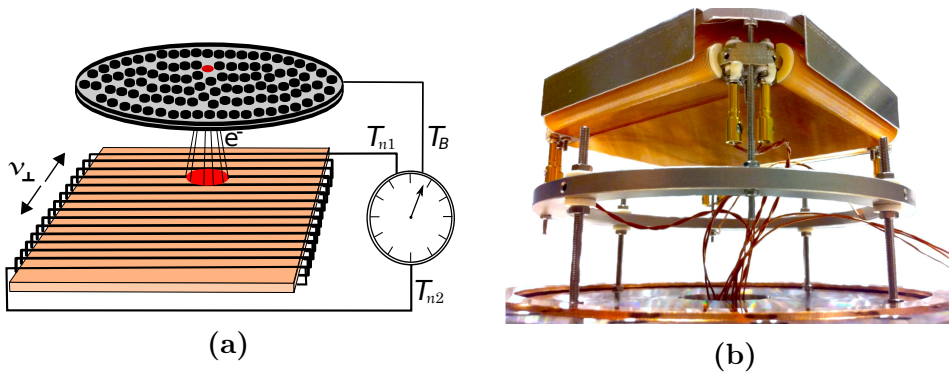


Figure 4.2: (a) Schematics for a MCP detector with a delay line anode. When a particle impacts on the MCP an electron cloud is generated and accelerated onto the delay line anode where a signal is induced and flows to each end of the delay line. (b) A picture of the delay line anode of the TIFF detector DET3 just after mounting on a CF150 flange and before it was installed in the vacuum chamber.

dumping the photons on a copper plate shortly ($\sim 2\text{m}$) after the interaction region. The distance, of course, gives a small offset of $T_d = 0.7\text{ns}$. The photons will detach some electrons and a voltage variation is observed.

4.1.1 Detector DET1

To facilitate the central hole in DET1 the delay line anode consist of three layers of wires. At the central 2mm of each layer no wires are wound and the angle between the wire direction of any two layers is 60° . This allows an open hexagon in the center of the detector with a minimum radius of $r_{i,\text{min}} = 1\text{mm}$. As only two layers are needed to calculate the position of an impact the entire detector surface outside a six pointed star is operational [6].

4.2 Digitalization

An impact on a MCP detector can be identified as a certain voltage variation on all wires. However, continuously analyzing the voltages on all

wires to recognize these variations is a tremendous task.

Firstly, in order to resolve the variation pattern, the sample rate must be sufficiently high. To resolve 1ns the sample rate must be at least $4 \cdot 10^9$ samples/s and preferably higher.

Secondly, the shape of the variation depends on the particle energy, the voltages applied and for the delay line wires to some extent on where on the detector the position of impact occurs. Hence, the algorithm to recognize the impacts must not be too rigid.

This, of course, has to be done for all wires and means that a lot of computations must be done in a very short amount of time to continually read out the impact positions.

Another option would be to simply store the entire sample trace, accumulating a vast amount of data to be processed later. But then it would not be possible to verify the obtained data during an experiment and make appropriate corrections in case of any errors or malfunctions.

At TIFFF a third option is implemented. Basically, the voltage variation is a peak on the otherwise constant voltage level. Small noise fluctuation can be eliminated by setting a lower threshold which a peak has to surpass.

If the pulse shape or height varies, some uncertainty will be introduced if the impact times are extracted simply by crossing a potential threshold. However, the pulse rise time for each wire is almost constant and using a constant fraction discriminator (CFD) will give a time fixed at a set percentage of the pulse height.

The CFD transforms the incoming signal to a bipolar signal with height and shape defined by the rise time of the original pulse. This is done by first splitting the signal in two parts. One part is delayed and inverted while the other is scaled. Finally, the two halves are subtracted and the set percentage of the pulse height is obtained as the signal changes sign.

The output from the CFD is sent to a time-to-digital converter (TDC) where the signal arrival time is recorded using an internal clock. The values stored in the TDC can be transferred directly to a computer for further processing, including a conversion from the TDC clock to SI time units.

4.3 Sorting impact times

As mentioned, the information to obtain from an ion beam experiment is the impact time and the position of the particles impacting on a detector. So far the values obtained have been the signal arrival times on different wires. This, of course, gives the absolute impact time for each particle on a detector relative to the start of the internal TDC clock, but a more desirable value would be the particles time of flight (TOF) from the interaction region to the detector. Furthermore, the signal arrival times at the end of the delay line anode have to be translated to a position on the detector.

The TOF of a particle from the interaction region to the detector is given by the difference between the impact time of the MCP back (T_B) and the laser time (T_L)

$$\text{TOF} = T_B - T_L + T_d. \quad (4.1)$$

where T_d is a possible wire delay difference for signals coming from the photon dump and the MCP detector. A wire delay can occur due to different total wire length and different processing time in the electronics before the TDC. If scattered photons are seen on a MCP detector the wire delay can be calibrated directly.

The position (x_n) of impact in one direction (n) can be calculated from the length of the delay line, the time difference between the two ends of that wire and the signal speed in the wire. It can, however, be more convenient to use the signal speed perpendicular to the wrapped wire (v_\perp) and calculate the impact position relative to the midpoint of the wrapped wire

$$x_n = (T_{n2} - T_{n1} + T_O) \cdot v_\perp \quad (4.2)$$

where T_{n1} and T_{n2} are the arrival times at the wire end and T_O is a calibration offset to compensate for possible delay differences. To get a two dimensional position of the impact at least two non-parallel wires must be used.

The signal speed perpendicular to the wire direction is calibrated to the individual delay line and depends on the diameter of the detector. For a detector with a diameter of $\varnothing = 40\text{mm}$ the signal speed is of the order of $v_\perp = 1.4 \frac{\text{mm}}{\text{ns}}$, while it for a $\varnothing = 80\text{mm}$ detector is around $v_\perp = 1.1 \frac{\text{mm}}{\text{ns}}$ [23].

To sum up for a particle impacting on a detector the TOF can be found using equation (4.1), while the impact position is given by equation (4.2). To perform the time and position calculation for an impact, the arrival time for all detector wires and the photons must be combined. However, the time values recorded by the TDC are not necessarily properly sorted. E.g. some values might be missing or some random noise might have passed the threshold. All the apparently unrelated wire times from all wires of one detector must therefore be arranged into individual, physical impacts containing the relevant information.

A laser time (T_L) can fairly easily be assigned to each MCP back time (T_B) based on the expected TOF from the interaction region to the detector surface. The TOF of particles to the different detectors range between 1-11 μ s, depending on the distance to the detector as well as mass and kinetic energy of the particles. The temporal length of ion pulses at TIFF are around 2.5 μ s and the temporal distance between successive photon-ion crossings are 5 μ s. Therefore only one photon pulse will match the TOF of a particle with known mass and the kinetic energy of the fast ion beam.

The total time for an induced signal to reach both ends of a delay line wire is constant, within a small variation (δ), and can be calculated as the sum of the wire times (T_{n1} and T_{n2}) with the time of the MCP back (T_B) as a time zero point. Hence T_{n1} , T_{n2} and T_B must satisfy

$$T_{\text{sum}} - \delta < T_{n1} + T_{n2} - 2 \cdot T_B < T_{\text{sum}} + \delta \quad (4.3)$$

where δ is in the order of 20ns. From this criteria the optimum wire combinations can be found as the one with the smallest value of δ .

To minimize the number of calculations, a faster pre-sorting is currently incorporated, requiring only that the time difference between any two wire times (T_i and T_j) must be less than the traveling time through the wire (T_W) for them to match

$$|T_i - T_j| < T_W \quad (4.4)$$

The search picks the first pair of wires which satisfy the condition and move on to find the next pair, until all wire times are either paired to constitute impacts or discarded as belonging to incomplete impact sets. The obtained pairs are then confirmed to actually satisfy equation (4.3) before being accepted.

The pre-sorting routine might pair up wires incorrectly if two impacts occur in a short time interval on the same detector. The validity of the pre-sorting can be tested by looking at two particles impacting on a detector in different areas almost at the same time. Assume the first particle hits the x-wire close to the x_1 end and the second particle hits the x-wire close to the x_2 end shortly after, see Figure 4.2. Then the signals leaving the detector on x_1 will first be the signal from the first particle and then from the second. Here, the pre-sorting will work just fine. But at the x_2 end the signal from the second particle will leave the wire first and in the pre-sorting this signal will be paired to the x_1 arrival time of first particle. Hence, the position calculation for these two impacts will be mixed up. The critical time (T_{critical}) to avoid this will then be the time it takes a signal to travel from one side of the detector to the other. e.g. for a 80mm delay line with a speeds of $v_{\perp} = 1.1 \frac{\text{mm}}{\text{ns}}$ [23] the critical time will be

$$\begin{aligned} T_{\text{critical}} &= \frac{\varnothing_{\text{detector}}}{v_{\perp,80\text{mm}}}, \\ &= 73\text{ns} \end{aligned} \tag{4.5}$$

This constitutes a multi-impact dead time for the pre-sorting and when two impacts are recorded within $T_{\text{critical}} = 72\text{ns}$ the pre-sorting should not be used. It should, however, be mentioned that even with the proper sorting, a MCP with a two delay line anode has a finite dead time between successive impacts, which depending on the relative position of the impacts. The dead time can be greatly reduced by introducing a third delay line and maintaining an angle of 60° between each wire dimension.

With the wire times and associated laser time grouped, the impact position on the detector and TOF from the interaction region to the detector surface is easily calculated. As the distances from the interaction region to the detectors are known, the velocities and thereby the momenta and kinetic energies of the fragments can be found from simple mechanics as explained in section 2.5.

4.4 Experimental scheme

The background-subtracted, photon-induced signal from a photon-ion interaction can statistically be obtained by measuring the background contribution directly. This is accomplished by running the data acquisition successively in four different modes:

- Photons&Ions
- Ions only
- Photons only
- Dark.

In the Photons&Ions both photons and ions are present, while in Ions only the photons are absent and similarly the ions are absent in Photons only mode. Neither photon or ion is present in the Dark-mode. The background-subtracted, photo-induced signal can then be obtained as

$$\text{Signal} = \text{Photons\&Ions} - \text{Ions only} - \text{Photons only} + \text{Dark} \quad (4.6)$$

The counts in the Dark mode are present in all the other modes and are hence added to compensate.

FLASH delivers photons in trains with for instance 50 bunches per train and a repetition rate of 10Hz for the trains. Each train will correspond to a single acquisition mode. This sets the limit for the number of Photon&Ions and Photons only modes per second. The Ions only and the Dark mode are interlaced between the photon trains.

The data collected in the electronics is transferred to a computer between each mode. The computer collects the information from 500 modes and stores it as a raw data file. With a 20Hz acquisition rate this amounts to roughly 25s/file. Each data file consists of a header specifying current values for the setup in the current run and a body where the actual data is stored in an event based format. One event corresponds to one acquisition mode.

As the photons are absent in both the Ions only and Dark mode, a note regarding laser time assignment in these modes must be made.

In the Photons&Ions and Photons-only modes the laser time is assigned to each impact by requiring the laser time to be within a time window defined by the expected TOF.

In the Ions-only and Dark modes the average laser time from the Photons&Ions and Photon-only modes can be used. This will give a small jitter. Alternatively a logical trigger placed at the laser time can be used. This pseudo laser time was implemented at the TIFF station in the spring of 2012 in order to remove the jitter.

Coincidence analysis

Two or more particles detected simultaneously are said to be detected in coincidence. Particles originating from the same reaction and detected simultaneously can be said to be detected in true coincidence, while particles originating from different reactions, but detected simultaneously, can be said to be detected in random coincidence. In an experimental setting with pulsed photon and ion beams “simultaneously detected” must be perceived as “emerging from the same photon-ion crossing and detected after the distance to the detector(s) is transversed”. Therefore, all particles detected from the same photon-ion crossing will be detected in real coincidence, whether it is a true or random coincidence.

A coincidence analysis separates particles detected in true coincidence from random coincidences as well as uncorrelated, individually detected particles. A coincidence analysis is a powerful tool for both isolating a weak breakup process from a large, unrelated background and for gaining more information about a reaction by combining the information obtained from each detected particle.

A coincidence analysis can be implemented directly into the data acquisition method. Either by collecting information only when more particles are detected or by allowing particles to access a detector only if some prerequisite are met. For instance, this has been done in a photoelectron-photoion coincidence study. If an electron with a specified kinetic energy was detected voltages were rapidly applied to allow ions with a certain

mass and charge to reach a detector otherwise inaccessible to ions [25]. To estimate the number of random coincidences the voltages were applied a second time without detecting an electron first. More precisely this was done $40\mu\text{s}$ after the first pulse to let uncorrelated ions reach the detector. One of the advantages with this approach is a lower load on the detectors and electronics, which can be crucial for instance when the count rates are comparable to the multi hit capabilities of the setup. The obvious disadvantage is that only expected coincidences will be tested while information of unpredicted outcomes are inaccessible.

A software-based implementation of a coincidence analysis can be a superior alternative if the detectors and data collection system can handle a sufficiently high count rate. This allows for testing several coincidence schemes after the data has been acquired.

In this chapter, the software based implementation of a coincidence analysis to study photoionization and photofragmentation at TIFF will be described.

5.1 Analysis scheme

Consider a photofragmentation reaction where a molecule AB absorbs a photon (γ) and dissociates, i.e.



Assume that each fragment (A and B) will be detected on separate detectors (DET1 and DET2, respectively) with a finite efficiency $\epsilon \leq 1$. The detection efficiency will cover both the detection efficiency of the detector, and the transmission from the point of reaction to the detector. $\epsilon = 1$ would imply no transmission losses and a perfect detector with a 100% acceptance. The coincidence analysis must identify the fragments in true coincidences ($A + B$) and suppress random coincidences as well as singularly detected A or B ($\epsilon < 1$), particles from collisions with residual gas and particles from other photoinduced reactions, which do not produce both A and B .

The requirement that can be invoked in an experimental setting for particles to be detected in coincidence is that they must emerge from the same photon-ion crossing, they must be in real coincidence. This will

selectively identify particles detected from the same reaction and in true coincidence only if a single reaction is possible in each photon-ion crossing and all particles are successfully detected $\epsilon = 1$. But for moderate reaction rates two or more reactions can occur in the same photon-ion crossing and some random coincidences between uncorrelated fragments from different reactions will inevitably be registered.

Observables like momentum and energy can be used to differentiate between true and random coincidences. Requiring momentum conservation will efficiently reduce the random contribution, but to fully separate the true coincidences from the random coincidences a statistical approach is necessary.

5.1.1 The algorithm

Assume all reactions have the same reaction probability in each photon-ion crossing. This will imply that the detection probability for each particle species will be constant for all crossings and therefore the probability for a particle on DET1 to be detected in random coincidence with any particle on DET2 will be invariant to the particles actually belonging to the same photon-ion crossing.

The actual analysis can be boiled down to two steps:

1. Pair each particle detected on DET1 with all particles detected on DET2 in the same photon-ion crossing. These real coincidence pairs will contain both the true and random coincidences.
2. Pair each particle detected on DET1 in one photon-ion crossing with all particles detected on DET2 in the next crossing. This will give an estimate of the random contribution.

The distribution of an observable (O) like time of flight (TOF), position etc from true coincidences can statistically be found as the difference between the real and random coincidences;

$$\begin{aligned} O_{\text{True}} &= O_{\text{Same photon-ion crossing}} - O_{\text{Two successive crossings}} \\ &= O_{\text{Real}} - O_{\text{Random}} \end{aligned} \tag{5.2}$$

5.2 Proof of concept

The viability of the algorithm can easily be verified through a simulation where all parameters are controllable and can be monitored. To ensure a realistic setting, parameters will be chosen from an experiment at TIFP; the photofragmentation at 42nm of the protonated water dimer (H_5O_2^+), but only including the binary breakup channel ($\text{H}_3\text{O}^+ + \text{H}_2\text{O}^+ (+ e^-)$) (See chapter 9). The kinetic energy of the initial ion beam will be $E_{ion} = 4.2\text{keV}$ with a total ion current of $I_{ion} = 1\text{nA}$. The mass of the parent ion is $m_{ion} = 37u$. This correspond to the linear density of ions

$$l_{ion} = \frac{I_{ion}}{q_{ion} \cdot \sqrt{2E_{ion}/m_{ion}}} = 421.7\text{cm}^{-1} \quad (5.3)$$

The photon pulse energy will be $E_\gamma = 25\mu\text{J}$ and photon energy $E_\lambda = 29.5\text{eV}$. This corresponds to $N_\gamma = E_\gamma/E_\lambda = 5.3 \cdot 10^{12}$ photons per pulse. A typical reaction cross section is $\sigma_{\text{Reaction}} = 10^{-18}\text{cm}^2$ and the photon ion beam overlap factor has been set to $F = 8\text{cm}^{-1}$. From these values the reaction rate can be found to be (See 2.20)

$$R_{\text{Reaction}} = N_{ph} \cdot l_{ion} \cdot F \cdot \sigma_{\text{Reaction}} = 0.018 \quad (5.4)$$

The number of reactions in the photon-ion crossings will be assumed to follow a Poisson distribution with mean $\lambda = R_{\text{Reaction}}$.

The detection efficiency will be chosen to be $\epsilon_{\text{Reaction}} = 0.33$ including the ion transmission as well as the efficiency of the detector. This gives a detection probability of $P_{\text{Reaction}} = R_{\text{Reaction}} \cdot \epsilon_{\text{Reaction}} = 5.9 \cdot 10^{-3}$.

Finally, the kinetic energy released in the process have been set to follow a Gaussian distribution with a mean $\mu = E_{\text{KER}} = 3\text{eV}$ and a standard deviation of $\sigma = 0.2\text{eV}$.

The two fragments (H_2O^+ and H_3O^+) are detected on separate detectors DET1 and DET2 located, respectively, 0.97m and 1.1m from the point of reaction. The distances have been chosen to have a clear time separation between the two species and both detectors are assumed to be time and position sensitive.

Figure 5.1(a) shows the time of flight (TOF) distribution for the two fragments (H_2O^+ and H_3O^+) after $5 \cdot 10^6$ photon-ion crossings, black and

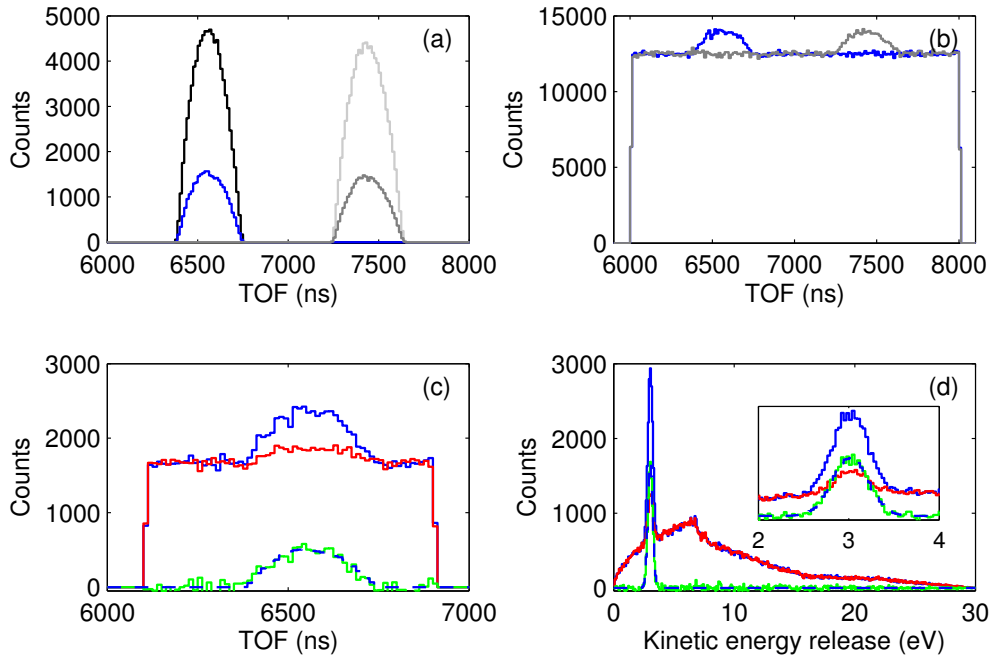


Figure 5.1: Simulation of a fragmentation of $H_5O_2^+$ to the two body breakup channel ($H_3O^+ + H_2O^+$) with a kinetic energy release of $E_{KER} = 3 \pm 0.2\text{eV}$, a fragmentation probability of $R_{\text{Reaction}} = 0.018$, a detection probability of $\epsilon_{\text{Reaction}} = 0.33$ and a probability of $P_{\text{Background}}(6-8\mu\text{s}) = 0.4$ to detect random impacts. (a) TOF distribution for all fragments (Black: H_2O^+ , light gray: H_3O^+) from the reaction and for the fragments actually detected (Blue: H_2O^+ , dark gray: H_3O^+). (b) The TOF distribution for the detected particles including an uncorrelated, uniform background. The blue curve is DET1 and the gray is DET2. (c) The resulting TOF distribution from a coincidence analysis between DET1 and DET2. The blue curve shows real coincidences on DET1, while the red curve shows the random coincidences on DET1. The green curve is the difference and the dashed blue shows the number of detected H_2O^+ on DET1 but is scaled with the efficiency to detect a H_3O^+ on DET2. (d) The kinetic energy release for the coincidence pairs. The blue curve is the real coincidences while the red curve is the random contribution. The green curve clearly follows the dashed blue curve depicting a Gaussian distribution with mean $\mu = 3\text{eV}$, standard deviation $\sigma = 0.2\text{eV}$ and an amplitude corresponding to the number of detected fragments in coincidence, see the insert.

light gray curve, respectively. The width of the two TOF distributions are $(6749\text{ns} - 6370\text{ns}) = 379\text{ns}$ and $(7640\text{ns} - 7234\text{ns}) = 406\text{ns}$. With a detection efficiency of $\epsilon = 0.33$ only a third of the fragments will be properly detected, the blue and dark gray curve, respectively.

To demonstrate the capabilities of the coincidence analyses a large number of random impacts have been mixed with the detected impacts from the fragmentation reaction as shown in Figure 5.1(b). The probability of random impacts on the detector has been set to $P_{\text{Background}}([6; 8]\mu\text{s}) = 0.4$ per photon-ion crossing. The impact position and time will constitute uniform distributions.

In the actual time interval of H_2O^+ impacts (TOF = $[6370; 6749]\text{ns}$), the probability of random impacts will amount to

$$P_{\text{Background}}(0.379\mu\text{s}) = P_{\text{Background}}([6; 8]\mu\text{s}) \cdot \frac{379\text{ns}}{2000\text{ns}} = 0.08. \quad (5.5)$$

This is a factor of $P_{\text{Background}}(0.379\mu\text{s})/P_{\text{Reaction}} = 13$ higher than the probability for detecting a single fragment from the two body breakup. Even so, the temporal position of the fragments can clearly be seen on top of the uniform distribution of random impacts.

At this point, the simulated experiment is completed and the recorded impacts are ready for a coincidence analysis. However, the number of random pairs can be greatly reduced by filtering the impacts. To this end only impacts in the time interval $t_{\text{DET1}} = 6.1\text{-}6.9\mu\text{s}$ and $t_{\text{DET2}} = 7.1\text{-}7.9\mu\text{s}$ on DET1 and DET2, respectively, will be passed to the analysis.

The result of the coincidence analysis is shown in Figure 5.1(c). The blue curve shows the TOF distribution of impacts on DET1 in real coincidence with an impact on DET2. This signal, of course, includes both the true and random coincidences. The red curve shows the fragments detected on DET1 in random coincidence with an impact in the following photon-ion crossing on DET2. The green curve shows the difference corresponding to true coincidences. The dashed blue curve is the TOF distribution of detected H_2O^+ fragments scaled with the efficiency to detect a H_3O^+ ($\epsilon_{\text{Reaction}} = 0.33$). The green curve clearly follows the dashed blue curve and fluctuates around zero outside the time interval of the H_2O^+ -fragments.

As a final control the released kinetic energy has been calculated for each coincidence pair for both the real and random output of the coincidence

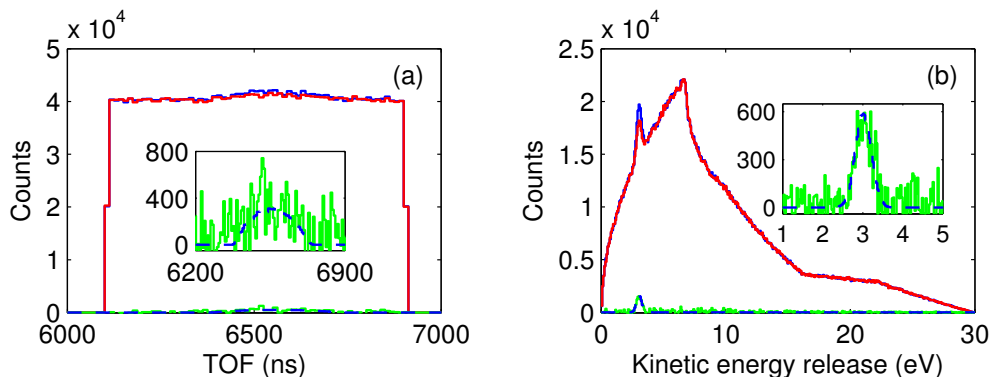


Figure 5.2: Simulation of a fragmentation of $H_5O_2^+$ to the two body breakup channel ($H_3O^+ + H_2O^+$) with a kinetic energy release of $E_{KER} = 3 \pm 0.2\text{eV}$, a fragmentation probability of $R_{\text{Reaction}} = 0.018$, a detection probability of $\epsilon_{\text{Reaction}} = 0.33$ and a $P_{\text{Background}}(6-8\mu\text{s}) = 2$ probability of random impacts. (a) The TOF distribution. The signal of true coincidences (green curve) are close to the noise limit. (b) The distribution of released kinetic energy. A small, but distinct structure can be seen around $E_{KER} = 3\text{eV}$.

analysis. The procedure to calculate the released kinetic energy is described in section 2.5. The released kinetic energy distributions are shown in Figure 5.1(d). The blue curve represents the real coincidence pairs and the red curve represents the estimation of the random contribution. The green curve is the difference. The dashed blue curve shows a Gaussian distribution with mean $\mu = 3\text{eV}$ and standard deviation $\sigma = 0.2\text{eV}$. The number of points chosen from the Gaussian distribution are given by the sum of $5 \cdot 10^6$ numbers following a Poisson distribution. Just like the number of fragmentation reactions in the simulated experiment. The histogram of the Gaussian distribution has then been scaled by the efficiency to detect both fragments $\epsilon_{\text{Reaction}}^2 = 0.11$. As illustrated with the small inset, the green curve truly follows the expected dashed blue curve and the estimation of the number of random impacts seems to be very precise. Note that the inset has a bin size of 30meV, while the full figure has a bin size of 86meV.

5.2.1 Testing the limit

To test the limits of the coincidence analysis the simulated experiment has been repeated with the probability of random impacts being increased by a factor of 5 to $P_{\text{Background}}(6\text{-}8\mu\text{s}) = 2$. On average, two random impacts will occur in each photon-ion crossing and with a uniform TOF distribution approximately one impact will occur in the time intervals $t_{\text{DET1}} = 6.1\text{-}6.9\mu\text{s}$ and $t_{\text{DET2}} = 7.1\text{-}7.9\mu\text{s}$. Recalculating the ratio between the probability to detect a random particle and a photofragment will yield a factor of $P_{\text{Background}}(0.379\mu\text{s})/P_{\text{Reaction}} = 65$ for this case.

The results from the coincidence analysis are shown in Figure 5.2. Figure 5.2(a) and (b) directly corresponds to Figure 5.1(c) and (d), respectively.

In Figure 5.2(a) the distribution of true coincidences are almost in the noise limit. The height of the expected signal (the dashed blue curve) has a maximum of $N_{\text{expected}} = 311$ counts at $TOF = 6.54\mu\text{s}$. In comparison the number of counts in real and random coincidence are $N_{\text{Real}} = 42 \cdot 10^3$ and $N_{\text{Random}} = 41.6 \cdot 10^3$, respectively. This gives an uncertainty of the true coincidences of $\sigma(N_{\text{True}})\sqrt{N_{\text{Real}} + N_{\text{Random}}} = 289$ counts. And finally the number of true coincidences are $N_{\text{True}} = 446 \pm 289$ counts.

A more distinct surplus of true coincidences can be seen in the released energy distribution in Figure 5.2(b) due to the small deviation of the released kinetic energy ($\sigma = 0.2\text{eV}$). Here the number of counts are $N_{\text{expected}} = 580$, $N_{\text{Real}} = 19.7 \cdot 10^3$ and $N_{\text{Random}} = 18.2$. This gives $N_{\text{True}} = (1.5 \pm 0.2) \cdot 10^3$ counts of true coincidence pairs.

The relatively sharp structure of the released kinetic energy can be used to reduce the random contribution to the TOF distribution. By only allowing coincidence pairs with a total released kinetic energy between $E_{\text{KER}} = [2; 4]\text{eV}$ a more pronounced signal can be located in the TOF distribution, as shown on Figure 5.3. At $TOF = 6.54\mu\text{s}$ the number of true coincidence counts are $N_{\text{True}} = 669 \pm 162$ with the kinetic energy filtering.

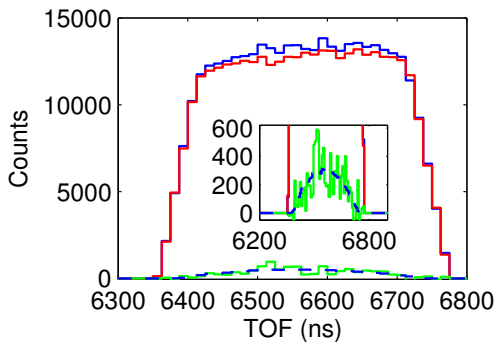


Figure 5.3: Simulation of a fragmentation of $H_5O_2^+$ to the two body breakup channel ($H_3O^+ + H_2O^+$) with a kinetic energy release of $E_{KER} = 3 \pm 0.2\text{eV}$, a fragmentation probability of $R_{\text{Reaction}} = 0.018$, a detection probability of $\epsilon_{\text{Reaction}} = 0.33$ and a $P_{\text{Background}}(6-8\mu\text{s}) = 2$ probability of random impacts. By filtering the data to only allow impact pairs with a total kinetic energy between 2 and 4eV, a large part of the random contribution can be removed.

5.3 Discussion

As demonstrated, the coincidence analysis can isolate fragments from a single reaction, if at least two fragments are detected either on two different detectors or in different time intervals on the same detector. The fundamental assumption is that the detection probabilities are constant for successive photon-ion crossings. Even if the photon or ion beam characteristics drift slowly during an experiment, this will still be fulfilled as only two successive photon-ion crossings are involved. If the photon or ion intensity varies between successive photon-ion crossings the detection probabilities will vary.

As the TIFF setup is located at FLASH, a self-amplified spontaneous emission free electron laser (SASE FEL), the photon pulses intensity, position, timing and energy spectrum fluctuates even within a single photon pulse. Given the statistical approach, the requirement of “constant reaction probabilities” in each photon-ion crossing can readily be softened to a constant average reaction probability. This will indeed be the case for long measurements with 10^6 or more photon-ion crossings.

A detection probability of $P_{\text{Background}}(6-8\mu\text{s}) = 2$ random impacts per photon-ion crossing is close to the extreme upper limit, to achieve a meaningful output from the coincidence analysis with a reaction probability of $P_{\text{Reaction}} = 5.9 \cdot 10^{-3}$. The coincidence analysis might be unsuccessful for

this high a count rate of random impacts if the distribution of observables from a fragmentation reaction is less ideal than in the presented simulation, and does not have any clear structure to distinguish it from the random impacts. Two photoinduced reactions with high count rates also pose a problem, though detection probabilities in the order of unity for actual photoinduced and ion related reactions appears very unlikely for ion currents in the order of 1-50nA.

A lower limit to the detection probability of random impacts does not really apply to the coincidence analysis. In this case a reaction will seldom happen and hence the random coincidences will only give a small contribution. If the reaction probabilities are also low it will be very unlikely for two reactions to happen in the same photon-ion crossing. The random contribution will be close to non-existing and the analysis will only return true coincidences.

The method can be extended to find coincidences between more than two particles, but the estimation of the random coincidences will require some attention.

For three bodies this can be done with the two body approach by making two pairs with a single particle species in both, and only accepting the random and real coincidences when both pairs are present. For the apparently real contribution this will work out flawlessly. But for the estimation of the random contribution to make a non-zero output this would imply that two of the three bodies must be detected in coincidence in the successive photon-ion crossing. If true two body coincidences are present this could bias the random estimation.

To determine which scheme best describes the random contribution for more than two bodies some further simulation must be performed.

Simulations

When working with ion beam lines the complex electric fields can be hard to describe analytically. Hence, to estimate the voltage to apply to each electrode of the beam line or after an experiment to interpret the acquired data a simulation tool is fundamental. This purpose has been fulfilled by SIMION 8.0 [26], a commercial, numerical software package developed by Scientific Instrument Services (New Jersey, USA).

6.1 SIMION

SIMION is a numerical software package with a graphical user interface for simulating charged particle optics and capable of calculating static or radio frequency (RF) electric and magnetic fields. The ion trajectory simulation capabilities have been utilized in electrostatic potentials only.

In SIMION the ion optical elements are defined and assembled on a two or three dimensional discrete grid, where the location, shape and potential of all elements are defined by marking the required points on the grid as electrodes with the required potential. In the space between the elements no charge can occur and, hence, the electrical fields must obey Laplaces equation

$$\Delta \vec{E} = 0 \tag{6.1}$$

, where $\Delta = \nabla^2$ is the Laplacian operator and \vec{E} is the electric field. In

SIMION this is obtained by iteratively assigning each non-electrode point the average value of its neighbor points. The number of iterations required are reduced by an over-relaxation, where the numerical value change in each step is dynamically adjusted by a small value from the pure average of neighboring points.

When more electrodes are present, SIMION uses the additive solution properties of the Laplace equation to solve for each electrode alone by turn. Afterwards it is then possible to scale the solution for each electrode individually and thereby adjust the applied voltage without having to calculate a new Laplace solution for the entire electrode configuration.

Ion trajectories are calculated by computing the curvature from the electric, magnetic and charge repulsive forces at each time step and then calculate the position and velocity at the next time step in a Runge-Kutta approach [27, p. 907-910], where the value after one step is calculated using field potentials from several intermediate positions. To minimize the number of steps and at the same time maximize the accuracy of the calculation the size of the time step is furthermore dynamically adjusted for each step.

6.2 Fragmentation reactions in SIMION

Fragmentation reactions can be implemented in SIMION via user supplied programs. In SIMION a user program must be divided into predefined sections that are called at specific steps during the calculation of a particles trajectory. This gives the option of triggering at certain points, times, events etc. and there by invoke the desired physics at the right moment.

A two body breakup can be simulated by always flying an even number of particles, pairing them two and two. Two subsequent particles to constitute a two body breakup must start from the exact same position with the same mass and initial velocity to obtain the same trajectory until fragmentation. The initial conditions will be chosen as the first particle is launched and be applied to both.

To simulate a real ion beam some randomization can be invoked to make a collection of particle pairs start from a given volume with positions and velocities following a desired distribution, like a uniform or a Gaussian

distribution. The distribution of pairs must resemble the width and divergence of the ion beam to simulate and the zone of interaction must constitute a volume defined by the cross-section of the photon and ion beams.

When the first particle enters the interaction zone, the fragmentation calculations will take place. If any energy is released in the process the fragmentation must obey both energy and momentum conservation. This is calculated in one dimension as described in section 2.4.

To match a desired angular distribution (equation (2.31)), described by the asymmetry parameter (β), the axis of reaction can be rotated by the polar (θ) and the azimuthal (ϕ) angle relative to the photon polarization. The angular distribution is independent of the azimuthal angle ϕ , which can therefore be chosen freely. To obtain random θ -angles following the desired angular distribution the expression for the distribution (equation (2.31)) is integrated over the interval $\theta = [0; \pi]$ and normalized to unity.

$$F(\theta) = \frac{1}{2} \left(-1 - \frac{\beta}{2} (\cos^2(\theta) - 1) \right) \cos(\theta) + \frac{1}{2} \quad (6.2)$$

Pseudo random numbers between zero and one are then chosen and for each random value the corresponding angle is found. However, the integrated expression is unsolvable with respect to the angle (θ) and hence the angle is obtained as a binary search. The angle (θ) is initially set to $\theta = \pi/2$. If the integrated function value ($F(\theta)$) is greater then the random number, the angle is decreased by $\pi/4$, and wise versa if $F(\theta)$ is smaller than the random number. For each step the step size is reduced by a factor of 2. The angle is accepted when the random number and the integrated function value differs by less than 10^{-3} ($|F(\theta) - R| < 10^{-3}$).

Figure 6.1 illustrates the conversion from uniformly distributed random numbers to random angles following a ($\beta = 2$)-distribution. The magenta dots mark 400 pairs of random numbers and angles, to further illustrate the process.

To execute the fragmentation when the first fragment reaches the interaction zone, the mass and charge of the particle can be adjusted to match the first fragment before applying the velocity correction from released energy. Similarly, the mass and charge of the second fragment can be adjusted when that fragment reach the chosen point.

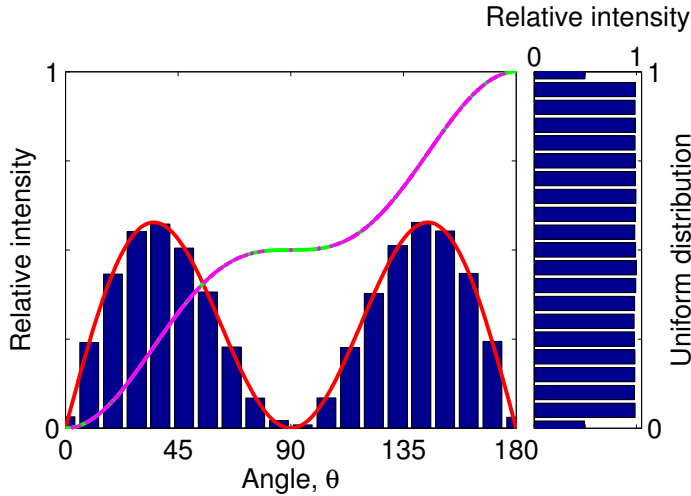


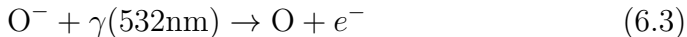
Figure 6.1: *The conversion from uniformly distributed number (vertical histogram) to random angles following a $(\beta = 2)$ -distribution (horizontal histogram). A $(\beta = 2)$ -distribution is marked with the red curve and integral distribution with the green curve. 400 pairs of random numbers and matching angles are marked with magenta dots on the green curve to further illustrate the conversion.*

By generalizing the two body break up it is, of course, possible to implement three or more bodies breakup, however, in these situations the momentum and energy distribution between the fragments are not implicitly given and some further information about the specific process are required besides the conservation laws.

6.3 4π electrons to one detector

For a short period one of the electron detector (eDET2) at TIFF was not operating properly and a voltage configuration of the electron spectrometer was derived to guide all photoemitted electrons to the same detector (eDET1), regardless of the initial emitted direction and without changing the electric field in the interaction region. To confirm the feasibility of this approach a study of the photodetachment from the oxygen anion with

532nm photons was carried out. The photodetachment process can be written as:



With only one nuclei, the energy variation is small as there can be no vibrational or rotational broadening and the energy of emitted electrons will be well defined.

The energy levels of neutral atomic oxygen (O^0) relative to the energy level of the oxygen anion ground state ($\text{O}^- \text{ } ^2\text{P}$) are illustrated in Figure 7.1. At $\lambda = 532\text{nm}$ ($E_\lambda = 2.33\text{eV}$) only the ^3P state in atomic oxygen are accessible $E_f = 1.46\text{eV}$ above the ground state (^2P) of the oxygen anion ($E_i = 0\text{eV}$). Therefore the kinetic energy of the electrons will be

$$E_{\text{KER}}(e^-) = E_i + E_\lambda - E_f \quad (2.22)$$

$$= 0.87\text{eV}. \quad (6.4)$$

At the TIFF setup the neutral oxygen will hit DET2 and all electrons will be guided to eDET1. An overview of the detectors at TIFF are given in Figure 3.6.

To setup the electron guiding the potential of all 22 electrodes in the interaction region and electron spectrometer has to be chosen. One option would be to just have a strong electric field extracting all the light electrons upwards. However, this will also steer the ion.

Another option is to operate the interaction region symmetrically in the vertical direction and use the lower electron spectrometer to deflect the electrons. The employed saddle point potential is depicted in Figure 6.2(b). In this way much lower potentials are necessary and the ions will be only slightly affected as they pass the potentials. Furthermore, all electrons will reach the same detector but be separated in time, as the electrons, initially moving downwards, will have a longer path to transverse. The different pathways give the possibility of differentiating between upwards and downwards emitted electrons, while still collecting all electrons on the same detector. It is even possible to detect an upwards and a downwards emitted electron from the same ion or molecule, without regard of the dead time of the detector.

Treating the detachment as a fragmentation reaction, the SIMION user program described in the previous section (section 6.2) can be used to

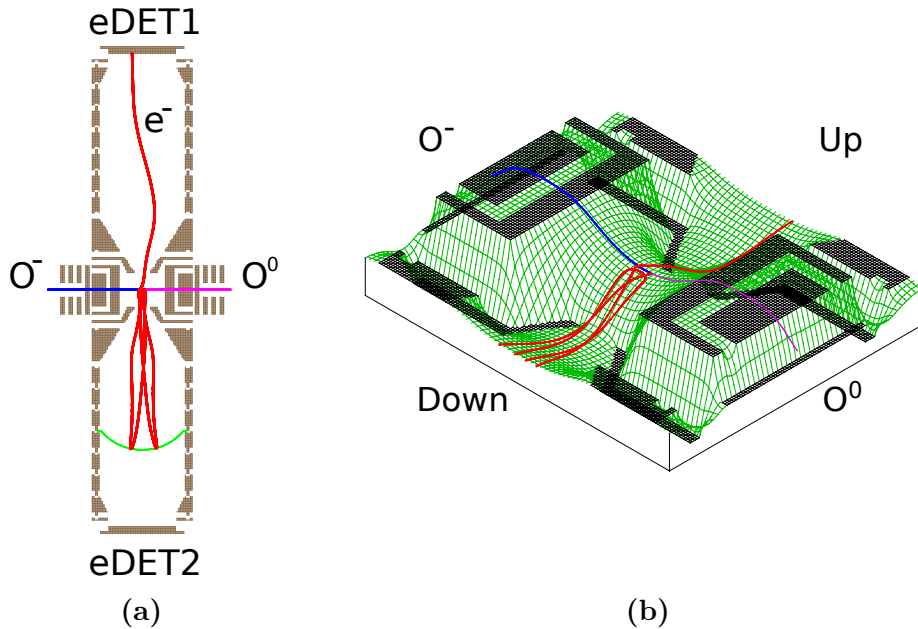


Figure 6.2: Simulation of the photodetachment from the oxygen anion at $\lambda = 532\text{nm}$. The lower part of the spectrometer has been set to reflect electrons. (a) The oxygen anion (blue curve) enters from the left and the neutral oxygen (magenta curve) exits on the right. The trajectory of a downwards emitted electron reflected backup after the second revolution (red curve). $TOF = 310\text{ns}$. The green curve indicates a -28V potential surface, where the electron turns. (b) A potential energy view of saddle point potential in the interaction region with the voltages applied to extract electrons. Notice the negative polarity to better visualize the motion of the negatively charged electron.

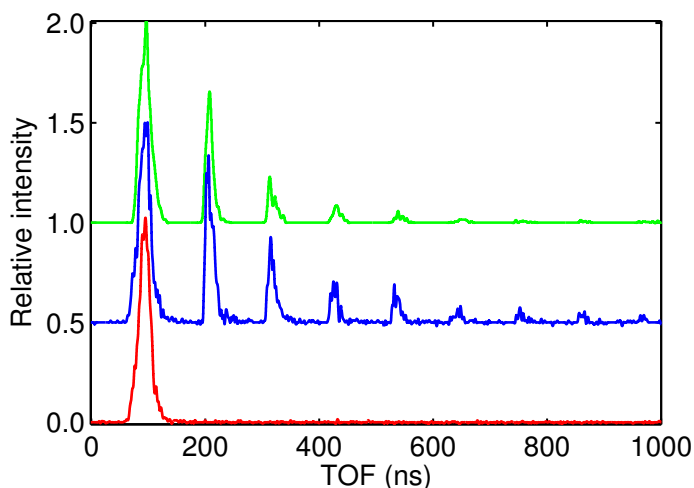


Figure 6.3: TOF distribution of photodetached electrons from the oxygen anion after exposure of 532nm photons using the TIFF electron spectrometer. Three situations are illustrated. Simulated values (green curve). Experimental values with the lower part of the spectrometer in a reflective (blue curve) or grounded (red curve) setting. It is clearly seen, that the reflection actually works and that there are a specific revolution time in the lower part of the spectrometer. Furthermore, there seems to be a fine correlation between the experiment and simulation. The signal height has been scaled relative to the number of electrons going straight to the detector (eDET1) and the blue and green curve has been offset by 0.5 and 1, respectively.

propagate the oxygen anion to the point of reaction, split it to a neutral atomic oxygen and an electron, one particle at a time, and propagate each of these to the designated detector. A simulated trajectories for single detachment process are plotted in Figure 6.2(a) and (b). By systematically optimizing the potential of the lower spectrometer it was confirmed, that it was indeed possible to guide downwards emitted electrons to eDET1 with a total transmission above 90%. The transmission of electrons emitted upwards is close to 100%, while almost 80% of the downwards emitted electrons actually reach eDET1.

To experimentally verify the settings found with SIMION, a 3keV beam

of oxygen anions were guided to the interaction region and trapped for 1ms before the laser was fired. This ensured a more reliable alignment with the spectrometer, as the ion trap and spectrometer are directly attached to the interaction region. Measurements were carried out both with the exact settings, as found with SIMION, and with a setting where the lower part of the lower spectrometer was kept at ground potential, allowing all electrons emitted downwards to escape. The detected TOF distribution from the SIMION simulation and both experiments are depicted in Figure 6.3. In all three situations the intensity has been normalized to the value of directly transmitted electrons. The experimental values have been adjusted by 18ns to earlier times to match the simulation, which can easily be explained by various delays in cables and electronics. It is worth noting that the simulation can represent the time distribution in each peak as well as the peak distance.

Though it does work to reflect electrons in this way and it is possible to have a simulated transmission of electrons above 90%, it is was not possible to reflect all electrons after just one round trip in the lower spectrometer. Rather, some electrons take several revolutions with a specific time per revolution, a pattern that would have been hard to interpret without the simulations.

6.4 DET3: KER and angular distribution

The kinetic energy released (KER) in a fragmentation reaction and the angular distribution of the fragments are two key parameters to retrieve from an experiment. As describes in section 2.5 this is rather straight forward for all detectors at TIFF where the particles are unaffected by electric fields and the trajectories from the point of reaction to the detector are straight lines. For DET3 however, the trajectory of charged, heavy fragments are bend in the electrostatic mirror. This deflection inevitably alters the momentum of the particles and mixes the forward and upward motion. This makes it more complicated to determine the KER and initial angles of emission.

An analytical model have been set up to calculate the KER and emission angle as a function of the TOF and impact position on DET3. The

trajectories have been treated as field free until the particles enter the non-uniform potential of the electrostatic mirror. In the mirror an acceleration is applied to bend the particles toward DET3. The focusing effect in the mirror is introduced as a constant acceleration in three dimensions.

To calibrate the accelerations in the electrostatic mirror to actual potentials applied, a series of simulations was carried out in SIMION. These simulations provided correlated initial velocities and final TOFs and impact positions on DET3. The relation between the KER and emission angle as a function of TOF and impact position proved too complicated to describe with this simplified model.

Even though the model was incapable of describing the relation between the initial and final values there appeared to be a unique mapping approximating each impact position and TOF to an initial velocity vector. From these velocity vectors the released kinetic energy and angle of emission can be calculated. With this approach the KER and angle of emission could be obtained provided a sufficient number of correlated initial and final values are known for each possible KER and emission angle. Hence an approach could be to compare measured TOF and impact positions to a large database.

To generate a database several simulation must be carried out for the specific fragment masses and potentials applied to the electrostatic mirror. The simulations have been executed utilizing the fragmentation reaction user program for SIMION described in section 6.2, but could as well have been made for each fragment separately. The photofragmentation of the protonated water dimer (H_5O_2^+) to the binary channel (H_3O^+ and H_2O^+) have been used as a case study. As experimental input for the SIMION simulation the ion beam energy have been set to 4.2kV and the KER in the process have been varied from $E_{\text{KER}} = 0.1\text{-}10\text{eV}$. The KER is shared between the two fragments as described in section 2.4. H_3O^+ receives $E_{\text{KER}}(\text{H}_3\text{O}^+) = 18/37 = 48.6\%$ while H_2O^+ receives $E_{\text{KER}}(\text{H}_2\text{O}^+) = 51.4\%$. The asymmetry parameter β (See equation (2.31)) have been set to $\beta = 0$ to have all possible emission angles covered with the same statistical weight. The diameter of ion beam have been set to $d_\gamma = d_{\text{ion}} = 1.0\text{nm}$, while length of photon-ion overlap have been set to zero. Within a good approximation this gives a negligible interaction zone and eliminates any fluctuation caused by the uncertainty of the point of reaction. The polarization of the

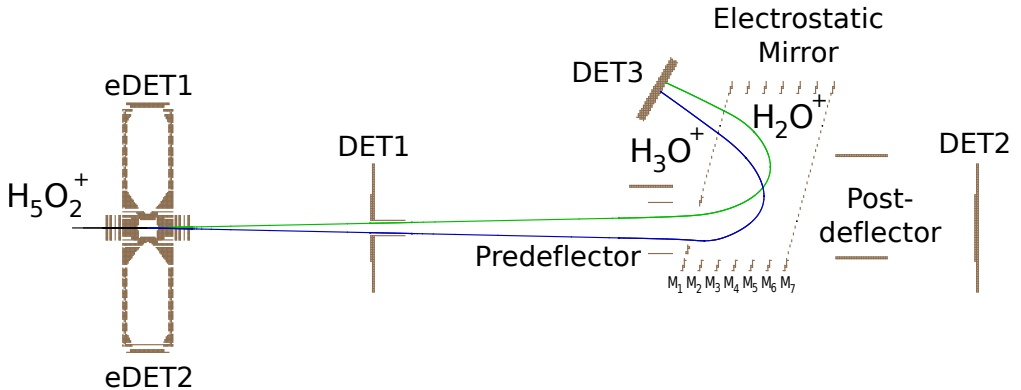


Figure 6.4: The simulated trajectories from a single photofragmentation of ${}^5\text{O}_2^+$ to the binary channel H_3O^+ and H_2O^+ with a KER of $E_{\text{KER}} = 2.5\text{eV}$. The interaction region and pre-deflectors are kept grounded, while the voltages applied to the mirror electrodes are: $M_1 = 0\text{V}$, $M_2 = M_3 = 2.3\text{kV}$, $M_4 = 1.0\text{kV}$, $M_5 = 1.7\text{kV}$, $M_6 = 2.4\text{kV}$, $M_7 = 2.6\text{kV}$. The up and down post-deflector electrodes are set to -3.4 and 3.4kV , respectively, to deflect the positively charged parent beam away from DET2.

photons is set to be parallel to the direction of the ion beam. The simulated trajectories from a single fragmentation are illustrated in Figure 6.4.

With a KER of $E_{\text{KER}} \approx 3\text{eV}$ or higher the fragments can obtain sufficient velocity perpendicular to the forward motion to impact on DET1 or the tube through it. This will introduce a geometrical loss of the fragments. The higher the KER gets the larger a part of the fragments are lost on this account. The losses have not been compensated by simulating more ion trajectories at the higher energies, as this will shift the statistical weight in the angular distribution for the fragments that do reach the detector.

The database have been interpolated using the “TriScatteredInterp” function in MATLAB R2012a. The TriScatteredInterp function interpolates a surface (S) spanned by one to three coordinates (X). Each surface point must have a corresponding set of coordinates. If duplicate coordinate sets are found the matching surface values will be averaged. The TriScatteredInterp function returns an interpolated function (F) that for a given set of coordinates within the interpolated region return a surface value,

$$S = F(X).$$

The KER and the angle of emission, calculated from the simulated initial velocity, will each form a surface to be interpolated and the TOF and impact position correlated to each surface value will be the coordinates. In a similar manner any initial value can be obtained as a function of the final TOF and impact position. However, the surface must be single-valued and to obtain for instance the initial momentum in the x, y and z direction three interpolated function must be made, one for direction.

To obtain the most accurate interpolation the number of entries in the database for each energy must be high. In order to judge when the precision as a function of the number of entry point converges three databases have been made with 10^3 , 10^4 and 10^5 points, respectively, for each of the energies $E_{\text{KER}} = [0.1, 0.3, 0.5, 1, 2, 3, \dots, 10]$ eV. 14 energy steps in total. Similarly a fourth database have been made with 10^4 datapoint at each of the 60 energies $E_{\text{KER}} = [0.1, 0.2, 0.3, \dots, 0.6, 0.8, 1.0, 1.2, \dots 11.4]$ eV to judge the need energy resolution. To summarize and simplify the following examination of the databases they will be named:

A: 10^3 points, $\beta = 0$, $E_{\text{KER}} = [0.1, 0.3, 0.5, 1, 2, 3, \dots, 10]$ eV

B: 10^4 points, $\beta = 0$, $E_{\text{KER}} = [0.1, 0.3, 0.5, 1, 2, 3, \dots, 10]$ eV

C: 10^5 points, $\beta = 0$, $E_{\text{KER}} = [0.1, 0.3, 0.5, 1, 2, 3, \dots, 10]$ eV

D: 10^4 points, $\beta = 0$, $E_{\text{KER}} = [0.1, 0.2, 0.3, \dots, 0.6, 0.8, 1.0, 1.2, \dots 11.4]$ eV

A database with 10^5 entry points at each energy and a resolution of 0.2eV would required a substantial amount of physical computer memory and significantly increase processing times.

As the user program are invoked two entry point are used for each simulated fragmentation, one point for H_3O^+ fragment and the subsequent point for H_2O^+ .

6.4.1 Negligible extent of the interaction region

To test the interpolated function, an separate simulation have been executed with the same settings as used in the databases. The KER in the test

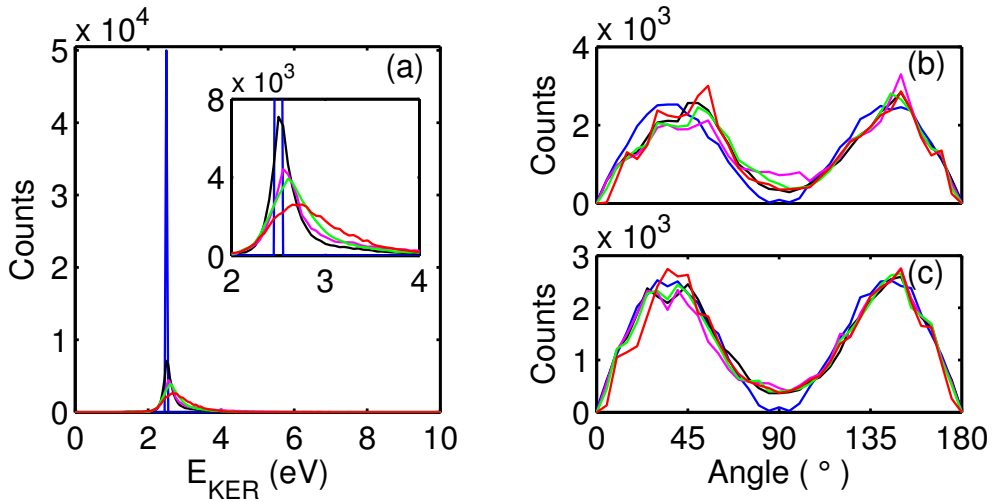


Figure 6.5: The observed KER in and angular distribution after a fragmentation of $H_5O_2^{2+}$ to H_3O^+ and H_2O^+ obtained in a simulation with a KER of $E_{KER} = 2.5\text{eV}$, an asymmetry parameter $\beta = 2$ and a negligible interaction zone. The blue curve is the direct output from the simulation, while the red, green, magenta and black corresponds to the response from database A, B, C and D, respectively. (a) The KER. (b) and (c) The angular distribution for fragments H_2O^+ and H_3O^+ , respectively

simulation have been set to $E_{KER} = 2.5\text{eV}$, which is deliberately placed between the grid points for all the databases. The asymmetry parameter have been set to $\beta = 2$. With the polarization of the photons parallel to the direction of the ion beam, the fragments will primarily be ejected in the forward and backward direction. This gives a characteristic angular distribution.

The results from the simulation are depicted in Figure 6.5. The blue curve show the direct values form the simulation. The red, green and magenta curves depict the response from the interpolated function for the databases A, B and C, respectively, while the black curve corresponds to database D. Plot (a) shows the kinetic energy calculated from the initial velocities, while plot (b) and (c) illustrates the angular distribution for

Table 6.1: Quantification of how well the interpolated values from the databases recreates the direct output from a simulation of the fragmentation of $H_5O_2^{2+}$ to H_3O^+ and H_2O^+ with a KER of $E_{KER} = 2.5\text{eV}$, an asymmetry parameter $\beta = 2$ and a very small interaction zone. The actual distribution are shown in Figure 6.5.

Database	E_{KER}	$\beta(H_2O^+)$	$\beta(H_3O^+)$
A	2.8 ± 0.4	1.7 ± 0.2	1.8 ± 0.14
B	2.6 ± 0.2	1.6 ± 0.18	1.8 ± 0.10
C	2.6 ± 0.17	1.5 ± 0.2	1.8 ± 0.12
D	2.5 ± 0.12	1.7 ± 0.17	1.8 ± 0.09

fragments H_2O^+ and H_3O^+ , respectively.

The sharp blue peak in (a) demonstrates the small interaction zone and well defined KER. The response from database A clearly gives the poorest match to the KER, while the database C gives a slightly better result than database B. However, the difference between B and C are not as distinct as between A and B. Even the 10^4 entry points in database B gives a decent estimate of the KER. Database D gives the best results for the KER and suggest a better energy resolution with 10^4 entries at each energy is advantageous to 10^5 entry points at fewer energies. Furthermore, the total number of entries in database D constitute only 40% of the entry points in database C and thereby reduces the strain on the computer memory.

For the angular distribution in (b) and (c), the picture is not as clear. The responds from each database do reproduce the general shape of an angular distribution with an asymmetry parameter of $\beta = 2$, at least the shape clearly neither resembles a $\beta = -1$ nor $\beta = 0$ distribution. The angular distribution and the asymmetry parameter are introduced in section 2.4.

To quantify the precision of each database a Gaussian distribution have been fitted to each KER distribution and the expression for the angular distribution (equation 2.31) have been fitted to the angular distributions to find the asymmetry parameter β for each fragment. The results are listed in table 6.1. For the KER the listed uncertainty is two times the

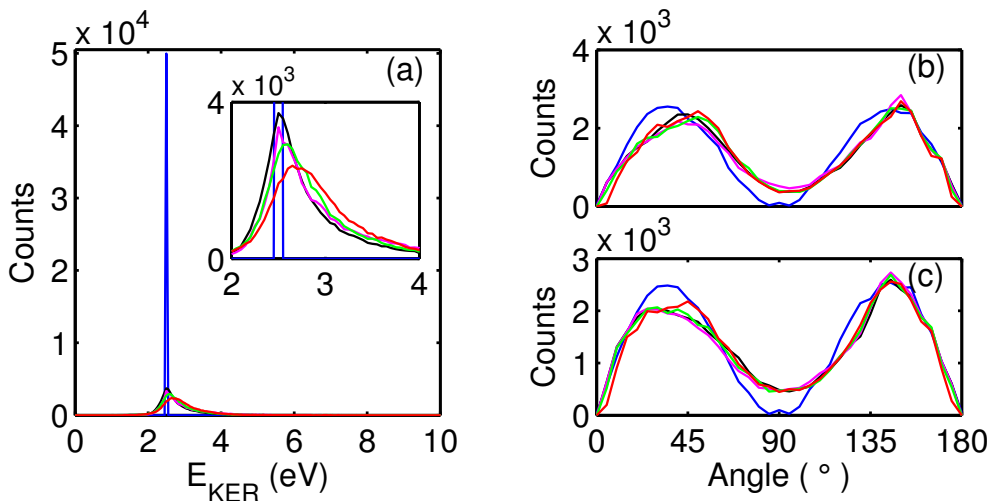


Figure 6.6: The observed KER and angular distribution after a simulated fragmentation of $H_5O_2^+$ to H_3O^+ and H_2O^+ . The interaction zone have been increased to a cylinder with diameter and length of 1mm compared to the simulation presented in Figure 6.5. The blue curve is the direct output from the simulation, while the red, green, magenta and black corresponds to the response from database A, B, C and D, respectively. (a) The KER. (b) and (c) The angular distribution for fragments H_2O^+ and H_3O^+ , respectively

standard deviation (σ), while uncertainty for the asymmetry parameter is the extent of a 0.95 confidence interval.

All the database slightly overestimates the KER and fall just short of $\beta = 2$. The results for the KER from the databases C and D are very close to the mark.

6.4.2 Realistic sized interaction region

As the concept appears to work, a new simulation was carried out with the interaction zone is increased to a realistic size by increasing diameter of the ion beam to $d_{ion} = 1.0\text{mm}$ and the extent of the interaction zone to $L_\gamma 1.0\text{mm}$. This gives a cylinder shaped interaction zone. The outcome of the simulation is shown in Figure 6.6 and the result of fitting the data

Table 6.2: Quantification of the precision of the databases when the simulation includes a realistic interaction zone (a small cylinder with a diameter and length of 1mm). The actual distribution are shown in Figure 6.6 and the values can be compare to table 6.1, where the interaction zone was negligible.

Database	E_{KER}	$\beta(\text{H}_2\text{O}^+)$	$\beta(\text{H}_3\text{O}^+)$
A	2.8 \pm 0.4	1.6 \pm 0.17	1.7 \pm 0.11
B	2.7 \pm 0.3	1.6 \pm 0.16	1.7 \pm 0.13
C	2.6 \pm 0.3	1.6 \pm 0.15	1.8 \pm 0.15
D	2.6 \pm 0.2	1.7 \pm 0.15	1.7 \pm 0.14

to a gaussian distribution and the relation for the angular distribution, respectfully, are listed in table 6.2. The scale of the insert in plot (a) have been reduces but otherwise Figure 6.5 and Figure 6.6 are directly comparable to see the effect of a non-negligible interaction zone.

For the realistically sized interaction zone the KER distributions are wider. Especially for the databases C and D where the width have doubled compared to simulation with the negligible interaction zone. The angular distribution appears to be shifted slightly towards too high angles for the realistic sized interaction zone, but the shape of the distributions are still identifiable as a $\beta > 2$ distribution.

For a realistically sized interaction zone the presented method clearly determines the order of magnitude of the KER and the shape of the angular distribution for particles detected in DET3.

6.4.3 Realistic sized interaction region and Gaussianly distributed KER

The delta function distribution of the KER have so far been used to test the feasibility of the method and judge the effect of the size of the interaction region. To test the effect of the KER distribution a simulation have been carried out with a KER following a Gaussian distribution with center $E_{\text{KER}} = 2.5\text{eV}$ and standard deviation $\sigma = 0.25\text{eV}$. The results a shown in

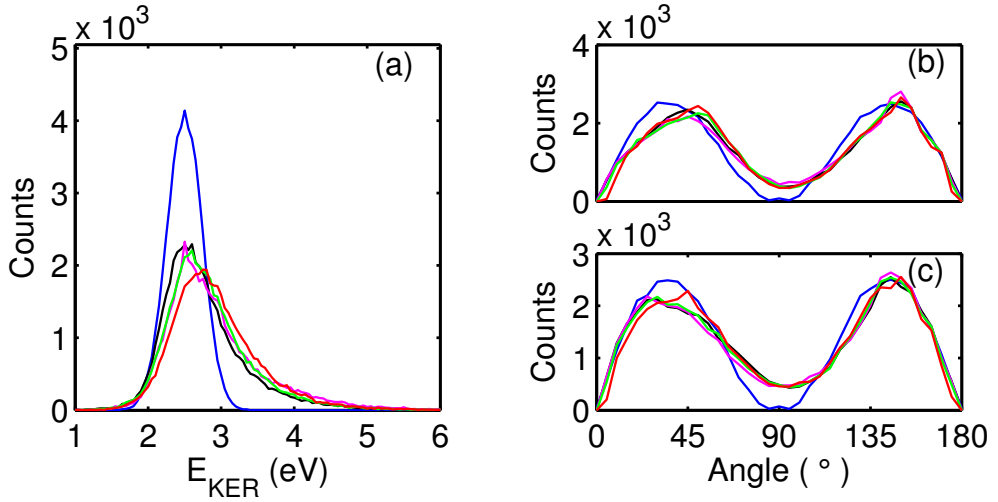


Figure 6.7: The observed KER and angular distribution after a simulated fragmentation of $H_5O_2^{2+}$ to H_3O^+ and H_2O^+ . The KER have been set to follow a Gaussian distribution with center $E_{KER} = 2.5\text{eV}$ and standard deviation $\sigma = 0.25\text{eV}$. The blue curve is the direct output from the simulation, while the red, green, magenta and black corresponds to the response from database A, B, C and D, respectively. (a) The KER. (b) and (c) The angular distribution for fragments H_2O^+ and H_3O^+ , respectively

Figure 6.7. The blue curve is the direct output from the simulation and fitting it with a Gaussian distribution returns a KER of $E_{KER} = 2.5 \pm 0.5\text{eV}$, just as expected. Notice that the uncertainty is listed as 2σ as in the rest of this section.

Even when the KER distribution have been broadened to a Gaussian distribution with standard deviation $\sigma = 0.25\text{eV}$ in the simulation, the width of the responds from database D only increases from $E_{KER} = 2.6 \pm 0.5\text{eV}$ with the Delta function KER to $E_{KER} = 2.6 \pm 0.4\text{eV}$ with the Gaussian distribution KER. This suggest the database responds scales smoothly with the width of a measured distribution and only exhibits an offset of $\sim 0.5\text{eV}$.

Of course, each database is specific for one mass over charge value for

Table 6.3: Quantification of the precision of the databases when the simulation includes a realistic interaction zone (a small cylinder with a diameter and length of 1mm) and Gaussianly distributed KER. $E_{KER} = 2.5\text{eV}$ and $\sigma = 0.25\text{eV}$. The actual distribution are shown in Figure 6.7 and the values can be compare to table 6.2, where the KER distribution is a delta function.

Database	E_{KER}	$\beta(\text{H}_2\text{O}^+)$	$\beta(\text{H}_3\text{O}^+)$
A	2.8 ±0.5	1.6 ±0.17	1.7 ±0.10
B	2.7 ±0.4	1.6 ±0.16	1.7 ±0.12
C	2.7 ±0.4	1.6 ±0.15	1.8 ±0.13
D	2.6 ±0.4	1.7 ±0.14	1.7 ±0.13

the fragments and the specific settings of the electrostatic mirror.

6.4.4 Higher KER range

So far the KER of the test simulation have been fixed at $E_{KER} = 2.5\text{eV}$ to be under the limit where noticeable geometrical losses are observed. To demonstrate the usefulness of the method at higher KERs a test simulation have been carried out at $E_{KER} = 7.5\text{eV}$ and an asymmetry parameter of $\beta = 2$. The realistically sized interaction region (a small cylinder with a diameter and length of 1mm) and the delta function KER distribution have been used.

At this KER the transmission to DET3 is 55% for the H_3O^+ fragments and 50% for the H_2O^+ fragments. In the simulation 0.17% of H_3O^+ fragments and 0.77% of the H_2O^+ fragments impacts on DET1. The fragments not accounted for on either detector are lost in the grounded tube just behind DET1.

The KER and angular distributions obtained on DET3 using the databases are shown in Figure 6.8 and the parameters for a Gaussian fit are given in table 6.4. All databases produces a distribution in the high range of the KER scale in the databases, however the width of the KER distribution returned from each database are twice the width found at $E_{KER} = 2.5\text{eV}$

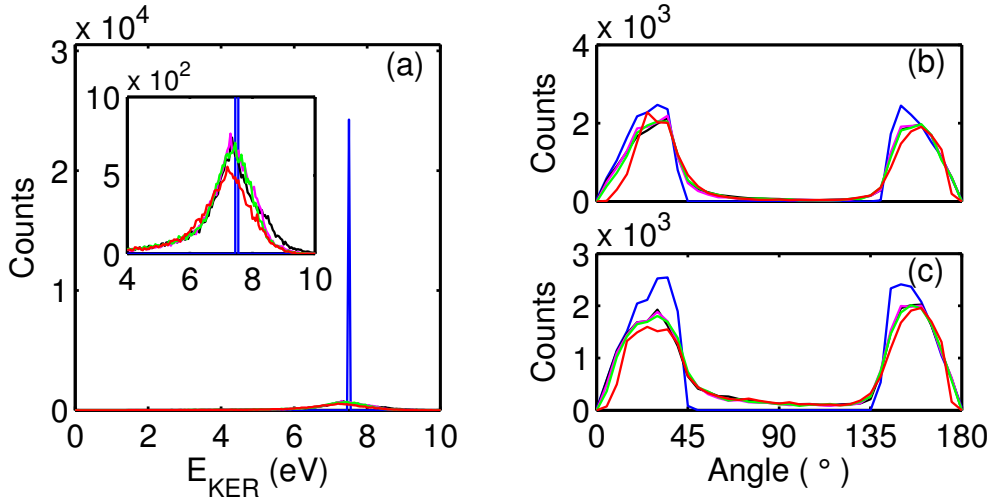


Figure 6.8: The observed KER and angular distribution after a simulated fragmentation of $H_5O_2^{2+}$ to H_3O^+ and H_2O^+ . The KER have been set to $E_{KER} = 7.5$ eV. The interaction zone was cylinder with diameter and length of 1mm. The blue curve is the direct output from the simulation, while the red, green, magenta and black corresponds to the response from database A, B, C and D, respectively. (a) The KER. (b) and (c) The angular distribution for fragments H_2O^+ and H_3O^+ , respectively

with the same settings. This suggest that the transmission losses due to DET1 should be compensated by more simulated entries in the database when working in this range.

The angular distributions clearly illustrates that fragments with a large velocity perpendicular to the beam direction are lost. No fragments in the angular interval $\theta = [45 : 135]$ reached DET3. A few impacts are wrongly assign to this interval by the databases, however, and properly corresponds the tail towards lower values seen in the KER distribution. Even with the miss assigned impact, the angular distribution deviate from an expected angular distribution (equation 2.31) and clearly shows that a lot of intensity is lost.

The transmission losses through DET1 is a characteristic of the setup

Table 6.4: Quantification of the precision of the databases with $E_{KER} = 7.5\text{eV}$, $\beta = 2$ and a realistically sized interaction zone (a small cylinder with a diameter and length of 1mm). The actual distribution are shown in Figure 6.7 and the values can be compare to table 6.2, where the KER is $E_{KER} = 2.5\text{eV}$.

Database	E_{KER}
A	7.2 \pm 0.7
B	7.4 \pm 0.6
C	7.4 \pm 0.6
D	7.4 \pm 0.6

and not easily amended. For the high energy range the loses should be compensated by simulating more ions to increase the precision.

XUV detachment from O^-

In this section an experimental study of the photodetachment from the oxygen anion at $\lambda_\gamma = 41.7\text{nm}$ using the TUFF end station of the FLASH will be described. The main focus is on the ratio of the single to double electron detachment process.

Absolute detachment cross sections have previously been measured with high precision using synchrotron radiation sources for channels with charged fragments, Na^- [28], F^- [29] and Cl^- [30]. These studies have been unable to detect the neutral channel, due to the parallel beam geometry. At low photon energy (400-2000nm) it is possible to detect both neutral and charged fragments in a parallel beam setup e.g. by electrostatically deflecting the charged fragment to one detector and letting the neutrals impact on a coated glass plate placed in the path of both photons and neutrals. The neutrals will kick electrons free, which can be accelerated to a nearby detector placed outside the photon path [31]. However, below 250nm a glass plate is no longer transparent and will block the photons, rendering this approach unfeasible.

In many of the previous experiments on the photodetachment from the oxygen anion the photon energy has been below or only slightly above the first excited state in O^0 . In the present study the photon energy is even higher than required to reach the second excited state of O^+ (2P). Furthermore, the neutral and positive ion can be chosen to be detected either on the same detector or on two different detectors. When both species

impact on the same detector, the trajectories and detection efficiencies will be almost identical and comparing the intensity of the O^0 and the O^+ channels will be more straightforward forward.

Lastly, the possibility of detecting pairs of ions and photoelectrons in coincidence is demonstrated.

The results presented here are published in [32].

7.1 The oxygen anion

Oxygen is the most abundant element in the Earth crust (46%) and the second most abundant in the atmosphere (21%) [33]. As such, oxygen affects almost any branch of chemistry and physics. The oxygen anion is stable and numerous aspects of the photodetachment from the oxygen anion have previously been studied in both the infrared and ultraviolet range. The photodetachment cross section has been investigated on an absolute scale [34–36] and as a function of photon energy [34, 37, 38]. The atomic oxygen/oxygen anion system has been used as a model system for very precise measurements of the electron affinity [37, 39, 40] and fine structure splitting of electronic states [37, 38, 41].

The oxygen anion (O^-) is an open shell system with the electronic ground state electronic configuration $1s^2 2s^2 p^5 \ ^2P$. The two fine structure levels $J = \frac{1}{2}, \frac{3}{2}$ have an energy difference of 0.022eV [37]. With 5 p-electrons the oxygen anion has one open p-shell, making the oxygen anion an interesting and important system for modeling e.g. correlated electron motion.

The ionization energy of the oxygen anion is equal the electron affinity of neutral oxygen $E_{EA}(O) = 1.461122 \pm 0.000003 \text{eV}$ ($O^- (^2P) \rightarrow O^0 (^3P)$) [37]. By removing one of the p-electrons from the oxygen anion the neutral oxygen can end up in one of three different electronic configurations (3P , 1D and 1S). The ionization energy of neutral oxygen is $E_{IE}(O) = 13.618$ [42] and fine structure splitting of the $O^0 (^3P)$ has been measured to 0.020eV [41].

The minimum energy required for a double ionization is $E_{EA}(O) + E_{IE}(O) = 15.08 \text{eV}$ ($O^- (^2P) \rightarrow O^+ (^4S)$).

In Figure 7.1 the single and double photodetachment from O^- is illustrated including the lower energy levels of O^0 and O^+ reachable from the

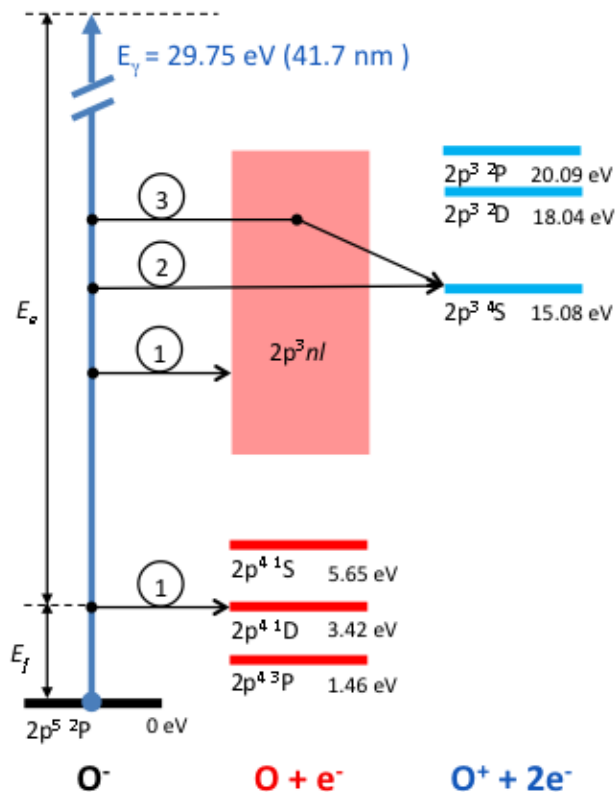


Figure 7.1: Illustration of the single and double photodetachment from O^- to O^0 and O^+ respectively. The energy levels accessible by $\lambda = 41.7$ nm photoabsorption are included. Processes labeled by 1 show single detachments while processes labeled 2 and 3 show direct (simultaneous) and indirect (sequential) double photodetachment, respectively.

ground state of O^- with a $\lambda = 41.7$ nm photon ($E_\gamma = 29.75$ eV).

The process marked with 1 is a single photodetachment from O^- resulting in the O^0 atom and an photoelectron with the kinetic energy

$$E_{\text{KER}}(e^-) = E_i + E_\gamma - E_f \quad (2.22)$$

where E_i is the energy of the initial O^- state and E_f is the energy of the final O^0 state.

The process marked by 2 is a double photodetachment, where both electrons are simultaneously kicked out, while the process marked 3 is a sequential process with an intermediate state of exited O^0 before the final ionization to achieve the positive charge.

7.2 The experiment

The experiment was performed at TUFF. The experimental setup is described in chapter 3.

The hollow cathode ion source was operated at negative potential with a gas inlet of pure water vapor at approximately 0.1mbar and sustaining a discharge of $U_{\text{disc}} = 775\text{V}$ and $I_{\text{disc}} = 55\text{mA}$. The ion beam energy was $E_I = -3\text{keV}$ and the ion beam current in the interaction region was approximately $I_{O^-} = 1.0\text{nA}$, corresponding to a linear density of $l_{O^-} = 3.3 \cdot 10^2\text{cm}^{-1}$.

The FLASH facility delivered horizontally polarized photons at $\lambda_\gamma = 41.7 \pm 0.5\text{nm}$. The average photon pulse energy was $E_\gamma = 30\mu\text{J}/\text{pulse}$ corresponding to the average number of photons in the order of $\langle N_\gamma \rangle = 10^{12}\text{photons}/\text{pulse}$. The transmission of the PG2 beam line is $T_{\text{PG2}} \sim 0.5 \pm 0.1$ [11], resulting in an effective photon pulse energy of $E_{\gamma, \text{effective}} = E_\gamma \cdot T_{\text{PG2}} = 15\mu\text{J}/\text{pulse}$. The photon pulses arrived as pulse trains with a repetition rate of 10Hz. Each pulse train contains 50 photon bunches separated by $5\mu\text{s}$, and with a duration of $\sim 250\text{fs}$. In total, this amounts to 500 photon-ion crossings per second.

The pressure in the interaction region was $p = 1-3 \cdot 10^{-10}\text{mbar}$ during the measurements.

The profiles and positions of both the photon and ion beam were measured and the results are shown in Figure 7.2. It is seen that both beams are $\sim 1\text{mm}$ wide (FWHM) and the vertical beam centers have an offset of 0.1mm. The overlap factor was found to be $F = 7.3 \pm 0.1\text{cm}^{-1}$ (See equation(2.19)).

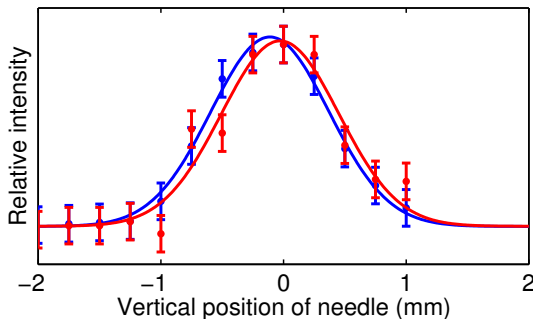


Figure 7.2: *Beam profile of the photon (red) and O^- (blue) beam. Both measured by passing a 1mm metal strip through the beams.*

The detector setup of TIFF is shown in Figure 3.1 and in this study DET2 was used to detect both O^0 and O^+ while the electrostatic mirror was used to bend the main beam of O^- towards DET3. Thereby, the mirror actually also accelerated and focused O^+ onto DET2. The position of the charged O^+ on the detector can be shifted with the post-deflectors after the mirror electrodes, thereby ensuring that the neutral and positively charge ions are separated in both time and position. During this experiment a zero bias was applied to the front of the MCP stack to ensure a more equal efficiency for detecting O^0 and O^+ . To test for a position dependent efficiency of the detector the position of the O^+ was shifted to four different positions, and the intensity of neutral and charged fragments were compared. This was found not to effect the results, as expected.

The measurement comprised recordings from two different photon pulse energies.

In the first measurement the full intensity of photon was used to achieve a high count rate of the detachment processes.

In the second measurement the photon intensity was lowered ($E_\gamma = 30\mu\text{J} \rightarrow E_\gamma = 3\mu\text{J}$) and eDET1 was turned on to count single electron and ion impacts in coincidence. For the ions the high speed of the beam ensured that only beam related ions reached the detector, but as the electrons detached from the residual gas have kinetic energies comparable to the ones of interest, a too high photon pulse energy will generate too many electrons and saturate the electron detector.

7.3 Results

7.3.1 Ratio of single and double detachment

The distribution of time of flight (TOF) of particles detected with detector DET2 are shown in Figure 7.3(a) with the time zero being the time the photons arrived in the interaction zone. The blue curve depicts TOF recorded in the Ions&Photons mode and similarly the red Ions-only, black Photons-only and the green is the Dark mode. The different measuring modes are described in section 4.4. A large ion background is observed (red curve) and properly originates from O^- colliding with the residual gas in the vacuum chamber. By shifting the voltage on the post-deflector after the electrostatic mirror this was confirmed to be positively charged, and therefore corresponding to a double detachment. A huge spike at $5\mu\text{s}$ was observed in both the Ions&Photons and the Photons-only mode. As the bunch spacing in the pulse trains is $5\mu\text{s}$, the spike corresponds to photons scattering in the interaction region in the successive photon-ion crossing and overtakes the ions to arrive at $5\mu\text{s}$. This can even be seen as a confirmation, that the time zero is correctly implemented. The background-subtracted, photon-induced signal is given by

$$\text{Signal} = \text{Photons\&Ions} - \text{Ions only} - \text{Photons only} + \text{Dark} \quad (4.6)$$

In the background-subtracted, photon-induced signal two narrow peaks are found at 4880nm and 5150nm and identified as O^+ and O^0 , respectively.

In Figure 7.3(b) the spatial distribution for the particles detected in narrow time windows, around the O^+ and O^0 , are shown. Two small areas show significant larger intensities, corresponding to the two observed particle species. As the peaks are in the middle of the detector it can safely be assumed that all particles from the photo induced detachment are detected.

Figure 7.3(c) shows the background-subtracted, photon-induced signal in the intermediate spatial area around the two peaks, see the two white squares in Figure 7.3b. This gives an almost background free signal of both O^+ and O^0 .

This, of course, is only the particles detected. The actual number (R_X)

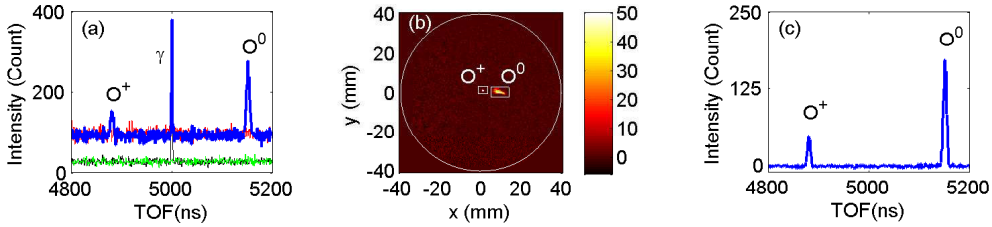


Figure 7.3: Recorded impacts on DET2 after $\sim 1.3 \cdot 10^6$ ion-photon crossings. (a) The TOF distributions corresponds to the operation modes (See section 4.4), Blue: Photons&Ions, Red: Ions only, Black: Photons only and Green: Dark. The peaks from single detachment (O^+) and double detachment (O^0) is marked around 4880ns and 5150ns, respectively, while the very narrow peak at 5000ns corresponds to scattered photon from the following photon-ion crossing. Plot (b) shows the impact position in the time interval corresponding the O^0 and O^+ peaks in plot (a). Plot (c) shows the background-subtracted, photon-induced TOF distribution for the particles recorded in the area marked in (b). It is seen that this almost eliminates the background.

of reactions X for one photon-ion crossing is given by

$$R_X = N_\gamma \cdot l_I \cdot F \cdot \sigma_X \quad (2.20)$$

Hence, the number of detected particles can be estimated by

$$N_X = (\langle N_\gamma \rangle T_{PG2}) (l_{O^-}) F \sigma_X P_\gamma \epsilon_X \quad (7.1)$$

where X can be both the single and double detachment, $\langle N_\gamma \rangle$ is the average number of photons per pulse, T_{PG2} is the transmission of the PG2 beam line $T_{PG2} \sim 0.5 \pm 0.1$ [11], l_{O^-} is the linear density of of the mother beam, P_γ is the number of photon-ion crossings and ϵ_X is the detection efficiency for particles of channel X .

From this a reaction cross section for the single detachment channel can

be estimated, if the detection efficiency is $\epsilon_{O^0} = 0.5 \pm 0.1$.

$$\begin{aligned} \sigma_{O^0} &= \frac{N_{O^0}}{(\langle N_\gamma \rangle T_{PG2}) (l_{O^-} F) P_\gamma \epsilon_{O^0}} \\ &= \frac{986}{(6 \cdot 10^{12} \cdot 0.5) (3.3 \cdot 10^2 \text{cm}^{-1} \cdot 7.3 \text{cm}^{-1}) 1.3 \cdot 10^6 \cdot 0.5} \\ &= 2.1 \pm 0.6 \cdot 10^{-19} \text{cm}^2 \end{aligned} \quad (7.2)$$

The ratio of the single to double detachment channels are then seen to be given directly, as the number of counts in the two peaks shown in Figure 7.3c, assuming the same detection efficiency for both channels ($\epsilon_{O^0} = \epsilon_{O^+} = 0.5 \pm 0.1$). This measurement gave

$$\frac{\sigma_{O^0}}{\sigma_{O^+}} = \frac{N_{O^0}}{N_{O^+}} = 3.99 \pm 0.26. \quad (7.3)$$

As mentioned, a test for a position dependent detection efficiency was carried out by moving the O^+ beam on the detector, using the post-deflector and the results for different separations of O^0 and O^+ on DET2 is shown in Figure 7.4. The average of the three different separations are:

$$\frac{\sigma_{O^0}}{\sigma_{O^+}} = 4.12 \pm 0.17. \quad (7.4)$$

7.3.2 Photoelectrons from single detachment

At FEL intensity used for ion analysis the total number of electrons detached completely saturates the detectors, and counting single electrons is not possible. Hence, the electron spectroscopy was performed at much reduced photon pulse energy ($E_\gamma = 30 \mu\text{J} \rightarrow E_\gamma = 3 \mu\text{J}$). Even at this reduced intensity some photon might impact on the detector. Hence the electron spectrometer was activated to retard the electrons to arrive sufficiently later than scattered photons. Another problem is to distinguish electrons from the desired reaction from the large number of electrons, originating from other sources for instance ionization of the residual gas and electrons kicked off the walls by stray photons. This creates a large background on which the electrons of interest must be found.

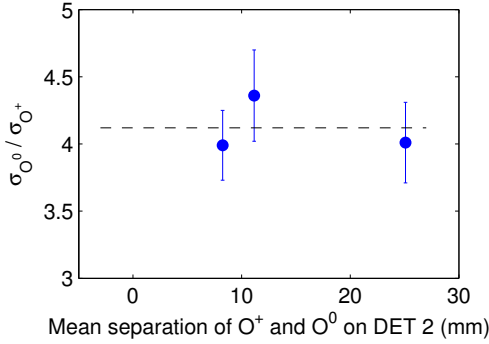


Figure 7.4: The measured ratio between single and double detachment as a function of separation of the beam spots on DET2. To test possible variations of detection efficiency for different areas of DET2. No significant variation was found.

The number of photodetached fragments of interest, produced in a single photon-ion crossing ($P_\gamma = 1$), is given by equation (7.1) and for now the detection efficiency is set to $\epsilon_x = 1$

$$\begin{aligned}
 N_{O^0} &= \langle N_\gamma \rangle \cdot T_{PG2} \cdot l_{O^-} \cdot F \cdot \sigma_X & (7.5) \\
 &\approx 6 \cdot 10^{12} \cdot 0.5 \cdot 3.3 \cdot 10^2 \text{cm}^{-1} \cdot 7.3 \text{cm}^{-1} \cdot 2.1 \cdot 10^{-19} \text{cm}^2 \\
 &= 1.5 \cdot 10^{-3}
 \end{aligned}$$

where the inserted values are estimates for the current experiment with O^0 . The number of fragments produced from collisions with the residual gas is given by

$$\begin{aligned}
 R_X^g &= \sigma_X^g \cdot n_g \cdot \left(\frac{I_{O^-}}{e} \right) \cdot L_X^g \cdot \Delta t_X & (7.6) \\
 &\approx 10^{-15} \text{cm}^2 \cdot 2 \times 10^6 \text{cm}^{-3} \cdot \left(\frac{1 \text{nA}}{1.6 \cdot 10^{-19} \text{C}} \right) \cdot 150 \text{cm} \cdot 30 \text{ns} \\
 &= 5.6 \cdot 10^{-5}
 \end{aligned}$$

where σ_X^g is the cross section for detachment in the residual gas, n_g is the residual gas density, $\frac{I_{O^-}}{e}$ is the rate of ions, L_X^g is the effective propagation

length from which the fragments can reach DET2 and Δt_X is the TOF range when photodetachment fragments from the ion beam are observed on DET2.

Finally, the number of photoelectrons produced by ionization of the residual gas in a single photon-ion crossing is

$$\begin{aligned} R_X^g &= \langle N_\gamma \rangle \cdot T_{\text{PG2}} \cdot n_g \cdot L_e^g \cdot \sigma_e^g & (7.7) \\ &\approx 6 \cdot 10^{12} \cdot 0.5 \cdot 2 \cdot 10^6 \text{ cm}^{-3} \cdot 1 \text{ cm} \cdot 10^{-18} \text{ cm}^2 \\ &= 6 \end{aligned}$$

where σ_e^g is the photoionization cross section and L_e^g is the effective distance from where photoelectrons are extracted to the electron detectors. From the expressions above it is seen that the collisional ionization of the residual gas has a very small contribution, and may be ignored. The photoionization of the residual gas is by far the dominant effect. Much larger even than the number of electrons for the reaction of interest. Lowering the FEL intensity will decrease both contributions by the same factor and result in much extent measurements for the same statistics. Even if the estimated cross section for the photoionization of the residual gas have been set two orders of magnitude too high, the contribution will still be a factor of 4 higher than for the electrons in interest.

Never the less, this is what must be dealt with, and the photon intensity must be low enough that only a countable number of electrons are impacting in the electron detector per photon-ion crossing. The TOF of the electrons from the interaction region to eDET1 are $\leq 200\text{ns}$ and a non-saturated signal can therefore be obtained by reducing the intensity of the FEL until only 2-3 electrons are detected per photon-ion crossing and single electron counting is possible.

To select only the electrons and ions detected in coincidence, a coincidence analysis between electrons and O⁰-particles is invoked as described in chapter 5. The resulting TOF distribution of real (red curve) and random (dashed blue curve) coincidences are plotted in Figure 7.5(a).

A distribution of true coincidence is clearly seen as the difference between 40-50ns corresponding to the electrons from the single detachment from O⁻. To estimate the kinetic energy of the electrons a simulation in SIMION has been carried out with different kinetic energy releases (15.0eV, 24.1eV and

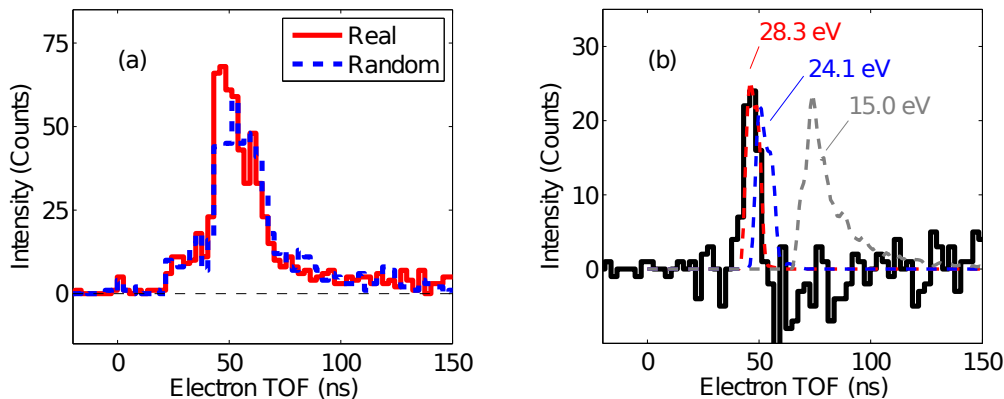


Figure 7.5: Results from a coincidence analysis between electrons on eDET1 and O^0 and DET2. a) shows the direct output. Red: Real correlated coincidence pairs. Blue: Random coincidence pairs. b) the solid black line shows the difference between the real and random coincidence pairs from a). The dashed lines are TOF distributions from a SIMION simulation of electrons with different kinetic energies.

28.3eV) produced by detachment from a 3keV O^- beam with a diameter of 1mm. The resulting TOF distributions from the simulations are plotted as dashed lines in Figure 7.5(b) along with the difference between the real and random signal (black curve), showing that a distribution with a kinetic energy of 28.3eV fits the observed distribution well.

7.4 Discussion

In this study the neutral channel was found to be 4 times larger than the charged channel and hence our setup with crossed beams and fast moving ions seems to compliment the high precision cross section results already obtained for the charged detachment channels by enabling measurements of the relative cross sections of all fragments at once, however, only at one wavelength at a time.

From the simulations and coincidence analysis it was found that pho-

toelectrons with 28.3eV are properly observed. This corresponds to a photodetachment from $O^- \ ^2P$ and into the $O^0 \ ^3P$ state, though the energy resolution does not allow us to exclude ending in the $O^0 \ ^1D$ state. The energy diagram can be seen in Figure 7.1.

Obtaining these results requires many photon-ion crossings as far less than one coincidence pair is found per crossing with the lowered FEL intensity. At one setting $2.7 \cdot 10^6$ FEL shot were recorded with a photon energy of $3.5\mu\text{J}/\text{pulse}$, corresponding to $\langle N_\gamma \rangle \cdot T_{\text{PG2}} = 7.3 \cdot 10^{11}$ photons/pulse. This resulted in $2.5 \cdot 10^3$ real coincidence pairs and $2.4 \cdot 10^3$ random coincidence pairs, hence the number of true coincidences was only in order of 10^2 .

Due to the low yield of the double detachment channel ($\sigma_{O^+}/\sigma_{O^0} \sim 1/4$), it was not possible to make a similar analysis of the photoelectrons from this channel although it would be informative to know whether it occurred in a direct or sequential process.

The present work is a, first step, in the investigating of the photodetachment from O^- far above the threshold, by being the first to measure the ratio between the single and double detachment channel of O^- , utilizing a crossed beam setups and a FEL. Furthermore, the experiment indicates that mostly the lower states (3P and 1D) in the O^0 are populated, despite sufficient energy to reach higher states. The energy resolution has to be improved in order to find the branching ratio between these low excited states, however, this does not seem plausible with the short TOF in the current spectrometer. The TOF could be increased by a magnetic field, but this would require some calibration.

It would be advantageous to improve the signal to background ratio of the photoelectrons, which could be done by achieving a better vacuum to reduce the amount of residual gas, but even obtaining the low 10^{-10} mbar at present is not straight forward. Another approach would be to increase the ion current, e.g. by using a more intense ion source.

Lastly, increasing the rate of FEL pulses (i.e. more than 50 pulses pr train) would bring the needed beam time down. By sending the pulse trains with a repetition rate of 5Hz, a total of 800 pulses per train have been demonstrated at FLASH [13]. This would yield an effective number of $4 \cdot 10^3$ pulses per second, 8 times higher compared to the 500 pulses per second used in this study. The temporal distance between pulses in a train was $1\mu\text{s}$, and as the TOF for the particles to DET2 in this experiment

was $4.9\mu\text{s}$ and $5.1\mu\text{s}$ this could actually be within the working conditions depending on the system to investigate.

7.5 Conclusion

It has been demonstrated how all detachment channels from a negative ion can be analyzed to find the relative detachment cross sections by utilizing a crossed beam setup at a FEL.

At 41.7nm the cross section for single detachment from O^- was found to be

$$\sigma_{\text{O}^0} = 2.1 \pm 0.6 \cdot 10^{-19} \text{cm}^2 \quad (7.8)$$

and ratio of single to double detachment from O^- was found to be

$$\frac{\sigma_{\text{O}^0}}{\sigma_{\text{O}^+}} = 4.12 \pm 0.17. \quad (7.9)$$

Hence, a complete characterization of the detachment process from O^- and possible other anions can be performed in the XUV regime utilizing a crossed beam setup in combination with a FEL. This complements the high precision measurements already performed at synchrotron radiation sources to find the detachment cross section for channels with positive fragments.

A photoelectron-photofragment coincidence analysis indicates that single electron detachment from the oxygen anion O^- (^2P) ends in the lower excited states of O^0 (^3P and ^1D).

Lifetimes of an excited state of H_2O^+

The water cation (H_2O^+) has been probed at TIFF with a $\lambda = 532\text{nm}$ photon ($E_\lambda = 2.33\text{eV}$) below the threshold of dissociative excitation of the ground state ($\tilde{X} \ ^2\text{B}_1$). Utilizing the crossed beam momentum imaging setup two fragmentation channels are observed ($\text{OH}^0 + \text{H}^+$ and $\text{OH}^+ + \text{H}^0$), both determined to originate from the second excited state ($\tilde{\text{B}} \ ^2\text{B}_2$). By the means of an electrostatic ion trap the lifetime of the $\text{OH}^0 + \text{H}^+$ channel was measured to be $\tau_{\tilde{\text{B}} \ ^2\text{B}_2} = 198 \pm 11\mu\text{s}$.

The results are published in [43].

8.1 The water cation

The water cation is found in naturally occurring plasmas, for instance, in the Earth's ionosphere [44, 45], in comet tails [46, 47], and in several regions of the interstellar medium [48–51]. In these plasmas water ions participate in reactions that influence the thermal and chemical properties of the environment as formulated in several model chemistries [52–56].

The low energy levels and dissociation limits of the water cations are schematically shown in Figure 8.1, while a more extensive description can be found H. H. Harris and J. J. Leventhal [57]. Additionally, the size of a $E_\lambda =$

2.3eV photon is marked with a green vertical arrow showing the accessible states in this experiment. The electronic ground state of the water cation ($\tilde{X}^2\text{B}_1$) has C_{2v} symmetry like neutral water though at an equilibrium angle of $\angle\text{HOH} = 110.46^\circ$ and bond length $R_{\text{O-H}} = 0.9988\text{\AA}$, [58]. The electron configuration of the ground state is $(1a_1)^2(2a_1)^2(1b_2)^2(3a_1)^2(1b_1)^1$. This corresponds to an ionization of one of the $1b_1$ electrons in neutral water.

Two excited states of H_2O^+ exist below the dissociation limits. One arises by ionization of neutral water from the $3a_1$ orbital (forming $\tilde{A}^2\text{A}_1$), and the other from ionization from the $1b_2$ orbital (forming $\tilde{B}^2\text{B}_2$), [3]. The different orbitals involved results in different equilibrium structures of the two excited states. The $\tilde{A}^2\text{A}_1$ state is linear, while the $\tilde{B}^2\text{B}_2$ state are strongly bent. At linear geometry the $\tilde{X}^2\text{B}_1$ and $\tilde{A}^2\text{A}_1$ constitute a degenerate Renner-Teller system, a $^2\Pi$ state, [59]. At an intermediate angle there is a conical intersection between $\tilde{A}^2\text{A}_1$ and $\tilde{B}^2\text{B}_2$ [60–62]. The $\tilde{B}^2\text{B}_2$ state has a spin-orbit coupling to the unbinding $\tilde{a}^4\text{B}_1$ state [62]. All these nonadiabatic interactions in such a small molecules makes the water cation an interesting benchmark system in molecular physics and makes the decay dynamics more complicated to predict.

Experimentally, the three bound states have been investigated and characterized by photoelectron spectroscopy [63], photofragment spectroscopy [3] and photoelectron-photofragment coincidence spectroscopy [25, 64]. The transitions between the $\tilde{A}^2\text{A}_1$ and $\tilde{X}^2\text{B}_1$ states have been characterized both via emission [58] and absorption [65] spectroscopic studies in the infrared and visible range. Weis et al. [66] have reported that the vibrational levels of the ground state ($\tilde{X}^2\text{B}_1$) can only decay by infrared emissions with lifetimes in the range of milliseconds. This, however, has so far not been experimentally confirmed.

Electrical dipole transitions from the first excited state ($\tilde{A}^2\text{A}_1$) are allowed to the ground state, but can be strongly influenced by the Franck-Condon factor due to the different nuclear geometries. Direct measurements of lifetimes of vibrational levels on the $\tilde{A}^2\text{A}_1$ potential surface have been performed by observing the optical emission spectrum of the \tilde{A} - \tilde{X} transition as a function of time after generation of ions by impact of energetic electrons on water vapor. Thus, lifetimes of the vibrational levels ($v = 9-15$) of H_2O^+ ($\tilde{A}^2\text{A}$) were initially reported to be around $1\mu\text{s}$ [67, 68]; however, a later

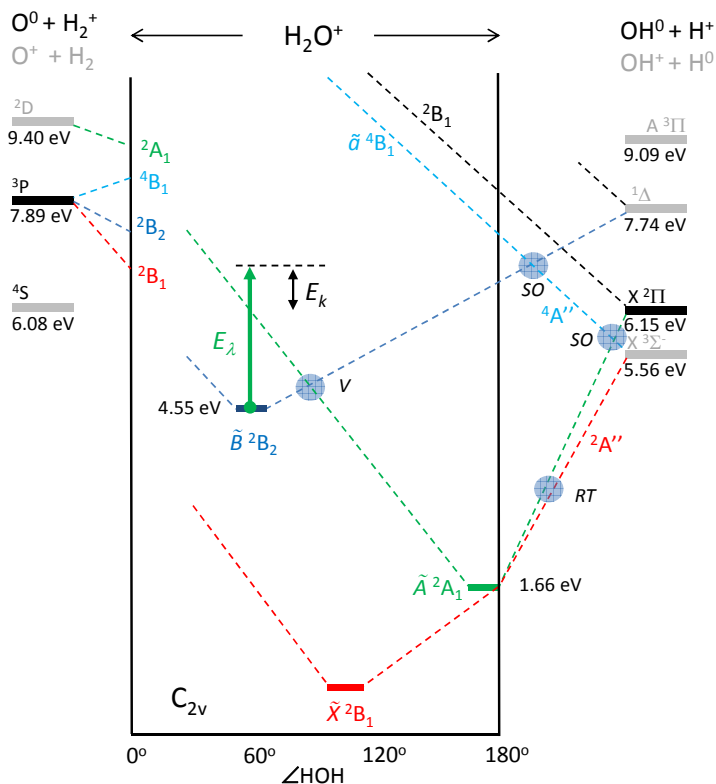


Figure 8.1: Illustration of the energy levels and geometries of the low energy states of H_2O^+ . The possible dissociation channels are marked on the sides and the dashed line indicate the existence of potential energy curves (PEC). The non-adiabatic couplings between PEC are marked with small circles. RT: Renner-Tenner, SO: Spin-orbit. V: vibronic (the asymmetric stretch, ν_3). A $\lambda = 532\text{nm}$ photon ($E_\lambda = 2.33\text{eV}$) is marked with the green arrow.

experiment [69] using a similar experimental approach found lifetimes in the range of $10.5\mu\text{s}$. The discrepancy was attributed to the perturbation by space-charge effects in the setups of the early experiments [67].

The second excited state ($\tilde{\text{B}}^2\text{B}_2$) can couple radiatively to the $\tilde{\text{A}}^2\text{A}_1$ state, while direct radiative transitions to the ground state $\tilde{\text{X}}^2\text{B}_1$ are dipole forbidden. Furthermore, the $\tilde{\text{B}}^2\text{B}_2$ state has conical intersections

with both the \tilde{A}^2A_1 state and \tilde{a}^4B_1 , leading to vibronic and spin-orbit couplings, respectively, that strongly influence the predissociation dynamics of this state. The lowest vibrational levels of the \tilde{B}^2B_2 state cannot be predissociated, as they are located below all dissociation limits, and their decay properties have not been observable in previous studies [3]. Evidently, the decay of these low vibrational levels of the \tilde{B}^2B_2 state can be influenced both by radiative transitions to the \tilde{A}^2A_1 state and by the above-mentioned nonadiabatic couplings. In a photoelectron-photoion coincidence experiment, on vacuum ultraviolet ($\lambda = 10\text{-}200\text{nm}$) ionized neutral water molecules, Norwood and Ng [25] in fact reported the observation of metastable states of H_2O^+ that occurred on a time scale of $10\mu\text{s}$; these states were tentatively attributed to an ultrafast (nonadiabatic) coupling from the \tilde{B}^2B_2 state to the \tilde{A}^2A_1 state, followed by radiative relaxation from the \tilde{A}^2A_1 state to the \tilde{X}^2B_1 state.

8.2 The experiment

The experiment was performed at TFFF. The experimental setup is described in chapter 3.

The ions were produced in the hollow cathode ions source by maintaining a discharge of 654V and 29mA in a 0.2 mbar pressure of deionized water vapor, resulting in a total current of H_2O^+ of $I_{H_2O^+} \approx 5\text{nA}$. The kinetic energy of the ions was 2.0kV, resulting in a time of flight (TOF) of $\sim 60\mu\text{s}$ from ion source to the interaction.

A Nd:YAG laser (See section 3.9) delivered vertically polarized photons at a wavelength of 532nm ($E_\lambda = 2.33\text{eV}$) in pulses of $\sim 3\text{-}5\text{ns}$ width with adjustable photon pulse energies in the range $E_\gamma = 3\text{-}11\text{mJ/pulse}$. The photon and ion beam were crossed at an 45° angle.

The pressure in the interaction region was $p \sim 4 \cdot 10^{-10}\text{mbar}$ during the measurements.

The beam positions and profiles were measured for both the photons and ions and are shown in Figure 8.2. Both vertical beam profiles are well approximated by gaussian distributions of standard deviation 0.41 mm and 0.62 mm, and being slightly off-centered ($\sim 0.26\text{mm}$) from each other.

The vertical overlap factor (See equation (2.19)) was determined to be $F = 5.4 \pm 0.1 \text{cm}^{-1}$.

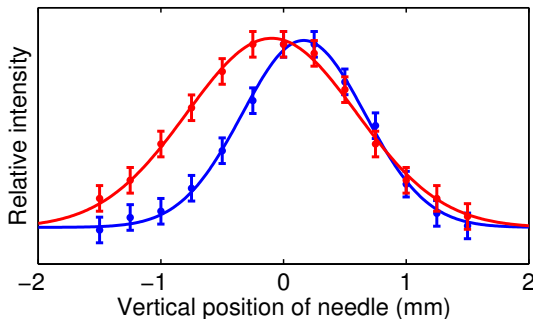


Figure 8.2: Vertical profiles of the ion (blue dots) and photon (red dots) beams measured with the 1-mm insertable needle in the middle of the interaction region. The curves show the Gaussian fits to the profiles.

The detector setup of TIFF is shown in Figure 3.1 and in this study DET1 was used to detect light fragments (H^0 and H^+) and DET2 to detect the neutral OH^0 , while the electrostatic mirror was used to bend the OH^+ towards DET3 for detection, and at the same time allow H_2O^+ to pass and be deflected towards the beam dump.

For the present investigation three of the operation modes of the interaction region were utilized. The different modes are introduced in section 3.5.

The field free mode was used to measure the momentum and energy of fragments.

A 100V bias was applied to distinguish H^+ , H_2^+ and H^0 on DET1 by temporal separation according to their charge to mass ratio.

In the last mode the ion trap was activated, trapping the H_2O^+ molecules for various times. The ions were injected into the trap by lowering the entrance mirror to ground potential and rapidly ($< 100\text{ns}$) raise it to full potential, once a bunch of ions have entered. Thereby, the H_2O^+ molecules will oscillate back and forth. The neutral fragments H^0 and OH^0 are unhindered by the mirrors. Hence, the neutral fragments from a molecule moving towards the detector can be detected. When the exit potentials are high the charged fragments H^+ and OH^+ can not leave the ion trap. This mode was used to measure the background-subtracted, photon-induced signal of H^0 and OH^0 at various times.

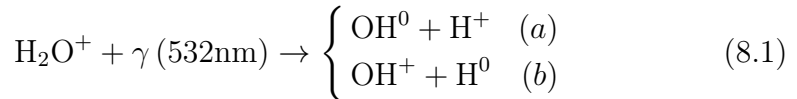
8.3 Results

8.3.1 Photodissociation channels

Figure 8.3 shows the number of detected fragment on all three detectors (DET1-3) after photodissociation of H_2O^+ at $\lambda = 532\text{nm}$. The diagonal plots show the background-subtracted, photon-induced and non-correlated yield in two situations. With the interaction region at ground potential (gray curve) and with a 100V bias (blue curve). The expected longitudinal momentum $(1 - 1/\tau)$ for H^0 , H^+ , H_2^+ , O^+ and OH^+ in the biased situation was found from simulations in SIMION and marked in plot (11) and (33), respectively. Plot (11) clearly shows that no H_2^+ was detected on DET1 and similarly plot (33) shows that no O^+ (33) was observed on DET3.

The off-diagonal plots show the result of a coincidence analysis. Plot (12) and (21) gives the correlation between DET1 and DET2 and clearly shows that H^+ and OH^0 comes in coincidence. Plot (13) and (31) shows a smaller but distinct coincidence between H^0 and OH^+ . The TOF distributions in plot (23) and (32) fluctuates around zero but (luckily!) gives no surplus of OH^0 and OH^+ in coincidence.

Therefore, the two measured channels are:



By looking at the intensities of H^0 and H^+ in plot (11) in Figure 8.3 channel (8.1)(a) appears to be much more intense than channel (b). To compare the relative size of the channels, the detection efficiency (ϵ_F) for fragment F must be taken into account. The detection efficiency includes both the actual efficiency of the MCP plate and the geometry of the setup; transmission from the interaction region including the geometrical properties of the central hole in DET1. The number (N_X^F) of detected fragments (F) from a reaction (X) can be found as

$$\begin{aligned} N_1^{\text{H}^+} &= \epsilon_{\text{H}^+} R_a & , & & N_1^{\text{H}^0} &= \epsilon_{\text{H}^0} R_b \\ N_2^{\text{OH}^0} &= \epsilon_{\text{OH}^0} R_a & , & & N_3^{\text{OH}^+} &= \epsilon_{\text{OH}^+} R_b \end{aligned} \quad (8.2)$$

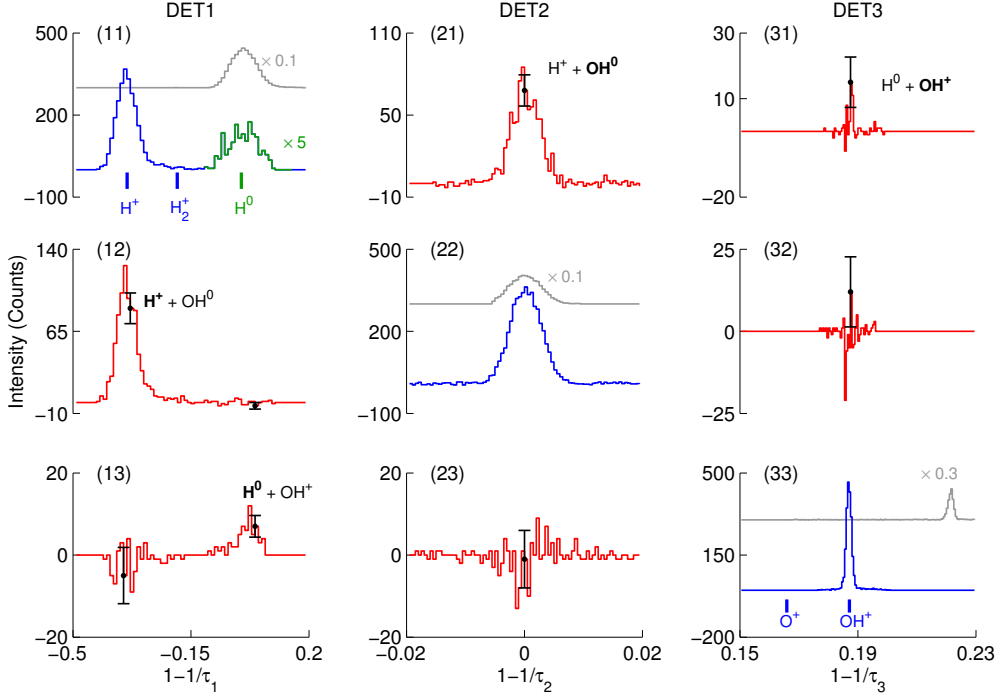


Figure 8.3: The observed intensity in a photofragmentation study of H_2O^+ after exposure to $\lambda = 532\text{nm}$ photons. The background-subtracted, photon-induced distributions of the uncorrelated fragments detected on DET1-3 with the interaction region at a potential of $U_{\text{Bias}} = 100\text{V}$ (blue curve) and $U_{\text{Bias}} = 0\text{V}$ (gray curve) are shown in the diagonal plots. The latter have been scaled as indicated. The expected, simulated momentum of H^+ , H_2^+ , H^0 , O^+ and OH^+ in the biased situation have been marked. For DET1, the temporal interval for H_0 -fragments have been scaled (green curve). The off-diagonal plots shows the intensity of true coincidences between the different detectors. For selected values the statistical uncertainty have been indicated.

where R_X is the number of reactions (8.1)(a) or (b).

$$R_X = N_\gamma \cdot l_I \cdot F \cdot \sigma_X \quad (2.20)$$

Similarly, the measured intensities of fragments in coincidence can be

obtained

$$N_{1\&2} = \epsilon_{H^+} \epsilon_{OH^0} R_a \quad , \quad N_{1\&3} = \epsilon_{H^0} \epsilon_{OH^+} R_b \quad (8.3)$$

From (8.2) and (8.3) the detection efficiencies for each fragment type can be found

$$\begin{aligned} \epsilon_{H^+} &= \frac{N_{1\&2}}{N_2^{OH^0}} = (17.8 \pm 0.9)\% \\ \epsilon_{H^0} &= \frac{N_{1\&2}}{N_1^{H^+}} = (1.7 \pm 1.0)\% \\ \epsilon_{OH^0} &= \frac{N_{1\&2}}{N_2^{OH^0}} = (30.9 \pm 1.8)\% \\ \epsilon_{OH^+} &= \frac{N_{1\&2}}{N_2^{N_1^{H^0}}} = (19.0 \pm 3.3)\% \end{aligned} \quad (8.4)$$

The first thing that springs to mind might be the huge difference between the detection efficiency for H^+ and H^0 . This is presumable due to the setup around DET1. At this measurement the front of DET1 was kept at -3000V. This would affect the fragments passing the detector and all fragments must pass through this region. Hence, a grounded mesh are installed in front of DET1, shielding the potential. As the H^+ fragments passes the mesh, they are accelerated towards the surface of the detector, and arrive with an kinetic energy 3keV higher than the neutral H^0 . When the H_2O^+ has a kinetic energy of $E_I = 2\text{keV}$, the energy of the hydrogen fragments will be on the order of

$$(m_H/m_{H_2O^+})E_I = 0.1\text{keV} \quad (8.5)$$

disregarding any small contribution from energy released in the fragmentation and the bias potential. As a MCP plate is sensitive to the kinetic energy, this could be an explanation.

As the photon flux and the number of ions before reaction are identical for the two channels, the ratio between their cross section can be found as the ratio between the number of reactions taking place.

$$\frac{\sigma_{OH^0+H^+}}{\sigma_{OH^++H^0}} = \frac{R_a}{R_b} = \frac{N_2^{OH^0}}{N_3^{OH^+}} \frac{\epsilon_{OH^+}}{\epsilon_{OH^0}} = 1.3 \pm 0.3. \quad (8.6)$$

This makes channel (8.1)(a) slightly larger than channel (b), however, not as much as suggested from the directly measured intensities shown in Figure 8.3.

8.3.2 Origin of the photodissociation at 532 nm

With the active channels established, the next step would be to locate the initial state in H_2O^+ and the final states for the observed fragments. This information might be found by comparing the energy difference between the internal energy of the initial state (E_i) in H_2O^+ and the internal energy of the final state (E_f) of the fragments to the energy diagram in Figure 8.1. However, due to the low efficiency to detect H^0 the statistics for channel (8.1)(b) be have been insufficient, and channel (a) will receive the main focus.

The energy balance for the process $\text{H}_2\text{O}^+ + \gamma(532\text{nm}) \rightarrow \text{OH}^0 + \text{H}^+$ can be written

$$E_i^{\text{H}_2\text{O}^+} + nE_\lambda = E_f^{\text{OH}^0} + E_k \quad (8.7)$$

where nE_λ is the total energy from photon absorption and E_k is the kinetic energy released. Hence, both the number of photons absorbed and any kinetic energy released must be determined to find the energy difference between the initial and final state.

To determine the number of photons involved, the number of channel (8.1)(a) reactions (measured as OH^0 counts on DET2) have been plotted in Figure 8.4 as a function of photon pulse energy (E_γ).

If only one photon is absorbed, the number of detected OH^0 will be on the form given in equation(2.17)

$$N_a \propto 1 - e^{-\phi_\gamma \sigma_a \Delta t} = 1 - e^{-\frac{E_\gamma \sigma_a}{A_\gamma E_\lambda}}, \quad (8.8)$$

where Δt is the photon pulse duration, $E_\gamma = E_\lambda N_\gamma = E_\lambda \phi_\gamma A_\gamma \Delta t$ is the photon pulse energy, E_λ is the energy per photon, ϕ_γ is the photon flux and A_γ is the cross-sectional area of the laser pulse in the interaction region overlapping the ion beam. In the low intensity limit ($\frac{E_\gamma \sigma_a}{A_\gamma E_\lambda} \ll 1$) this gives $N_a \propto E_\gamma$.

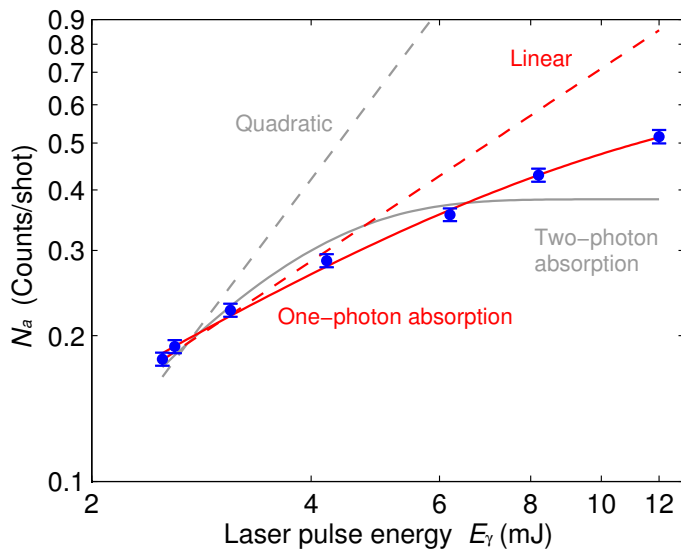


Figure 8.4: The measured yield of OH^0 on DET2 as a function of photon pulse energy (E_γ). The solid lines show a fit to the measured values by the exact expression for single (red) or double (gray) photon absorption. The dashed lines show the expression for in the low photon flux limit.

If two photons are absorbed the dependence will be on the form (2.26)

$$N_a \propto 1 - e^{\phi_\gamma^2 \sigma_a^{(2)} \Delta t} = 1 - e^{-\frac{E_\gamma^2 \sigma_a^{(2)}}{A_\lambda^2 E_\lambda^2 \Delta t}} \quad (8.9)$$

For two photon absorption the low flux limit will be $N_a \propto E_\gamma^2$.

These four models have been fitted to the measured values and plotted in Figure 8.4. For the low flux approximation the slope must be constant. However, the data expresses a small curvature indicating a depletion. Hence, these two models (dashed curves) have only been fitted at low pulse energy ($E_\gamma < 4\text{eV}$) and in this case there is an agreement between the one-photon model and the data, however, the two photon model overestimates the fragment yield. As the data has a curvature, clearly the approximation of low intensity is a poor match to the data.

The best fit to the two photon model with depletion of absorbing molecules (solid gray curve) bends too fast and fails to describe the data.

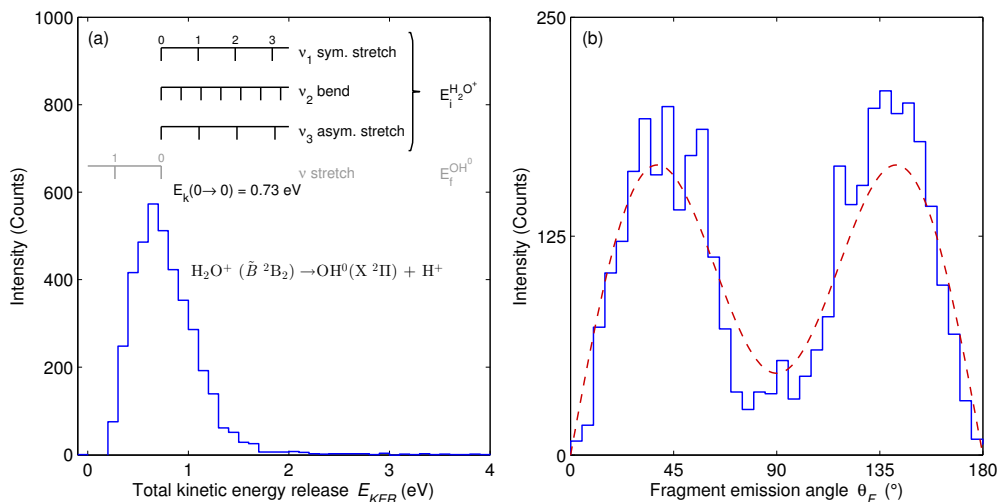


Figure 8.5: Kinematic analysis of the observed photodissociation channel $\text{H}_2\text{O}^+ + \gamma(532\text{nm}) \rightarrow \text{OH}^+ + \text{H}^+$. Plot (a) shows the obtained distribution of released kinetic energy in the process. In the top of the figure the energy levels of possible vibrational excitation for the initial state in H_2O^+ (black) and final in OH^+ (gray) state are indicated. Plot (b) shows the angular distribution of OH^+ fragments detected on DET2 (blue curve) and a fit to the expected angular distribution of fragments (equation (2.31)).²

The single photon absorption model with a saturation (solid red) fits the data perfectly, and it can be assumed only one photon was absorbed.

The kinetic energy released from the process in channel (8.1)(a) can be obtained from the OH^+ and H^+ fragments in coincidence as described in section 2.5.

The distribution of the total experimental kinetic energy released in channel (8.1)(a) is plotted in Figure 8.5(a). The distribution peaks at $E_{\text{KER}} = 0.66\text{eV}$, has a full width at half maximum (FWHM) of $\sim 0.7\text{eV}$ and displays a tail towards higher energies.¹

¹See the footnote of Figure 8.5

The observed photodissociation signal is likely to originate from one of the three lowest electronic states of H_2O^+ . The $\tilde{X}^2\text{B}_1$ ground state of H_2O^+ is bound by $\sim 5.56\text{eV}$ relative to the first dissociation limit ($\text{OH}^+ (\text{X}^3\Sigma^-) + \text{H}^0$) and only very high vibrationally excited levels of this state could be responsible for the observed photodissociation with a single $E_\lambda = 2.33\text{eV}$ photon. Similarly, the first excited state ($\tilde{A}^2\text{A}_1$) lies $\sim 3.90\text{eV}$ below the first dissociation limit, and also here, only highly excited vibrational levels can be attributed to the photodissociation signal at $\lambda = 532\text{nm}$. Moreover, the lifetimes of high vibrational levels of the $\tilde{A}^2\text{A}_1$ state have already been addressed experimentally [69] and were found to be on the order of $10\mu\text{s}$. In the present experiment, the direct time of flight from the ion source to the interaction region is about $60\mu\text{s}$, and hence it also seems unlikely that the $\tilde{A}^2\text{A}_1$ state could be the origin of the observed photodissociation signal.

Hence, the most likely initial state is the second excited state ($\tilde{B}^2\text{B}_2$) only 1.01eV below the first dissociation limit. The $\tilde{B}^2\text{B}_2$ state, however, does not directly couple to the energetically lowest final states in OH^0 and OH^+ . But if the $\tilde{B}^2\text{B}_2$ state absorbs into a repulsive part of the $\tilde{A}^2\text{A}_1$ state it could pre-dissociate into either the $\text{OH}^+ (\text{X}^3\Sigma^-) + \text{H}^0$ or the $\text{OH}^0 (\text{X}^2\Pi) + \text{H}^+$ channel.

The possible vibrational modes in both H_2O^+ and OH^0 and energy spacing for each mode are indicated in the top part of Figure 8.5a. The vibrational energies of the symmetric stretch $\nu_1 = 0.37\text{eV}$ and the bend $\nu_2 = 0.20\text{eV}$ of the $\tilde{B}^2\text{B}_2$ states are known from photoelectron spectroscopy [70], while for the asymmetric stretch $\nu_3 = 0.38\text{eV}$ are calculated by Lorquet and Lorquet [62]. The OH^0 stretch $\nu = 0.46\text{eV}$ can be found at the Nist Chemistry WebBook [42].

The vibrationally ground state to ground state transition from $\tilde{B}^2\text{B}_2$ to $\text{OH}^0 (\text{X}^2\Pi) + \text{H}^+$ almost perfectly fits the center point of the experimental distribution and even some vibrational excitation in the initial and final state would fit the observed distribution.

²The energy distribution in Figure 8.5(a) shows E_{KER} . However in the corresponding figure in the published article [43] the labels falsely claimed it to be the single fragment energy E_F . Furthermore the theoretically expected value have been corrected to be $E_{\text{KER}} = 0.73\text{eV}$ by including all significant numbers of the energy level of the $\tilde{B}^2\text{B}_2$ state given in Figure 8.1.

The angular distribution of OH^0 relative to the photon polarization (see (2.38)) are shown in Figure 8.5(b) as an extra information. The distribution is well described by the asymmetry parameter β (See equation (2.31)) and the fit result shown in Figure 8.5(b) gives a value of $\beta = 1.4 \pm 0.2$. This value might be used as evidence of a particular dissociation route, e.g. confirming the suggested $\tilde{\text{B}}^2\text{B}_2$ to $\tilde{\text{A}}^2\text{A}_1$ absorption.

To sum up, the initial state seems to be the $\tilde{\text{B}}^2\text{B}_2$ state, which absorbs only one photon and ends up in either OH^+ ($\text{X }^3\Sigma^-$) + H^0 ($^2\text{S}_{\frac{1}{2}}$) or OH^0 ($\text{X }^2\Pi$) + H^+ . For the latter the expected and observed kinetic energy release are in good agreement.

8.3.3 Lifetime of the $\tilde{\text{B}}^2\text{B}_2$ state

Assuming all photoinduced signals originate from the $\tilde{\text{B}}^2\text{B}_2$ state, the lifetime of the $\tilde{\text{B}}^2\text{B}_2$ state can be measured as the background-subtracted photon-induced signal as a function of time. But as H^+ and OH^+ cannot escape the ion trap and the detection efficiency of H^0 on DET1 is small, the OH^0 fragments if the most efficient fragment to monitor as a function of time. To effectuate this the electrodes in interaction region were operated to trap H_2O^+ in the time interval from $60\mu\text{s}$ to $2500\mu\text{s}$. Where $60\mu\text{s}$ corresponds to the TOF from the ion source to the interaction region with a beam energy of 2keV .

However, photodissociation is not the only dissociation channel of H_2O^+ . In Figure 8.6(a) the recorded ion count (N_I) on DET2 (H_2O^0 , OH^0 and O^0) in the “Ions only” recording mode is plotted as a function of trapping time. This reveals a rapid decay at smaller times ($t < 200\mu\text{s}$) and an almost flat tail towards larger times ($t > 1000\mu\text{s}$). The rapid decay is common for this type of ion traps and seems to originate from a non-perfect matching between the incoming molecules and the geometry of the ion trap, resulting in population of quasistable orbits during the injection [71]. The long term decay is most probably pressure related and arises from collisions with the residual gas in the vacuum chamber. Both unstable orbits and residual gas collisions are independent of the internal state of H_2O^+ and hence, the ion count (N_I) is directly proportional to the number of stored H_2O^+ ions and can be estimated by the number of counts in the Ions only acquisition

mode.

$$N_I(t) \propto N_{\text{H}_2\text{O}^+}(t) \quad (8.10)$$

The observed fragment count as a function of trapping time was modeled by the sum of three exponentials. The initial decay from unstable orbits is not exponential, but rather obeys a power series, but the total agreement with the model is acceptable at present. From the model the long term pressure related storage time of H_2O^+ in the ion trap was found to be $\tau > 100\text{ms}$.

Figure 8.6(b) shows the background-subtracted, photon-induced signal. The induced signal are clearly not stable for the first $200\mu\text{s}$ probably reflecting the decay of unstable orbits or an non-uniform temporal distribution in the ion trap. At later times ($t > 200\mu\text{s}$) the signal agrees with an expected single exponential decay. As discussed in the previous section only the $\tilde{\text{B}}^2\text{B}_2$ state will contribute to the photon induced signal (N_a) and hence the counts are directly proportional to the number of H_2O^+ in the $\tilde{\text{B}}^2\text{B}_2$ state in the ion trap. Furthermore, as the $\tilde{\text{B}}^2\text{B}_2$ state is below the dissociation limit it can only decay to a lower internal state in the water cation. Therefore the relation to the total number of H_2O^+ must be

$$N_a(t) \propto N_{\tilde{\text{B}}^2\text{B}_2}(t) \propto N_{\text{H}_2\text{O}^+}(t)e^{-\frac{t}{\tau_{\tilde{\text{B}}^2\text{B}_2}}} \quad (8.11)$$

where $\tau_{\tilde{\text{B}}^2\text{B}_2}$ is the lifetime of the $\tilde{\text{B}}^2\text{B}_2$ state. This indicates that the $N_a(t)$ contains both the decay of the H_2O^+ and the decay of the second excited state. Therefore, the lifetime of the excited state can be deduced from the ratio of the background-subtracted, photon-induced signal and the decay of H_2O^+ obtained from the Ions only mode.

$$\frac{N_a(t)}{N_I(t)} \propto e^{-\frac{t}{\tau_{\tilde{\text{B}}^2\text{B}_2}}} \quad (8.12)$$

The N_a counts have hence been normalized to the model describing the Ions only signal decay and have been plotted in Figure 8.6(c). From the slope the lifetime of the low vibrational states of the $\tilde{\text{B}}^2\text{B}_2$ state have been determined to be

$$\tau_{\tilde{\text{B}}^2\text{B}_2} = 198 \pm 11\mu\text{s} \quad (8.13)$$

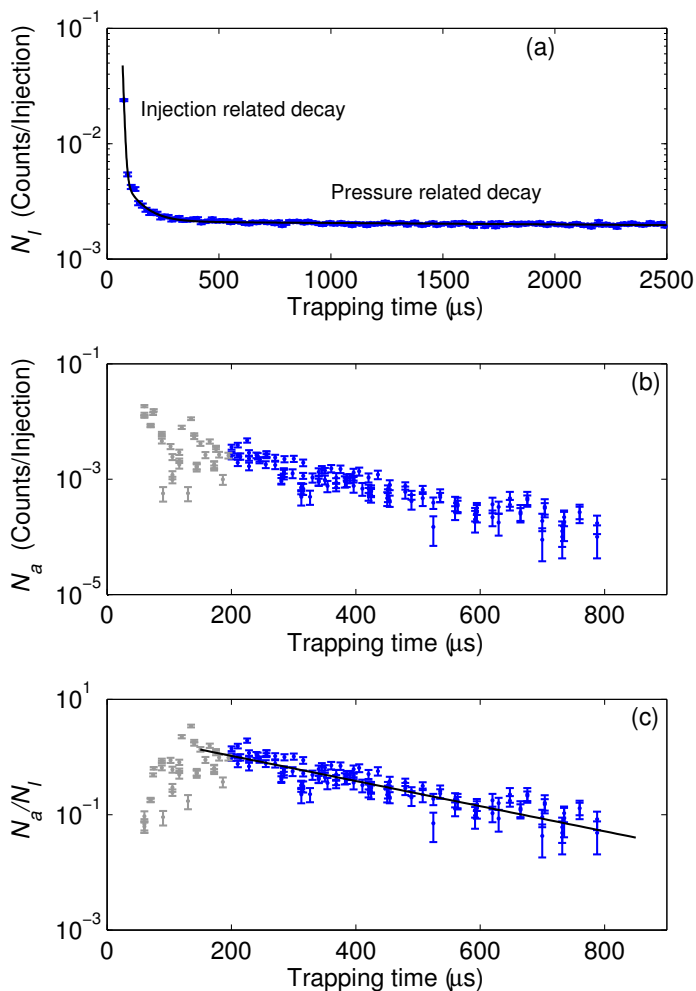


Figure 8.6: Observed decay of the fragment signal produced in the electrostatic ion trap. Plot (a) shows the distribution of fragments recorded in the Ions only mode. This signal is not photon-induced and most likely originate from injection to unstable orbits and collisions with the residual gas. Plot (b) shows the background-subtracted, photon-induced signal, and plot (c) shows the photon-induced signal normalized to the decay of the parent beam obtained from in plot (a) to isolate the decay of the \tilde{B}^2B_2 state.

8.4 Discussion

8.4.1 Decay dynamics of excited states of H_2O^+

The existence and quantification of the lifetime of the $\tilde{\text{B}}^2\text{B}_2$ state might shed light on two aspects of the physics of the excited states of the water cation. Firstly, a meta stable state in H_2O^+ was discovered by Norwood and Ng [25], who concluded there that might be a state in H_2O^+ with a lifetime in the order of $10\mu\text{s}$, the timescale of their experiment. By the explicit value given here it might be possible to model the decay dynamics and test whether a nonadiabatic or radiative interaction best describe the coupling to the $\tilde{\text{A}}^2\text{A}_1$ state.

Secondly, if the $\tilde{\text{B}}^2\text{B}_2$ state couple to the $\tilde{\text{A}}^2\text{A}_1$ state, the $\tilde{\text{A}}^2\text{A}_1$ state will start with the nuclear geometry of the $\tilde{\text{B}}^2\text{B}_2$. Clearly not a relaxed geometry and in the repulsive part of the $\tilde{\text{A}}^2\text{A}_1$ PES. If both the observed channels ($\text{OH}^0 + \text{H}^+$ and $\text{OH}^+ + \text{H}^0$) from the $\tilde{\text{B}}^2\text{B}_2$ state passes the $\tilde{\text{A}}^2\text{A}_1$ the determined branching ratios $\frac{\sigma_a}{\sigma_b} = 1.3 \pm 0.3$, holds information about the strength of the nonadiabatic couplings in this energy range.

An interesting experiment in the future could clearly be isotope substituted species HDO^+ and D_2O^+ or isoelectronic species H_2S^+ to test whether any of these would express a similar long lived behavior.

8.4.2 Fraction of $\tilde{\text{B}}^2\text{B}_2$ states in the ion beam

It has not been possible to calculate the cross section (σ_X) for either of the two channels (X), as the number of H_2O^+ initially in the $\tilde{\text{B}}^2\text{B}_2$ state remains unknown. The relation between the number of detected fragments, the cross section and the number of H_2O^+ initially in the $\tilde{\text{B}}^2\text{B}_2$ state can be approximated by

$$N_X = \phi_\gamma N_{\tilde{\text{B}}^2\text{B}_2} \sigma_X \Delta t \quad (2.18)$$

$$= (N_\gamma) \left(N_I \cdot p_{\tilde{\text{B}}^2\text{B}_2} \cdot F \right) \sigma_X \cdot P_\gamma \cdot \epsilon_X \quad (8.14)$$

Where $N_\gamma \approx 1.3 \cdot 10^{16}$ is the average number of photons per pulse, $N_I = \frac{I}{q_I v_I} = \frac{5\text{nA}}{1\text{C} \cdot 1.8 \cdot 10^5 \frac{\text{m}}{\text{s}}} = 1.7 \cdot 10^5$ is the number of ion in the interaction region given by the ion current (I), charge (q_I) and speed (v_I), $p_{\tilde{\text{B}}^2\text{B}_2}$ is the

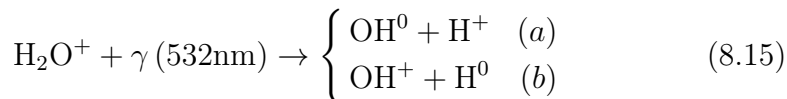
percentage of H_2O^+ in the $\tilde{\text{B}}^2\text{B}_2$ state, $F = 5.4 \pm 0.1\text{cm}^{-1}$ is the vertical overlap factor, $P_\gamma = 7.2 \cdot 10^4$ is the number of photon-ion crossings and $\epsilon_{\text{OH}}^0 = (30.9 \pm 1.8)\%$ is the detection efficiency for OH^0 assuming we pick channel (a) as an example.

For the sake of getting an estimate, let us assume that all H_2O^+ molecules are in the $\tilde{\text{B}}^2\text{B}_2$ state, $p_{\tilde{\text{B}}^2\text{B}_2} = 100\%$. Then the cross section will be in the order of 10^{-20}cm^2 , which seems to be too low. A more realistic cross section for a dipole-allowed process is in the order of 10^{-18}cm^2 , hence a more realistic percentage of molecules in the $\tilde{\text{B}}^2\text{B}_2$ state would be $p_{\tilde{\text{B}}^2\text{B}_2} \sim 1\%$. This would even agree with a previous value of 3-5% given by K. Norwood, A. Ali and C. Y. Ng [25].

8.5 Conclusion

Using the TIFF setup with the ability to perform coincidence fragment momentum imaging a photodissociation at 532nm of H_2O^+ from a hollow cathode ion source was found to originate from the low vibrational levels of the $\tilde{\text{B}}^2\text{B}_2$ state and only involve single photon absorption.

With the crossed beam geometry both charged and neutral fragments could be detected and two photodissociation channels were observed



with the branching ratio $\frac{\sigma_a}{\sigma_b} = 1.3 \pm 0.3$.

By utilizing an ion trap located around the interaction region and measuring the intensity of heavy, neutral fragments (OH^0) the lifetime of channel (a) was found to $\tau_{\tilde{\text{B}}^2\text{B}_2} = 198 \pm 11\mu\text{s}$.

XUV fragmentation of the Zundel cation H_5O_2^+

$\text{H}^+(\text{aq})$ is of fundamental importance in solution chemistry. In aqueous solutions H^+ will interact with the water molecules creating hydrogen bonded complexes. The two simplest of these are the H_5O_2^+ , proposed by Zundel [72] where a central proton is shared between two water molecules, and the H_9O_4^+ , proposed by Eigen [73] where a core hydronium (H_3O^+) is surrounded by three neutral water molecules. These hydrated protons have been identified in water clusters, bulk water and ice structures and are important in fields from cluster science to atmospheric chemistry where protonated water clusters $\text{H}^+(\text{H}_2\text{O})_n$ may represent the earliest stage of cloud formation [74]. Furthermore, the Zundel and Eigen ions have been used as model systems to understand charge mobility in bulk water [75]. The Zundel ion has previously been studied theoretically and experimentally in the infra red (IR) to the ultra violet (UV) range [76–80]. In the extreme ultra violet (XUV) range only a few theoretical studies exist [81, 82]. The only experiment performed in XUV regime has been carried out at TIFR in 2010 [83]. At that point a detector for charged, heavy fragments was not installed and it was not possible to resolve the H_nO^+ ($n = 0-3$) fragments. This has been amended in the present study where branching ratios between 10 fragmentation pathways have been found and the kinetic energy released (KER) in the strongest channel is estimated.

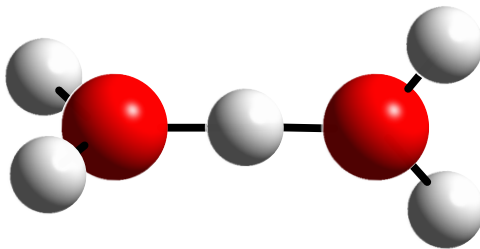
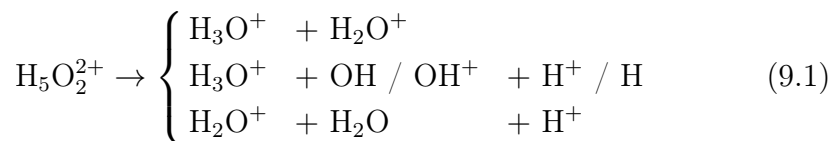


Figure 9.1: *The Zundel cation ($H_5O_2^+$). Two water molecules sharing a proton.*

9.1 The Zundel ion

The Zundel cation is a protonated water dimer. The structure is sketched in Figure 9.1. The geometry can be described as two water molecules loosely bond by a proton located between them. In both water molecules the oxygen lone pair point towards the proton. The HOH angle in each water molecule are close to that of an unbound water molecule $\sim 109^\circ$ and the OHO angle between the two water molecules are close to linear $\sim 176^\circ$ [76]. The electronic ground state of the Zundel ion is $X^1A_1 (C_{2v})$.

Z. Li et.al. [81, 82] have theoretically investigated the fragmentation of $H_5O_2^+$ after XUV photon ionization. They have calculated the potential energy surfaces of the 6 lowest electronic states of the dication ($H_5O_2^{2+}$). The calculations was executed with a complete set of the lowest energy outer-valence electronic states of $H_5O_2^{2+}$. Fragmentation was identified at the end of the calculations by requiring the O-H bond length to be only slightly larger than the average bond length. They found that the decay dynamics starts with the central proton moving towards one of the water groups. The electron hole will move to the opposing water group and the two groups with equal charge will repel each other. Z. Li found ionization with photon energies below 24eV lead to a twobody break up only ($H_3O^+ + H_2O^+$) while at photon energies above 27eV the dissociated groups had sufficient energy to expel a charged or a neutral hydrogen leading to a total of three fragmentation channels.



9.2 The experiment

The experiment was performed at TIFF. The experimental setup is described in chapter 3.

The ions were produced in the hollow cathode ions source by maintaining a discharge of 597V and 29mA in a 3.1mbar pressure of deionized water vapor. The kinetic energy of the ions were 4.2kV and the ion current of H_5O_2^+ was 4nA.

FLASH delivered horizontally polarized photons at a wavelength of $\lambda = 42.1\text{nm}$ ($\lambda_{\text{FWHM}} = 0.3\text{nm}$, $E_\lambda = 29.5 \pm 0.2\text{eV}$) with an average pulse energy of $50\mu\text{J}/\text{pulse}$ before the PG2 beam line. The transmission of the PG2 beam line have been measured to 0.5 ± 0.1 [11], hence the average pulse energy at TIFF was $25\mu\text{J}/\text{pulse}$. The photon pulses arrived as pulse trains with a repetition rate of 10Hz. Each pulse train contains 50 photon bunches separated by $5\mu\text{s}$, and with a duration of $\sim 250\text{fs}$. In total, this amounts to 500 photon-ion crossings per second. The photon and ion beam were crossed at an 90° angle

The pressure in the interaction region was $p = 3-6 \cdot 10^{10}\text{mbar}$ during the measurements.

The detector setup is shown in Figure 3.1 and the fragments from H_5O_2^+ were detected using detector DET1-3. At this high pulse energy the electron detectors are not capable of counting the number of released electrons and were powered down.

For the present investigation the field-free and the bias operation modes of the interaction region were utilized. The different modes are introduced in section 3.5. The field free mode was used to measure the momentum and energy of fragments, while a 200V bias was applied to distinguish H^+ , H_2^+ and H/H_2 on DET1 by temporal separation according to their

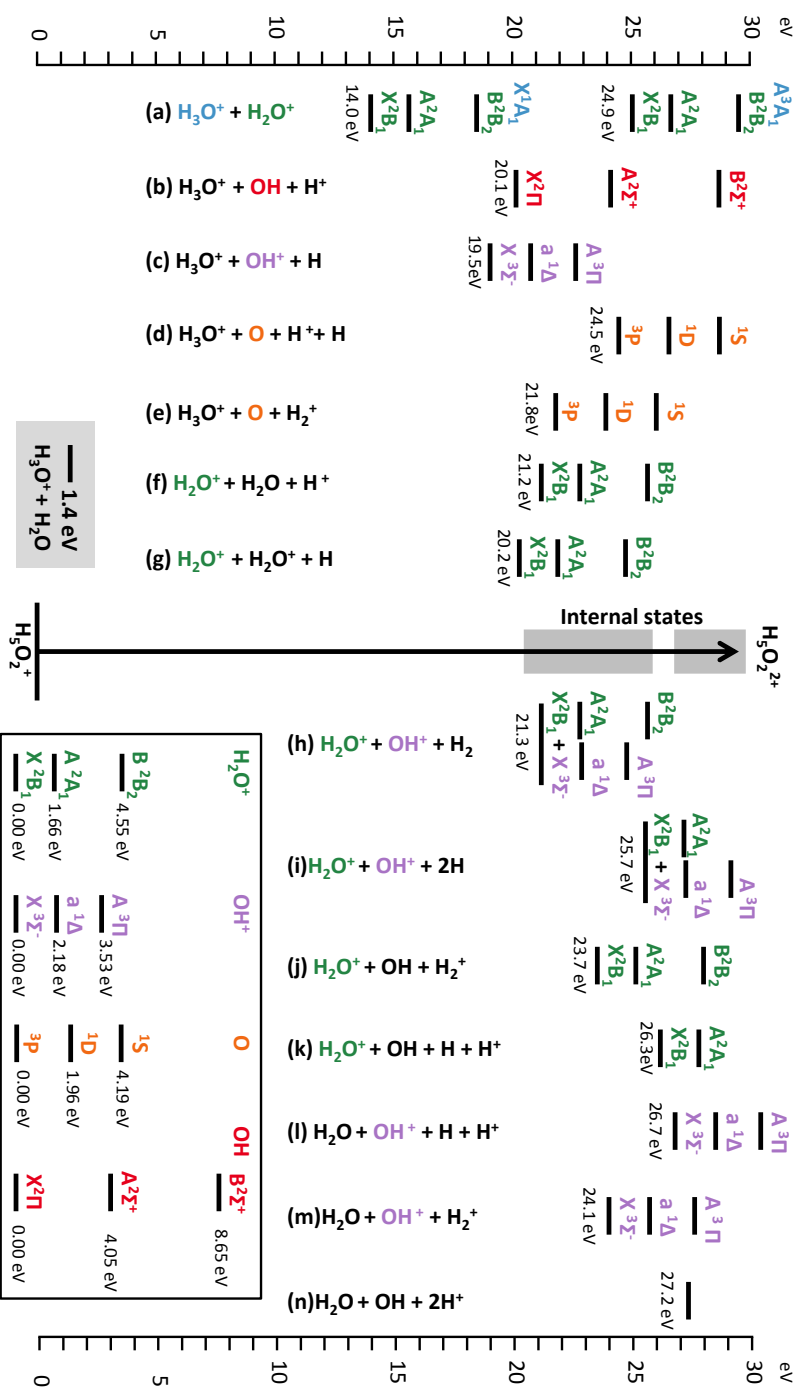


Figure 9.2: Energy diagram for the possible reaction pathways for XUV ionization ($E_{\lambda} = 29.5 \pm 0.2\text{eV}$) of $H_5O_2^+$ and a following fragmentation of $H_5O_2^{2+}$. The energies of internal states and reaction have been obtained from the Nist Chemistry WebBook [42]. The colors have been used to link an internal state to a fragments. The energy of the first excited state of H_3O^+ have been calculated by S. Roszak [84] and the internal state of $H_5O_2^+$ have been calculated by Li et al [82]. The energy of the internal state of $H_5O_2^+$ depends strongly on the position of the central proton and as indicated by the marked energy bands. The inset show the energy of the lowest excited states of H_2O^+ , OH^+ , OH and O . The energy of the lowest excited state of H_2O is in around 7eV and the energy of the lowest excited states of H , H_2 and H_2^+ are around 10eV. Hence, these states have not been included.

charge to mass ratio. The charged, heavy fragments detected on DET3 are automatically separated in time by the electrostatic mirror.

9.3 Results

9.3.1 Branching ratio of fragmentation pathways

Figure 9.3 shows the yields on all three fragment detectors after photofragmentation of H_5O_2^+ at $\lambda = 42.1\text{nm}$ with the interaction region raised to a bias potential of $U_{\text{Bias}} = 200\text{V}$. The diagonal plots show the background-subtracted, photo-induced (defined in section 4.4) number of non-correlated counts of each detected fragment species (blue curves). The simulated center positions of the H^+ , H_2^+ and H / H_2 longitudinal momentum distribution on DET1 are indicated on plot (11) and show that this bias potential clearly makes the fragments on DET1 separate. The O^+ label on (33) marks the position where O^+ should have been observed if present.

The result of a coincidence analysis between “ H^+ and H / H_2 ” is depicted with the red curve in (11) and shows a small number of coincidences. No coincidences were found between “ H^+ and H_2^+ ” or “ H_2^+ and H / H_2 ”. In (33) coincidences are demonstrated both between “ H_3O^+ and H_2O^+ ” (black curve) and between “ H_3O^+ and OH^+ ” (green curve), while “ H_2O^+ and OH^+ ” coincidences (red curve) are not observed.

The off-diagonal plots show distribution of coincidences between detections on two detectors. The plots (12) and (21) demonstrate a coincidence between neutral, heavy fragments on DET2 ($\text{O} / \text{OH} / \text{H}_2\text{O}$) and both H^+ and H_2^+ on DET1.

A clear coincidence between H_3O^+ and $\text{O} / \text{OH} / \text{H}_2\text{O}$ is visual on plot (23) and (32), together with smaller contributions from the two pairs “ H_2O^+ and $\text{O} / \text{OH} / \text{H}_2\text{O}$ ” and “ OH^+ and $\text{O} / \text{OH} / \text{H}_2\text{O}$ ”.

With three distinguishable fragments on both DET1 and DET3 several combinations of coincidences are possible. The strongest of these is between H_3O^+ and H^+ .

In total 7 distinguishable fragments species have been identified and from these 18 combinations of coincidences have been confirmed. This gives

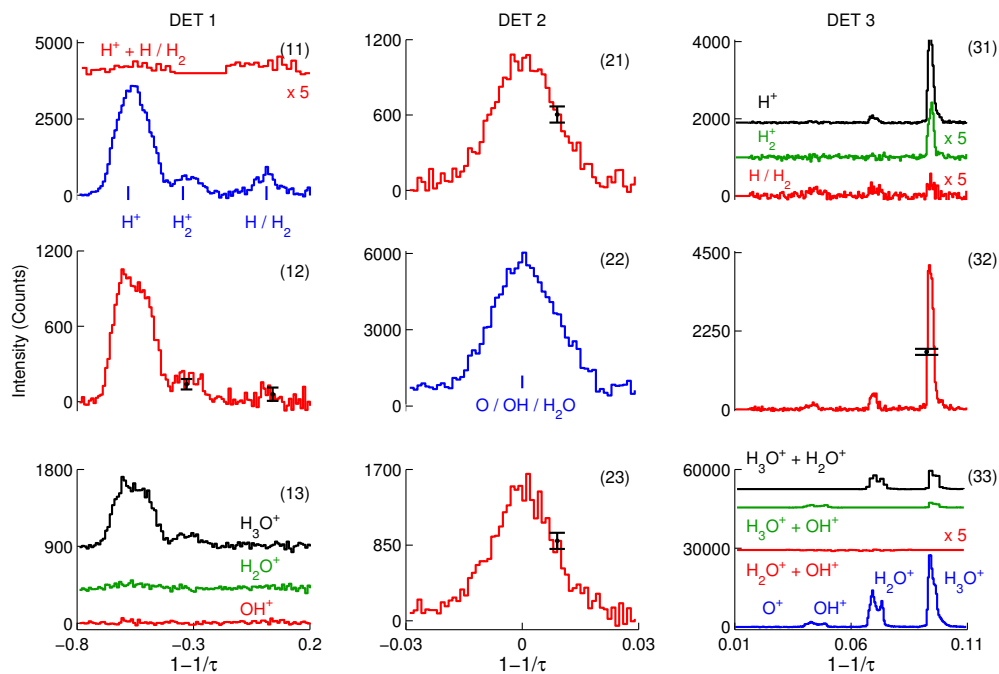


Figure 9.3: The observed intensity in a photofragmentation study of H_5O_2^+ after exposure to $\lambda = 42.1$ photons. The background-subtracted, photon-induced distributions of the uncorrelated fragments detected on DET1-3 with the interaction region at a potential of $U_{\text{Bias}} = 200\text{V}$ (blue curve) are shown in the diagonal plots. The expected, simulated momentum of H^+ , H_2^+ , H/H_2 have been marked in plot (11). Similarly the expected location of the fragments species are indicated on plot (22) and (33). The distribution of true coincidences found in an coincidence analysis are shown with the red, green and black curves. A few curves have been scales to better shown the distributions. For selected values the statistical uncertainty have been indicated. The absolute number of counts are listed in table 9.1.

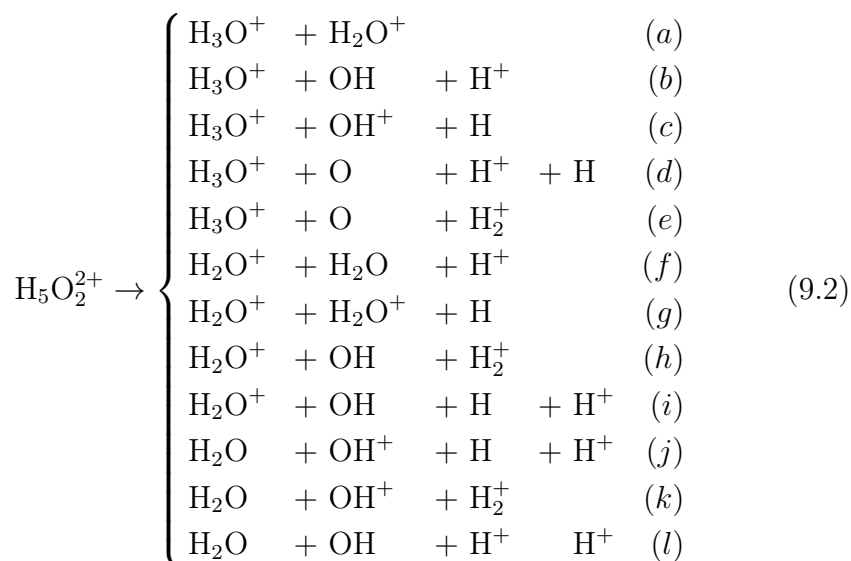
Table 9.1: Observed channels and their intensities after photofragmentation of $H_5O_2^+$ at $\lambda = 42.1 \pm 0.3\text{nm}$. Notice coincidences between “ H^+ and H_2^+ ”, “ H_2^+ and H/H_2 ” and “ H_2O^+ and OH^+ ” are not observed.

Channel	Intensity		Channel	Intensity	
H_3O^+	199311±	674	$H_2O^+ + O/OH/H_2O$	3473±	382
H_2O^+	127418±	556	$H_2O^+ + H^+$	1041±	126
OH^+	27235±	463	$H_2O^+ + H_2^+$	72±	73
$O/OH/H_2O$	146767±	1448	$H_2O^+ + H/H_2$	347±	126
H^+	62067±	408	$OH^+ + O/OH/H_2O$	1548±	281
H_2^+	8442±	282	$OH^+ + H^+$	327±	90
H/H_2	8895±	481	$OH^+ + H_2^+$	99±	53
$H_3O^+ + H_2O^+$	19278±	247	$OH^+ + H/H_2$	483±	92
$H_3O^+ + OH^+$	4957±	166	$H^+ + O/OH/H_2O$	19515±	308
$H_3O^+ + O/OH/H_2O$	26320±	492	$H^+ + H/H_2$	695±	140
$H_3O^+ + H^+$	13710±	189	$H_2^+ + O/OH/H_2O$	2716±	171
$H_3O^+ + H_2^+$	1633±	97	$H/H_2 + O/OH/H_2O$	779±	282
$H_3O^+ + H/H_2$	586±	152			

a total of 25 observable intensities to use for sorting out the branching between possible fragmentation channels. The complete list are summarized in Table 9.1

Coincidences between fragments of the same species “ $H_2O^+ + H_2O^+$ ”, $H^+ + H^+$ etc. are difficult to measure due to hardware limitations such as detector down time between successive impacts. The possible loss of the second impact renders these intensities to be underestimated if observed at all.

For 42nm photofragmentation of $H_5O_2^+$ a list of fragment pathways can be compiled from the possible combinations of the fragments detected. By allowing a total of 4 fragments only the list can be limited to the following 12 reactions.



The measured intensity of each observable in Table 9.1 can be expressed as the number of occurrences of each contributing reaction scaled by the efficiency ($\epsilon_{X,F}$) to detect a fragment F from reaction X . This efficiency will include both the efficiency of the detector and the transmission from the interaction region to the detector. The efficiency hence has to be between 0 and 1.

For the intensity of H_3O^+ on detector DET3 ($N_{\text{H}_3\text{O}^+}$) there will be a contribution of one H_3O^+ -fragment count each time one of reactions (9.2)(a-e) occur.

$$N_{\text{H}_3\text{O}^+} = \epsilon_{a,F} \cdot R_a + \epsilon_{b,F} \cdot R_b + \epsilon_{c,F} \cdot R_c + \epsilon_{d,F} \cdot R_d + \epsilon_{e,F} \cdot R_e \quad (9.3)$$

where $\epsilon_{X,F}$ is the efficiency of fragment $F = \text{H}_3\text{O}^+$ from reaction X to be detected and R_X is the number of reaction X that occurred.

Deducting the number of heavy neutrals (O/OH/H₂O) detected in coincidence with a H⁺ is a bit more complicated. The reactions (9.2)(b, d, f, i and j) will each contribute with one count per reaction each, but reaction (9.2)(l) will add several counts. Both H₂O and OH can be detected in coincidence with either one of the H⁺. Hence reaction (n) adds a contribution

of $2\epsilon_{1, H^+} + \epsilon_{1, H_2O/OH} R_n$ for both H_2O and OH . The total number of counts will then be

$$\begin{aligned}
 N_{O/OH/H_2O + H^+} = & \epsilon_{b, H^+} \cdot \epsilon_{b, OH} R_b + \epsilon_{d, H^+} \cdot \epsilon_{d, O} R_d \\
 & + \epsilon_{f, H^+} \cdot \epsilon_{f, H_2O} R_f + \epsilon_{i, H^+} \cdot \epsilon_{i, OH} R_i \\
 & + \epsilon_{j, H^+} \cdot \epsilon_{j, H_2O} R_j + (2\epsilon_{1, H^+} \cdot \epsilon_{1, H_2O} \\
 & + 2\epsilon_{1, H^+} \cdot \epsilon_{1, OH}) R_l
 \end{aligned} \tag{9.4}$$

Following this approach 25 equations can be written, one for each observable intensity. Solving this system of equations for the number of reactions that have occurred for each of the 12 reactions will directly give the branching ratio between the reactions. However this approach will result in the 12 unknown variables for the number of reactions and 39 unknown variables for the detection efficiencies. In total 25 equations with 51 unknown variables. Some assumptions will be needed to simplify the system.

One detection efficiency for each species

The detection efficiency will be assumed to be the same for all heavy neutral fragments on detector DET2 regardless from which reaction they originated

$$\epsilon_{DET2} = \epsilon_{H_2O} = \epsilon_{OH} = \epsilon_O \tag{9.5}$$

Similarly, one detection efficiency will be assumed for the heavy fragments on DET3

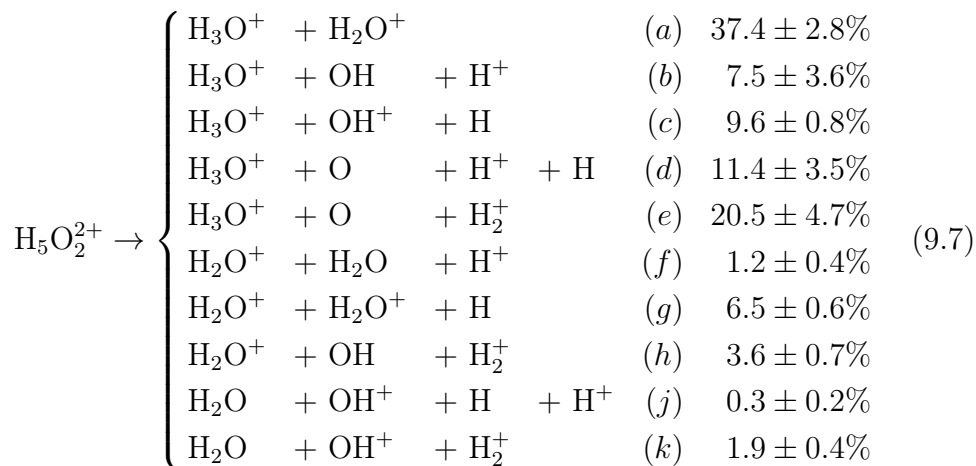
$$\epsilon_{DET3} = \epsilon_{H_3O^+} = \epsilon_{H_2O^+} = \epsilon_{OH^+} \tag{9.6}$$

Each of the species H^+ , H_2^+ and H / H_2 detected on DET1 differs in both charge as well as mass and as a consequence each species will be assumed to have an individual efficiency of detection, which is constant for all reactions (ϵ_{H^+} , $\epsilon_{H_2^+}$ and $\epsilon_{Neutral}$).

These assumptions make the system of equations solvable.

By performing a nonlinear regression where the unknown variables are estimated using iterative least squares estimation, it becomes apparent that reactions (9.2)(i) and (l) have a negligible contribution and they are eliminated from the system.

The branching ratio for the remaining system is



With the detection efficiencies

$$\begin{array}{llll} \text{H}^+ & \epsilon_{\text{H}^+} & = & 30.1 \pm 7.3\% \\ \text{H}_2^+ & \epsilon_{\text{H}_2^+} & = & 3.2 \pm 0.6\% \\ \text{H}/\text{H}_2 & \epsilon_{\text{Neutral}} & = & 2.4 \pm 0.3\% \\ \text{O}/\text{OH}/\text{H}_2\text{O} & \epsilon_{\text{DET2}} & = & 30.7 \pm 0.5\% \\ \left. \begin{array}{l} \text{OH}^+ \\ \text{H}_2\text{O}^+ \\ \text{H}_3\text{O}^+ \end{array} \right\} & \epsilon_{\text{DET3}} & = & 22.6 \pm 0.4\% \end{array} \quad (9.8)$$

The detection efficiency for DET2, DET3 and the light, neutral fragments (H and H₂) is comparable to the values obtained during the photofragmentation study of the water cation (H₂O⁺) with λ = 532nm photons, see chapter 8 (equation (8.4)). The detection efficiency for H⁺ obtained from the present study is strangely significantly higher.

The low efficiency for H₂⁺ appears remarkable. Though the masses are different for H⁺ and H₂⁺ one would expect their detection efficiencies to be in the same order. With a positive charge they will be accelerated on to the surface of the detector, increasing their kinetic energy and thereby their detection efficiency. However, with twice the mass H₂⁺ might have an insufficient velocity perpendicular to the beam direction to actually reach DET1.

One detection efficiency for each species and including relative transmissions

The assumption that all fragments of the same species have the same detection efficiency, regardless of which reaction they originated from, allows the system to be solvable. However, this cannot in general be valid. The kinetic energy released will vary between reactions and thereby the trajectory will vary. Due to geometrical obstructions like the central hole in DET1 this will affect the transmission. For light fragments a too small energy release will cause fragments to pass through the hole while for heavy fragments a too large kinetic energy release will cause fragments to impact either on DET1 or the shielded tube through it. In both cases the transmission is effected.

Introducing a relative transmission variable ($T_{X,F}$) can allow a fragment F from one reaction X to have the generalized detection efficiency scaled by a relative transmission. For instance, if H_3O^+ from reaction 9.2(a) has twice the detection efficiency of H_3O^+ from the other reactions, this could be written

$$N_{\text{H}_3\text{O}^+} = \epsilon_{\text{DET3}}(T_{a,\text{H}_3\text{O}^+} \cdot R_a + R_b + R_c + R_d + R_e), \quad (9.9)$$

with the relative transmission of H_3O^+ is set to $T_{a,\text{H}_3\text{O}^+} = 2$. The total detection efficiency of H_3O^+ from reaction (a) would then be

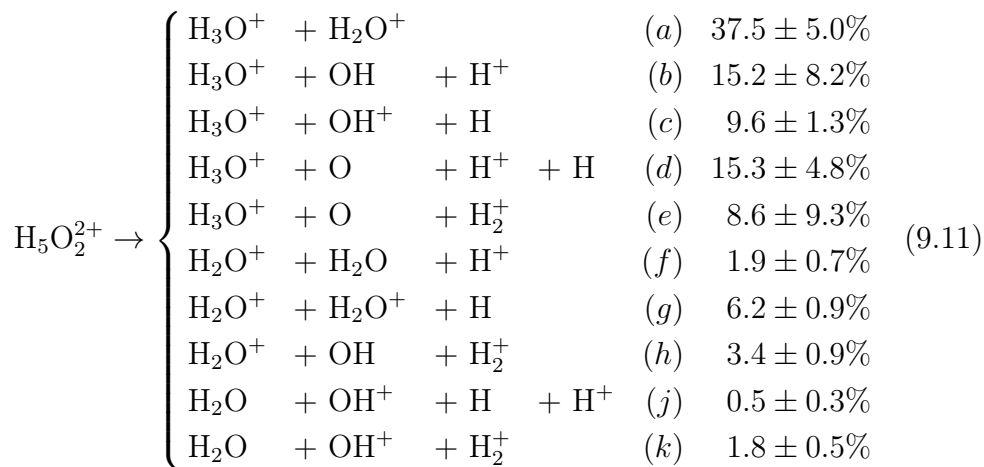
$$\epsilon_{a, \text{H}_3\text{O}^+} = \epsilon_{\text{DET3}} \cdot T_{a,\text{H}_3\text{O}^+}. \quad (9.10)$$

In this manner the detection efficiency of some fragments could be individually adjusted, while still limiting the total number of unknown variables.

With just one or two relative transmissions, the stability of the solution for the branching ratio can be tested. Introducing more than a few (~ 5) relative transmissions appears to make the system unstable and produces unphysical behaviors with negative numbers of reactions and efficiencies in the order of 10^3 .

For most fragments, the introduction of a relative transmission has only a very little effect, and presenting all the tested combinations will be more extensive than enlightening. Therefore only a single example will be given, where the effect of the transmission is noticeable.

The introduction of a relative transmission for the H_2^+ from reaction 9.2(e) will return the following branching ratio.



With the efficiency of the detectors

$$\begin{array}{llll} \text{H}^+ & \epsilon_{\text{H}^+} & = & 18.7 \pm 5.6\% \\ \text{H}_2^+ & \epsilon_{\text{H}_2^+} & = & 1.8 \pm 0.8\% \\ \text{H}/\text{H}_2 & \epsilon_{\text{Neutral}} & = & 2.2 \pm 0.3\% \\ \text{O}/\text{OH}/\text{H}_2\text{O} & \epsilon_{\text{DET2}} & = & 30.5 \pm 0.5\% \\ \left. \begin{array}{l} \text{OH}^+ \\ \text{H}_2\text{O}^+ \\ \text{H}_3\text{O}^+ \end{array} \right\} & \epsilon_{\text{DET3}} & = & 22.6 \pm 0.4\% \end{array} \quad (9.12)$$

and the relative transmission of H_2^+ from reaction 9.2(e) was found to be $T_{e, \text{H}_2^+} = 4.7 \pm 4.9$. Hence, the total detection efficiency of H_2^+ from reaction (e) was:

$$\epsilon_{e, \text{H}_2^+} = \epsilon_{\text{H}_2^+} \cdot T_{e, \text{H}_2^+} = 8.5 \pm 3.3. \quad (9.13)$$

The most noticeable differences between two sets of branching ratios (equation (9.7) and (9.11)) is the detection efficiency of H^+ and the rearrangement of intensities between the reactions 9.2(b), (d) and (e).

For the branching ratio (equation (9.11)) the detection efficiency of H^+ is comparable to the efficiency obtained for H^+ in the water cation (H_2O^+) study with $\lambda = 532\text{nm}$ photons, see chapter 8 (equation (8.4)).

9.3.2 KER of the major channel ($\text{H}_3\text{O}^+ + \text{H}_2\text{O}^+$)

For the light fragments and neutral heavy fragments the kinetic energy released (KER) and angular distribution of fragments from a reaction can be calculated for each fragment as described in section 2.5 and the KER to each fragment can be added up in order to get the total KER for the reaction.

For the charged, heavy fragments detected on DET3 the forward and upward dimension are mixed by the electrostatic mirror in a way that is hard to describe in a simple, analytical way. The generalized coordinates (ρ and τ) are defined relative to a non-deflected and non-retarded particle and, hence, become slightly arbitrary for DET3. The KER and angular distribution of fragments cannot be calculated directly with that approach for DET3.

A method to estimate the KER and angular distribution by comparing the measured TOF and impact position on DET3 to a database is described in section 6.4. The database contains initial velocities and the corresponding, simulated TOF and impact position for each entry. A unique database must be used for each mass and settings of the electrostatic mirror.

The database method will now be applied to the fragments H_3O^+ and H_2O^+ detected in coincidence, corresponding to the fragmentation pathway



only. The obtained KER and angular distribution will therefore originate from reaction 9.2(a).

The database to be used has an energy resolution of $E_{\text{KER}} = 0.2\text{eV}$ and contains 10^4 entry points for each energy, corresponding to database D in section 6.4.

The measured, uncorrelated TOF and impact position distribution for H_3O^+ can be seen in Figure 9.4 as an example of the distributions. Plot (a) displays the TOF distribution and the colors correspond to the different measuring modes: Photons&Ions (Blue curve), Ions only (red curve), Photons only (black curve) and Dark (gray curve). The measuring modes are defined in section 4.4. The contribution from Photons only and Dark mode are negligible. The background-subtracted, photon-induced signal

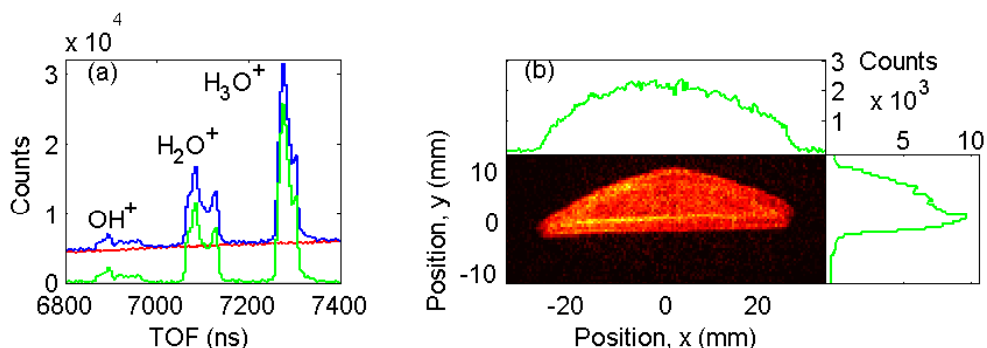


Figure 9.4: Plot (a) TOF distribution of uncorrelated impacts on DET3. The colors corresponds to the different measuring modes: Photons&Ions (Blue curve), Ions only (red curve), Photons only (black curve) and Dark (gray curve) and background subtracted photon-induced signal (green curve). Plot (b) The background-subtracted, photon-induced impact positions of H_3O^+ fragments. The shape is a result of the electrostatic mirror. The color axis is linear from zero (black) to 200 (red).

is marked with the green curve. Plot (b) illustrates the background-subtracted, photon-induced impact positions and the specific x and y distribution have been explicitly shown.

The measured, uncorrelated TOFs and impact positions on DET3 are corrected for any offset compared to the simulated TOFs and impact positions from the database. To quantify the center position the TOF, x and y distributions for both H_3O^+ and H_2O^+ a Gaussian distribution is fitted to the measured values as well as to the database entries.

The approximated KER and angular distribution for the uncorrelated H_3O^+ are shown in Figure 9.5 as a later reference for the distributions for H_3O^+ fragments in coincidence with other fragments.

By fitting a Gaussian distribution to the KER distribution, a KER of $E_{\text{KER}} = 0.6 \pm 0.4\text{eV}$ has been obtained for the uncorrelated H_3O^+ . The listed uncertainty for the KER is the standard deviation (σ) of the fit to a Gaussian distribution. In plot (b) the magenta curve illustrates the fit, and it appears like the fragments do not follow an expected angular distribution described by an asymmetry parameter (β). Several open fragmentation

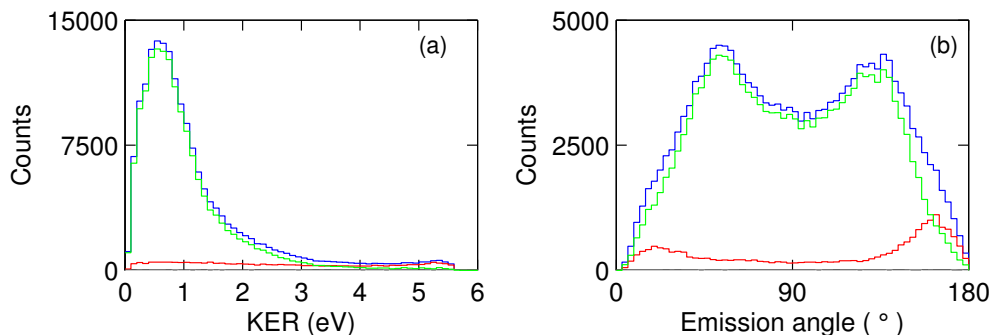


Figure 9.5: Plot (a) The KER and plot (b) the angular distribution for uncorrelated H_3O^+ fragments. The colors in plot (a) corresponds to the measure mode; Photons&Ions (Blue curve), Ions only (red curve), Photons only (black curve), Dark (gray curve) and background subtracted photon-induced signal (green curve). By fitting the KER distribution, a KER of $E_{\text{KER}} = 0.6 \pm 0.4\text{eV}$.

pathways could be an explanation.

A coincidence analysis is carried out to find the H_3O^+ and H_2O^+ fragments in coincidence. The TOFs and impact positions of the coincidence pairs are compared to the database one fragment at a time to estimate the KER and angular distribution. The results for the individual fragments are shown in Figure 9.6. The true coincidences (green curve) are found as the difference between the real coincidences (blue curve) and the random coincidences (red curve). The terms true, real and random coincidences are defined in chapter 5. Plot (a) shows the KER for the H_3O^+ fragments in coincidence with H_2O^+ fragments. The KER is found to be $E_{\text{KER}} = 0.7 \pm 0.4\text{eV}$ by fitting a Gaussian distribution to the KER distribution. The asymmetry parameter (β) has been estimated by fitting the expression for the angular distribution (equation 2.31) to the distribution of H_3O^+ shown (magenta curve) in plot (b). A value of $\beta = 1.2 \pm 0.2$ has been obtained. The ± 0.2 for the asymmetry parameter is the extent of the 0.95-confidence interval.

Figure 9.6(c,d) shows the similar distributions for the H_2O^+ fragments, in coincidence with H_3O^+ , and gives $E_{\text{KER}} = 1.0 \pm 0.4\text{eV}$ and $\beta = 1.6 \pm 0.2$.

By adding the KER of both fragments the total KER distribution for

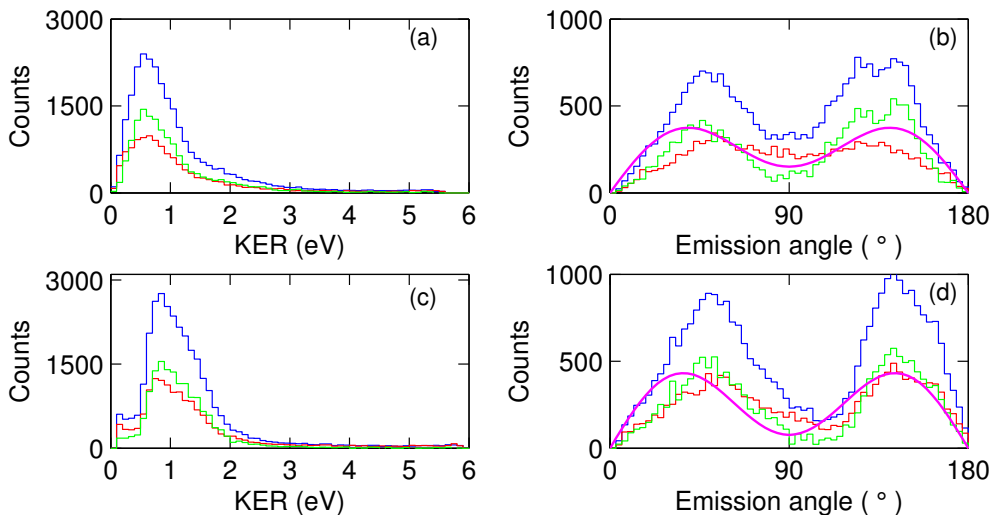


Figure 9.6: The KER and angular distribution for H_3O^+ and H_2O^+ detected in coincidence. Plot (a) and (b) represent H_3O^+ , while plot (c) and (d) shows the distributions for H_2O^+ . The distribution of true coincidences (green curve) is the difference between the real coincidences (blue curve) and the random coincidences (red curve). By fitting a Gaussian distribution to the KER distribution and the expression for the angular distribution of fragments to the angular distribution the following have been obtained. H_3O^+ : $E_{KER} = 0.7 \pm 0.4\text{eV}$ and $\beta = 1.2 \pm 0.2$. H_2O^+ : $E_{KER} = 1.0 \pm 0.4\text{eV}$ and $\beta = 1.6 \pm 0.2$.

binary breakup $H_5O_2^{2+}$ to H_3O^+ and H_2O^+ (corresponding to reaction 9.2(a)) has been obtained and is shown in 9.7. This gives a KER of $E_{KER} = 1.8 \pm 0.5\text{eV}$.

A standard deviation of $\sigma = 0.5\text{eV}$ is comparable to the standard deviation obtained in section 6.4 for simulated fragments where the KER was set to followed a Gaussian distribution with standard deviation $\sigma = 0.25\text{eV}$.

To further judge the validity of the method, the initial momentum has been calculated for the entries in the database and the corresponding momentum surface $p(\text{TOF}, x, y)$ has been interpolated. By comparing the measured TOFs and impact positions to the database the initial momentum

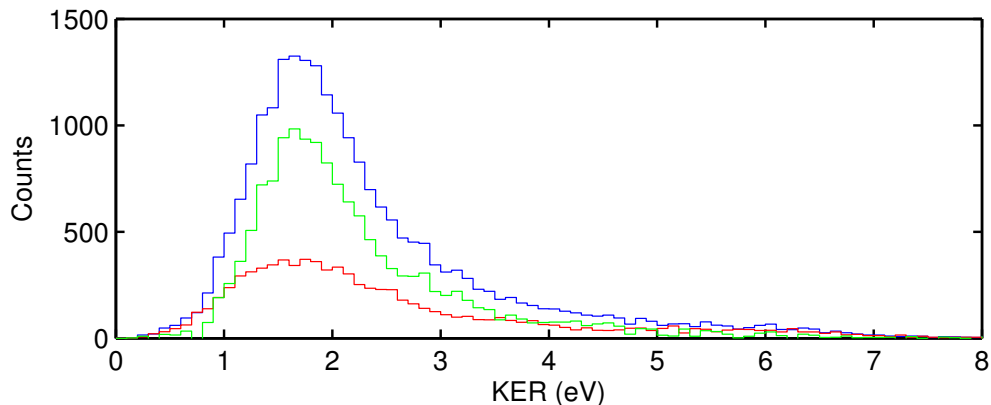


Figure 9.7: *The total KER for the binary breakup of $H_5O_2^+$ to H_3O^+ and H_2O^+ . The distribution of true coincidences (green curve) is the difference between the real coincidences (blue curve) and the random coincidences (red curve). By fitting a Gaussian distribution to the KER distribution of true coincidences the KER have been estimated to be $E_{KER} = 1.8 \pm 0.5\text{eV}$.*

of the fragments has been estimated.

In Figure 9.8 the momentum of the H_2O^+ (y-axis) have been plotted as a function of the momentum of H_3O^+ fragment (x-axis) detection in coincidence. Plot (a) shows the momentum in the forward direction (z) and indicates a primarily forward and backward motion. Plot (b) is the y -direction (up-down), while (c) is the x -direction (sideways). The uncertainty is clearly largest in the forward and y -direction, as would be expected with the electrostatic mirror mixing these coordinates. The x -momentum plot indicates a small uncertainty in the x -direction.

Overall the momentum plot in Figure 9.8 illustrates that the method is indeed capable of reproducing the momentum conservation for each dimension and underline a one-to-one mapping between initial velocities and final TOF and impact position.

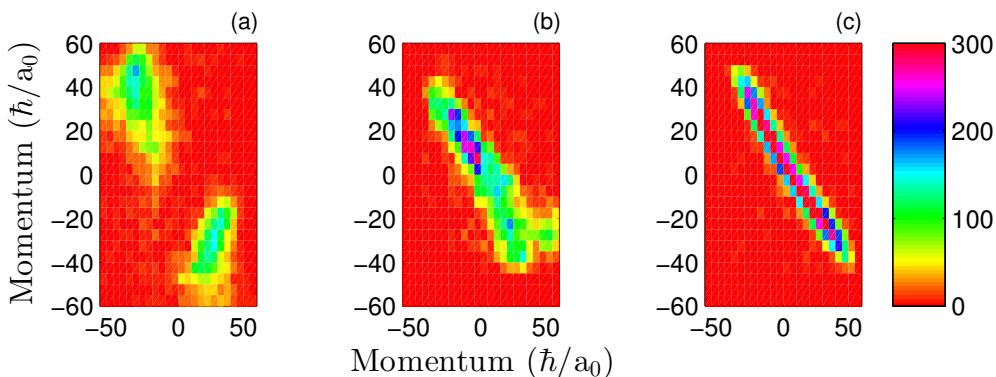
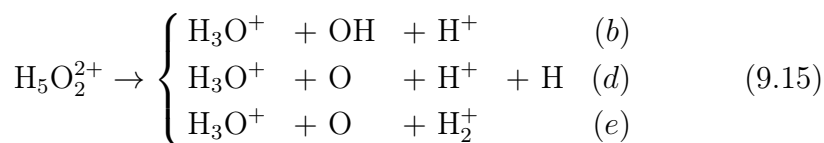


Figure 9.8: The approximated momentum of H_3O^+ (x -axis) and H_2O^+ (y -axis) detected in coincidence. Plot (a) is the forward direction, (b) the y -direction (up-down) and (c) the x -direction (sideways). Momentum conservation is apparent for all three dimensions and plot (a) suggest a primary forward and backward emission in agreement with the asymmetry parameter obtained for each fragment.

9.3.3 KER of H_3O^+ and heavy, neutral fragments in coincidence

The KER and angular distribution have been estimated for the coincidences between H_3O^+ and the heavy, neutral fragments on DET2. This corresponds to the fragmentation reactions



Where the labels refer to the fragmentation channels investigated in section 9.3.1.

The procedure is similar to the one described in section 9.3.2. The database with a energy resolution of $E_{\text{KER}} = 0.2\text{eV}$ and 10^4 entry point at each energy (corresponding to database D in section 6.4) will be used for the H_3O^+ fragments while the KER and angular distribution for the heavy, neutrals will calculated as described in section 2.5.

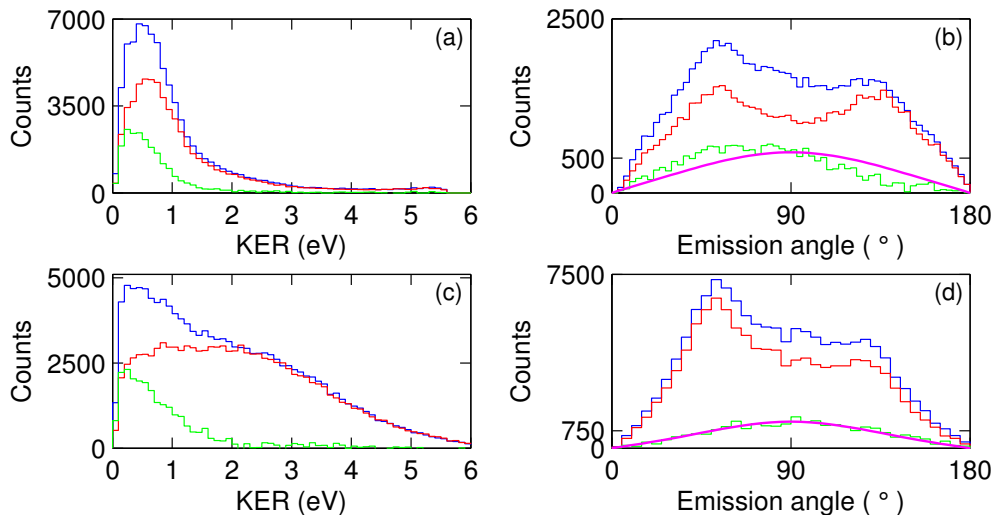


Figure 9.9: The KER and angular distribution for H_3O^+ and heavy, neutral fragments detected in coincidence. Plot (a) and (b) represent H_3O^+ , while plot (c) and (d) shows the distributions for the heavy neutrals. The distribution of true coincidences (green curve) is the difference between the real coincidences (blue curve) and the random coincidences (red curve). The KER distributions does not give a specific KER, however an upper limit can be places between $E_{KER} = 1\text{eV}$ and $E_{KER} = 1.5\text{eV}$. By fitting the expression for the angular distribution of fragments to the angular distribution the asymmetry parameter have been obtained. H_3O^+ : $\beta = -0.1 \pm 0.3$. Heavy, neutral fragments: $\beta = -0.27 \pm 0.14$.

The KER and angular distribution of the individual fragments are shown in Figure 9.9. The true coincidences (green curve) are found as the difference between the reel coincidences (blue curve) and the random coincidences (red curve). The terms true, real and random coincidences are defined in chapter 5. Plot (a) and (b) illustrates the KER an angular distributions, respectively, for H_3O^+ , while plot (c) and (d) represents the heavy, neutral fragments. The KER distribution for all fragments starts at zero energy and slopes gently towards zeros intensity around $E_{KER} = 1.5\text{eV}$.

The expression for the angular distribution (equation 2.31) has been fitted to the angular distribution of fragments and the asymmetry parameter has been estimated to $\beta = -0.1 \pm 0.3$ and $\beta = -0.27 \pm 0.14$ for H_3O^+ and the

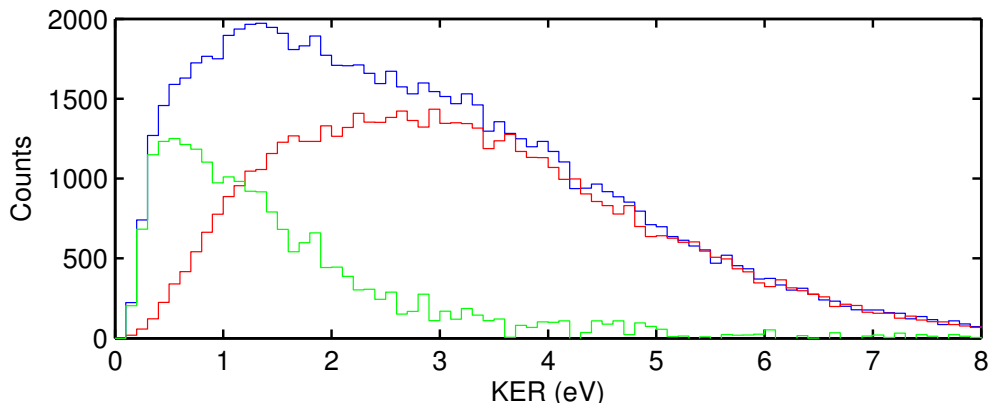


Figure 9.10: *The combined KER for a H_3O^+ and a heavy, neutral fragments in coincidence. The distribution of true coincidences (green curve) is the difference between the real coincidences (blue curve) and the random coincidences (red curve). While the KER distribution does not reveal a distinct energy, it does give an upper limits around $E_{KER} = 3\text{eV}$*

heavy neutrals, respectively. This is very close to an isotropic distribution. The fit is marked with the magenta curve. For the H_3O^+ there appears to be a deviation towards smaller angles compared to a regular fit to an angular distribution, while the directly calculated angles for the heavy, neutral fragments fits almost perfectly.

It is worth noting that the two very different approaches do indeed give similar KER and angular distributions for two heavy fragments in true coincidence with proportionally equal mass.

The KER for the individual fragments has been added to find the partial KER in the reactions and the distribution is shown in Figure 9.10. This does not give a clear KER, but it does give an upper limit to the KER around $E_{KER} = 3\text{eV}$. As only two of three/four fragments are included here, this will not be the total KER in the reaction. The total KER could perhaps have been obtain for the three body breakup via momentum conservation, but this have not been attempted.

9.4 Discussion

9.4.1 Branching ratio of fragmentation pathways

By comparing the two sets of branching ratios (equation 9.7 and 9.11), the importance of knowing the exact values for the detection efficiencies becomes apparent.

The detection efficiency of H^+ has dropped by 38% from the ratios in equation 9.7 ($\epsilon_{\text{H}^+} = 30.1 \pm 7.3\%$) to the one presented in equation 9.11 ($\epsilon_{\text{H}^+} = 18.7 \pm 5.6\%$). Similarly the general detection efficiency for H_2^+ got lower by allowing the efficiency for H_2^+ from reaction 9.2(e) to be relatively higher. The effect of the lowered detection efficiencies has been to drastically change the internal ratio between the reactions 9.2(b), (d) and (e). The other reactions appear to have been unaffected, except perhaps to have slightly increased uncertainties. From this it could be argued to simply list the combined ratio of reactions (b), (d) and (e) as $39.4 \pm 11.8\%$, in agreement with both sets of branching ratios.

This clearly shows that the detection efficiency of a fragment depends on the reaction from which it originated and the value of the efficiency for each fragment is crucial for determining the proper branching ratio. That the detection efficiencies for the branching ratios in equation 9.11 actually agrees with the ones determined in the study of the water cation (equation (8.4)), would advocate for this set of branching ratios to be preferable to determine the internal branching between reactions (b), (d) and (e).

The high ratio of fragmentation pathway containing H_3O^+ fragments, clearly indicate that the lifetime of the H_3O^+ fragments is much longer than the few micro seconds it take to reach the detector, and the water cation study (chapter 8) determined that low vibrationally excited states in the $\tilde{\text{B}}^2\text{B}_2$ excited state of the water cations has a lifetime of $\tau_{\tilde{\text{B}}^2\text{B}_2} = 198 \pm 11\mu\text{s}$. However other or higher excited states of some species might actually decay on the micro second time scale of this experiment and could account for the high number of open channels observed. To sort this out more information is needed about the internal states of the fragments.

The fragmentation of H_5O_2^+ after XUV exposure has previously been studied at TIFF at $\lambda_\gamma = 13.8\text{nm}$ [83]. At that time, detector DET3 and the

electrostatic mirror was not installed (See Figure 3.6). To keep the parent ion beam away from DET2 all charged fragments that passed through DET1 was deflected to a beam dump and lost. As a consequence the charged, heavy fragments H_mO^+ (with $m = [0, 1, 2, 3]$) was only detected on DET1 and with an acceptance in a small band of released kinetic energies only. Furthermore, the different masses of the H_mO^+ could not be distinguished. With these limitation it was argued that the major fragmentation channel was “ H_3O^+ and H_2O^+ ” in agreement with the present study. The upper limit for the size of fragmentation pathways involving H_mO^+ and a neutral fragment was estimated to be 3% as no clear coincidences were observed.

This is in contrast to the present results where the combined intensity of reaction 9.2(b), (d) and (e) are found to be 39%. However, the fragments now detected with DET3 was inaccessible at the 2010 study.

In the present study we do, however, not set any of the charged, heavy fragments on detector DET1. In the 2010 study the ion current was $I_{\text{Ion}} = 100\text{nA}$ and compared to the $I_{\text{Ion}} = 4\text{nA}$ in this study, the ion beam could have been wider than the present $w \sim 1\text{mm}$ FWHM. A wider ion beam or even a slight misalignment to the center of the interaction region would increase the change to see heavy fragments on DET1. An other explanation could be that the channel observed on DET1 in 2010 was not accessible at the photon energy in this study.

In a theoretical study of $H_5O_2^+$ by Z. Li et.al. [81,82] the fragmentational branching ratio between three channels was investigated as a function of both the photon energy and from which electronic state the fragmentation initiated.

Fragmentations initiated from the three lowest state (D_{1-3}) of $H_5O_2^{2+}$ only yielded the two body channel “ H_3O^+ and H_2O^+ ” while for fragmentations initiated from the 4th, 5th and 6th lowest state (D_{4-6}) the dominant pathway was found to be “ H_2O^+ , H_2O and H^+ ” (corresponding to reaction 9.2(f) presented here). The branching ratios are summarized and compared in table 9.2.

In the present experiment reaction 9.2(f) is among the smallest channels, $(1.9 \pm 0.7)\%$. Without knowledge of the population of the states of $H_5O_2^{2+}$ prior to fragmentation it is not possible to compare the two results directly. However, this could suggest that the dynamics are not limited to the 6 energetically lowest states valence states or that the H_3O^+ is more stable

Table 9.2: Comparison of the branching ratios calculated by Z. Li et.al. [82] and obtained in present measurement for three channels. Z. Li calculated the branching ratio for fragmentations initiated from different outer-valence ionic states (D_X , where $X = [1;6]$) of $H_5O_2^{2+}$. The branching ratio for the present work is listed as the absolute ratio obtained and the relative value for the three channels. The labels to the left refer to the reactions in equation 9.2.

	Channel	D ₁ -D ₃	D ₄	D ₅	D ₆	Rel	Abs
(a)	$H_3O^+ + H_2O^+$	100	37	13	15	58	37.5 ± 5.0
(b/c)	$H_3O^+ + OH/OH^+ + H^+/H$	0	44	76	79	39	24.8 ± 9.5
(f)	$H_2O^+ + H_2O + H^+$	0	19	11	6	3	1.9 ± 0.7
		Z. Li et al. [82]				Present work	

than predicted by the models.

9.4.2 Kinetic energy released

For the fragmentation reaction



the KER was determined to be $E_{KER} = 1.8 \pm 0.5$ eV. Comparing this value to the energy diagram of possible fragmentation pathways Figure 9.2, and assuming $H_5O_2^{2+}$ is in one of the zones marked as internal states after the ionization, this gives the possibility to end in

- H_3O^+ ($X \ ^1A_1$) + H_2O^+ ($\tilde{B} \ ^2B_2$)
- H_3O^+ ($A \ ^3A_1$) + H_2O^+ ($\tilde{X} \ ^2B_1$)
- H_3O^+ ($A \ ^3A_1$) + H_2O^+ ($\tilde{A} \ ^2A_1$)

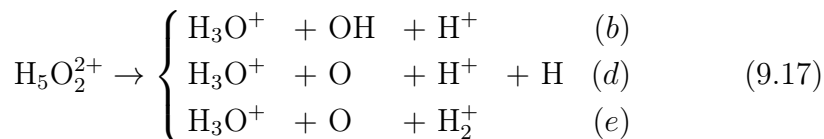
For all three pathways at least one of fragments ends up in an excited state. An indication why this is so can be found by looking at the H_3O^+ fragment. The H_3O^+ ground state has a triangular pyramid geometry at equilibrium. However, when the $H_5O_2^{2+}$ fragments the initial H_3O^+

geometry will most likely be planar. This does not conclude that H_3O^+ should be in an electronically excited state, but in this configuration the equilibrium electronic ground state might not have the lowest energy. If H_3O^+ does end in the electronic ground state at this geometry, it will be in a high vibrational state.

Z. Li et.al. [82] calculated the expected KER in a fragmentation to $\text{H}_3\text{O}^+ + \text{H}_2\text{O}^+$ from the three lowest state of $\text{H}_5\text{O}_2^{2+}$ after outer valance ionization from H_5O_2^+ . Depending on the method Z. Li found the KER interval to be $E_{\text{KER, MCTDH 7D}} = [1; 8]\text{eV}$, $E_{\text{KER, FSSH 7D}} = [1; 6]\text{eV}$ and $E_{\text{KER, FSSH 15D}} = [2; 7]\text{eV}$, where ‘‘FSSH 15D’’ was the most complete model.

With the presented KER distribution and value of $E_{\text{KER}} = 1.8 \pm 0.5\text{eV}$, this corresponds best to the lower part of the distribution from the ‘‘MCTDH 7D’’-model, but the measured KER distribution is must narrower. In fact the extend of the measured KER distribution is similar to the one obtained from a simulation with a KER following a Gaussian distribution with the standard deviation $\sigma = 0.25\text{eV}$ (See section 6.4).

For the reactions



It was not possible to derive a specific KER, but with a total of three participating pathways this was not expected. An upper limits around $E_{\text{KER}} = 3\text{eV}$ could be established. However, with this energy most of the listed combinations of possible internal states in Figure 9.2 for reaction 9.2(b), (d) and (e) are accessible.

- $\text{H}_3\text{O}^+ (\text{X } ^1\text{A}_1) + \text{OH}^+ (\text{X } ^2\Pi / \text{A } ^2\Sigma^+ / \text{B } ^2\Sigma^+) + \text{H}^+$
- $\text{H}_3\text{O}^+ (\text{X } ^1\text{A}_1) + \text{O} (^3\text{P} / ^1\text{D} / ^1\text{S}) + \text{H}^+ + \text{H} (^2\text{S}_{\frac{1}{2}})$
- $\text{H}_3\text{O}^+ (\text{X } ^1\text{A}_1) + \text{O} (^3\text{P} / ^1\text{D} / ^1\text{S}) + \text{H}_2^+ (\text{X } ^2\Sigma_g^+)$

To reduce the set of final states more information would be need.

As demonstrated in chapter 7 it is possible to perform simultaneous photoelectron-photofragmentation coincidence experiments even under

FEL conditions. The knowledge gained from such an experiment could be used to locate the internal state in $\text{H}_5\text{O}_2^{2+}$ and if a distinct KER of the electrons could be obtained, the list of possible pathway could be greatly reduced. However, the the number of particles detected in coincidence is proportional to the detection efficiency for each particle. For reaction 9.2(a) this would according to equation (2.20) be

$$N_a = N_\gamma l_I F \sigma \epsilon_{\text{H}_3\text{O}^+} \epsilon_{\text{H}_2\text{O}^+} \epsilon_{e^-} \quad (9.18)$$

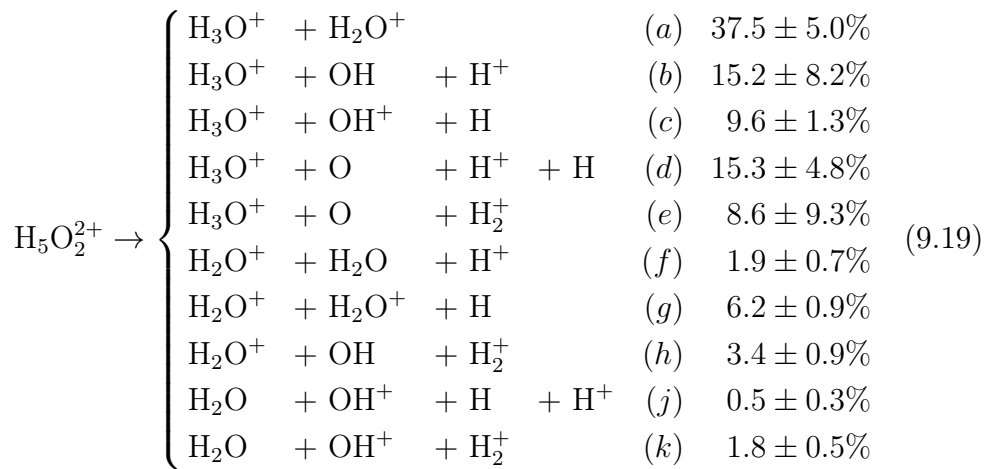
Even for an electron detection efficiency of $\epsilon_{e^-} = 0.5$, this would require twice the number of photon-ion crossings to obtain the same statistics. Sadly, the number of electrons produced by the applied photon pulse energy ($E_\gamma = 25\mu\text{J}/\text{pulse}$) completely saturated the electron detectors. Hence the photon pulse energy would have to be reduced to a level where single electron counting is possible. Lowering the photon pulse energy would directly decrease the number of photons and thereby increase the needed number of photon-ion-crossings. This would imply longer measuring times and the allotted time with access to the FEL beam is not unlimited.

With the upper limit on applicable photon pulse energy photoelectron-photofragment coincidence studies could perhaps be equally well suited at a synchrotron storage ring facility due to the much higher repetition rates, if the individual electrons and fragments can be matched with the corresponding photon pulse.

9.5 Conclusion

By using the TIFF setup and FLASH a photofragmentation study of H_5O^+ at $\lambda = 42.1\text{nm}$ have been carried out. After ionization ($\text{H}_5\text{O}^+ \rightarrow \text{H}_5\text{O}^{2+}$) the branching ratio between 10 different decay pathways have been

obtained



With the detection efficiencies

$$\begin{array}{llll} \text{H}^+ & \epsilon_{\text{H}^+} & = & 18.7 \pm 5.6\% \\ \text{H}_2^+ & \epsilon_{\text{H}_2^+} & = & 1.8 \pm 0.8\% \\ \text{H}/\text{H}_2 & \epsilon_{\text{Neutral}} & = & 2.2 \pm 0.3\% \\ \text{O}/\text{OH}/\text{H}_2\text{O} & \epsilon_{\text{DET2}} & = & 30.5 \pm 0.5\% \\ \left. \begin{array}{l} \text{OH}^+ \\ \text{H}_2\text{O}^+ \\ \text{H}_3\text{O}^+ \end{array} \right\} & \epsilon_{\text{DET3}} & = & 22.6 \pm 0.4\% \end{array} \quad (9.20)$$

and the relative transmission of H_2^+ from reaction (e) was found to be $T_{e, \text{H}_2^+} = 4.7 \pm 4.9$. Hence, the actual detection efficiency of H_2^+ from reaction (e) was:

$$\epsilon_{e, \text{H}_2^+} = \epsilon_{\text{H}_2^+} \cdot T_{e, \text{H}_2^+} = 8.5 \pm 3.3. \quad (9.21)$$

The released kinetic energy for the major channel, reaction (a), was obtained from a photofragmentation coincidence analysis to be

$$E_{\text{KER}}(\text{H}_5\text{O}_2^{2+} \rightarrow \text{H}_3\text{O}^+ + \text{H}_2\text{O}^+) = 1.8 \pm 0.5 \text{eV}. \quad (9.22)$$

while the asymmetry parameter of the fragments was found to be $\beta = 1.2 \pm 0.2$ and $\beta = 1.6 \pm 0.2$ for H_3O^+ and H_2O^+ , respectively.

From coincidence pairs of H_3O^+ and heavy, neutral fragments corresponding to the three reactions (b), (d) and (e) the distribution of the kinetic energy release was estimated. The distribution is highest for low energies and slopes almost linearly towards zero around $E_{\text{KER}} = 3\text{eV}$. This gives an upper limit for the kinetic energy release, but the information is insufficient to exactly determine the initial or final states involved let alone differentiate between the three reactions.

A photoelectron-photofragments coincidence study could greatly increase the insight in the H_5O_2^+ fragmentation process.

Summary

In this dissertation the experimental study of the decay pathways from excited states in three different ions is described. The ions are the oxygen anion (O^-), the water cation (H_2O^+) and the positively charged protonated water dimer ($H_5O_2^+$). For all three cases the decay has been initiated by photoabsorption and experiments were carried out at the TIFF ion beam setup, located as an end station to FLASH, the free electron laser (FEL) in Hamburg, Germany.

The TIFF ion beam setup comprises electron spectrometers, ion traps and fast, positional and temporal sensitive detectors, allowing simultaneously detection of electrons and positive, neutral and negative particles.

The high photon intensity from FLASH in the extreme ultra violet (XUV) and x-ray range grants a high reaction probability for each photon bunch in a crossed beam geometry, even when studying dilute gas targets with a low current of charged ions ($I_{\text{Ion}} = 1\text{-}50\text{nA}$).

The combination of the TIFF and FLASH have made it possible to simultaneously study single and double detachment from the oxygen anion at $\lambda_\gamma = 41.7\text{nm}$ and thereby determine the relative cross section to

$$\frac{\sigma_{O^0}}{\sigma_{O^+}} = 4.12 \pm 0.17. \quad (10.1)$$

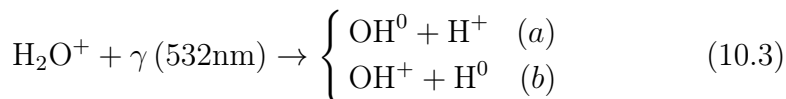
Photoelectrons and neutral oxygen detected in coincidence indicates that single electron detachment ends in the lower excited states of O^0 (3P and

¹D). The cross section for single detachment from O⁻ was found to be

$$\sigma_{O^0} = 2.1 \pm 0.6 \cdot 10^{-19} \text{cm}^2. \quad (10.2)$$

The results supplement the high precision detachment cross sections already obtained for channels with positive fragments at synchrotrons facilities.

A photodissociation at $\lambda = 532\text{nm}$ of the $\tilde{B} \ ^2B_2$ state in the water cation (H_2O^+) was found to originate from the low vibrational levels and involve single photon absorption only. Two channels were observed



with the branching ratio

$$\frac{\sigma_a}{\sigma_b} = 1.3 \pm 0.3. \quad (10.4)$$

Utilizing an ion trap the lifetime for channel (a) was found to be $\tau_{\tilde{B} \ ^2B_2} = 198 \pm 11\mu\text{s}$.

The branching ratio between 10 open channels from the photofragmentation of H_5O_2^+ at $\lambda = 42.1\text{nm}$ have been determined (see equation 9.19). The kinetic energy released in the strongest channel was determined to be

$$E_{\text{KER}}(\text{H}_5\text{O}_2^{2+} \rightarrow \text{H}_3\text{O}^+ + \text{H}_2\text{O}^+) = 1.8 \pm 0.5\text{eV}. \quad (10.5)$$

List of publications

Included in this dissertation

- L. S. Harbo, A. Becker, S. Dziarzhytski, C. Domesle, N. Guerassimova, A. Wolf, and H. B. Pedersen
Single and double electron photodetachment from the oxygen anion at 41.7 nm
Phys. Rev. A **86**, 023409 (2012)
<http://dx.doi.org/10.1103/PhysRevA.86.023409>
- L. S. Harbo, S. Dziarzhytski, C. Domesle, G. Brenner, A. Wolf and H. B. Pedersen
Lifetime of low vibrational levels of the metastable \tilde{B}^2B_2 state of H_2O^+ probed by photodissociation at 532 nm
Phys. Rev. A **89**, 052520 (2014)
<http://dx.doi.org/10.1103/PhysRevA.89.052520>

Other articles

- H. B. Pedersen, C. Domesle, L. Lammich, S. Dziarzhytski, N. Guerassimova, R. Treusch, L. S. Harbo, O. Heber, B. Jordon-Thaden, T.

Arion, M. Förstel, M. Stier, U. Hergenhahn, and A. Wolf

Photolysis of water-radical ions H_2O^+ in the xuv: Fragmentation through dicationic states

Phys. Rev. A **87**, 013402 (2013)

<http://dx.doi.org/10.1103/PhysRevA.87.013402>

- C. Domesle, S. Dziarzhytski, N. Guerassimova, L. S. Harbo, O. Heber, L. Lammich, B. Jordon-Thaden, R. Treusch, O. Heber, A. Wolf and H. B. Pedersen

Photoionization and fragmentation of H_3O^+ under XUV irradiation

Phys. Rev. A **88**, 043405 (2013)

<http://dx.doi.org/10.1103/PhysRevA.88.043405>

- H. B. Pedersen, A. Svendsen, L. S. Harbo, H. V. Kiefer, H. Kjeldsen, L. Lammich, Y. Toker and L. H. Andersen

Characterization of a new electrostatic storage ring for photofragmentation experiments

(submitted)

Bibliography

- [1] M. Born and R. Oppenheimer, *Zur Quantentheorie der Molekeln*, *Annalen der Physik* **389**, 457 (1927).
<http://dx.doi.org/10.1002/andp.19273892002>
- [2] B. H. Brandsden and C. J. Joachain, *Physics of Atoms and Molecules* (Prentice Hall, 2003), second edition.
- [3] A. G. Sage, T. A. A. Oliver, R. N. Dixon and M. N. Ashfold, *Velocity map imaging studies of the photodissociation of H₂O⁺ cations*, *Molecular Physics* **108**, 945 (2010).
<http://dx.doi.org/10.1080/00268971003596177>
- [4] H. Lefebvre-Brion and R. W. Field, *The Spectra and Dynamics of Diatomic Molecules* (Elsevier, 2004).
- [5] P. Atkins and R. Friedman, *Molecular quantum Mechanics* (Oxford University Press, 2011), fifth edition.
- [6] H. B. Pedersen *et al.*, *Neutral and charged photofragment coincidence imaging with soft x rays on molecular ion beams: Breakup of H₃O⁺ at 13.5 nm*, *Phys. Rev. A* **80**, 012707 (2009).
<http://dx.doi.org/10.1103/PhysRevA.80.012707>
- [7] P. Lambropoulos, *Topics on Multiphoton Processes in Atoms*, *Advances in atomic and molecular physics* **12**, 87 (1976).

- [8] R. N. Zare, *Photoejection Dynamics*, Mol. Photochem **4**, 1 (1972).
- [9] H. B. Pedersen *et al.*, *Photolysis of water-radical ions H_2O^+ in the xuv: Fragmentation through dicationic states*, Phys. Rev. A **87**, 013402 (2013).
<http://dx.doi.org/10.1103/PhysRevA.87.013402>
- [10] C. Domesle, S. D. N. Guerassimova, L. S. Harbo, O. Heber, L. Lammich, B. Jordon-Thaden, R. Treusch, O. Heber, A. Wolf and H. B. Pedersen, *Photoionization and fragmentation of H_3O^+ under XUV irradiation*, Physical Review A **88**, 043405 (2013).
<http://dx.doi.org/10.1103/PhysRevA.88.043405>
- [11] M. Martins, M. Wellhöfer, J. T. Hoeft, W. Wurth, J. Feldhaus and R. Follath, *Monochromator beamline for FLASH*, Review of Scientific Instruments **77** (2006).
<http://dx.doi.org/10.1063/1.2364148>
- [12] W. Ackermann *et al.*, *Operation of a free-electron laser from the extreme ultraviolet to the water window*, Nature Photonics **1**, 336 (2007).
<http://dx.doi.org/10.1038/nphoton.2007.76>
- [13] K. Tiedtke *et al.*, *The soft x-ray free-electron laser FLASH at DESY: beamlines, diagnostics and end-stations*, New Journal of Physics **11**, 023029 (2009).
<http://dx.doi.org/10.1088/1367-2630/11/2/023029>
- [14] H. B. Pedersen, L. Lammich, C. Domesle, B. Jordon-Thaden, O. Heber, J. Ullrich, R. Treusch, N. Guerassimova and A. Wolf, *Experimental investigation of dissociation pathways of cooled HeH^+ following valence electron excitation at 32 nm by intense free-electron-laser radiation*, Phys. Rev. A **82**, 023415 (2010).
<http://dx.doi.org/10.1103/PhysRevA.82.023415>
- [15] M. Dahan, R. Fishman, O. Heber, M. Rappaport, N. Altstein, D. Zafman and W. J. van der Zande, *A new type of electrostatic ion*

- trap for storage of fast ion beams*, Review of Scientific Instruments **69**, 76 (1998).
<http://dx.doi.org/10.1063/1.1148481>
- [16] J. Amann *et al.*, **Demonstration of self-seeding in a hard-X-ray free-electron laser**, NATURE PHOTONICS **6**, 693 (2012).
<http://dx.doi.org/10.1038/NPHOTON.2012.180>
- [17] **FLASH 2 homepage**, (2015).
<http://flash2.desy.de/e76656/>
- [18] **FLASH accelerator homepage**, (2015).
<http://flash.desy.de/accelerator/>
- [19] Continuum, *Minilite Datasheets* (checked 25.11.2012).
http://www.continuumlasers.com/products/pulsed_Minilite_series.asp
- [20] G. W. Goodrich and W. C. Wiley, **Continuous Channel Electron Multiplier**, Review of Scientific Instruments **33**, 761 (1962).
<http://dx.doi.org/10.1063/1.1717958>
- [21] J. Fricke, A. Müller and E. Salzborn, **Single particle counting of heavy ions with a channeltron detector**, Nuclear Instruments and Methods **175**, 379 (1980).
[http://dx.doi.org/10.1016/0029-554X\(80\)90751-X](http://dx.doi.org/10.1016/0029-554X(80)90751-X)
- [22] O. Jagutzki *et al.*, **Multiple hit readout of a microchannel plate detector with a three-layer delay-line anode**, Nuclear Science, IEEE Transactions on **49**, 2477 (2002).
<http://dx.doi.org/10.1109/TNS.2002.803889>
- [23] Roentdek, *MCP Delay Line manual*, 9.22.1003.1 edition.
<http://www.roentdek.com/manuals/>
- [24] J. L. Wiza, **Microchannel plate detectors**, Nuclear Instruments and Methods **162**, 587 (1979).
[http://dx.doi.org/10.1016/0029-554X\(79\)90734-1](http://dx.doi.org/10.1016/0029-554X(79)90734-1)

- [25] K. Norwood, A. Ali and C. Y. Ng, **A photoelectron–photoion coincidence study of H_2O , D_2O , and $(H_2O)_2$** , *The Journal of Chemical Physics* **95**, 8029 (1991).
<http://dx.doi.org/10.1063/1.461334>
- [26] **SIMION homepage**, (2015).
<http://simion.com/>
- [27] W. H. Press, S. A. Teukolsky, W. T. Vetterling and B. P. Flannery, *Numerical Recipes: The Art of Scientific Computing* (Cambridge University Press, New York, NY, USA, 2007), 3 edition, ISBN 9780521880688.
- [28] A. M. Covington *et al.*, **Correlated processes in inner-shell photodetachment of the Na^- ion**, *Journal of Physics B* **34**, L735 (2001).
<http://dx.doi.org/10.1088/0953-4075/34/22/105>
- [29] V. T. Davis *et al.*, **Photo-double detachment from the F^- ion**, *Journal of Physics B* **38**, 2579 (2005).
<http://dx.doi.org/10.1088/0953-4075/38/14/020>
- [30] A. Aguilar *et al.*, **Double photodetachment from the Cl^- ion**, *Phys. Rev. A* **69**, 022711 (2004).
<http://dx.doi.org/10.1103/PhysRevA.69.022711>
- [31] D. Hanstorp and M. Gustafsson, **Determination of the electron affinity of iodine**, *Journal of Physics B: Atomic, Molecular and Optical Physics* **25**, 1773 (1992).
<http://dx.doi.org/10.1088/0953-4075/25/8/012>
- [32] L. S. Harbo, A. Becker, S. Dziarzhytski, C. Domesle, N. Guerassimova, A. Wolf and H. B. Pedersen, **Single and double electron photodetachment from the oxygen anion at 41.7 nm**, *Phys. Rev. A* **86**, 023409 (2012).
<http://dx.doi.org/10.1103/PhysRevA.86.023409>
- [33] D. R. Lide (Ed.), *CRC Handbook of Chemistry and Physics 77th* (CRC Press, 1996), 77 edition.

- [34] L. M. Branscomb, S. J. Smith and G. Tisone, **Oxygen Metastable Atom Production Through Photodetachment**, The Journal of Chemical Physics **43**, 2906 (1965).
<http://dx.doi.org/10.1063/1.1697230>
- [35] L. C. Lee and G. P. Smith, **Photodissociation and photodetachment of molecular negative ions. VI. Ions in O₂/CH₄/H₂O mixtures from 3500 to 8600 Å**, The Journal of Chemical Physics **70**, 1727 (1979).
<http://dx.doi.org/10.1063/1.437690>
- [36] P. Hlavenka, R. Otto, S. Trippel, J. Mikosch, M. Weidemüller and R. Wester, **Absolute photodetachment cross section measurements of the O⁻ and OH⁻ anion**, The Journal of Chemical Physics **130**, 061105 (2009).
<http://dx.doi.org/10.1063/1.3080809>
- [37] D. M. Neumark, K. R. Lykke, T. Andersen and W. C. Lineberger, **Laser photodetachment measurement of the electron affinity of atomic oxygen**, Phys. Rev. A **32**, 1890 (1985).
<http://dx.doi.org/10.1103/PhysRevA.32.1890>
- [38] T. Suzuki and T. Kasuya, **Optogalvanic study of photodetachment of O⁻ near threshold**, Phys. Rev. A **36**, 2129 (1987).
<http://dx.doi.org/10.1103/PhysRevA.36.2129>
- [39] D. T. Vier and J. E. Mayer, **A Direct Experimental Determination of the Electron Affinity of Oxygen**, The Journal of Chemical Physics **12**, 28 (1944).
<http://dx.doi.org/10.1063/1.1723876>
- [40] C. Blondel, C. Delsart, C. Valli, S. Yiou, M. R. Godefroid and S. Van Eck, **Electron affinities of ¹⁶O, ¹⁷O, ¹⁸O, the fine structure of ¹⁶O⁻, and the hyperfine structure of ¹⁷O⁻**, Phys. Rev. A **64**, 052504 (2001).
<http://dx.doi.org/10.1103/PhysRevA.64.052504>
- [41] R. J. Saykally and K. M. Evenson, **Laser magnetic resonance measurement of the 2 ³P₂-2 ³P₁ splitting in atomic oxygen**,

- The Journal of Chemical Physics **71**, 1564 (1979).
<http://dx.doi.org/10.1063/1.438500>
- [42] *Nist webbook*, (2015).
<http://webbook.nist.gov>
- [43] L. S. Harbo, S. Dziarzhyski, C. Domesle, G. Brenner, A. Wolf and H. B. Pedersen, *Lifetime of low vibrational levels of the metastable B^2B_2 state of H_2O^+ probed by photodissociation at 532 nm*, Phys. Rev. A **89**, 052520 (2014).
<http://dx.doi.org/10.1103/PhysRevA.89.052520>
- [44] G. Herzberg, *H_2O^+ ions in the upper-atmosphere*, Annales de Geophysique **36**, 605 (1980).
- [45] R. P. Wayne, *Chemistry of Atmospheres* (Oxford University Press, Oxford, UK, 2000), 3rd edition.
- [46] P. A. Wehinger, S. Wyckoff, G. H. Herbig, G. Herzberg and H. Lew, *Identification of H_2O in the Tail of Comet Kohoutek*, Astrophys. J. **190**, L43 (1974).
- [47] M. A. Disanti, U. Fink and A. B. Schultz, *Spatial distribution of H_2O^+ in comet P/Halley*, Icarus **86**, 152 (1990).
[http://dx.doi.org/10.1016/0019-1035\(90\)90205-N](http://dx.doi.org/10.1016/0019-1035(90)90205-N)
- [48] D. A. Neufeld *et al.*, *Herschel/HIFI observations of interstellar OH^+ and H_2O^+ towards W49N: a probe of diffuse clouds with a small molecular fraction*, Astronomy and astrophysics **521**, L10 (2010).
<http://dx.doi.org/10.1051/0004-6361/201015077>
- [49] G. Chattopadhyay *et al.*, *Detection of OH^+ and H_2O^+ towards Orion KL*, Astronomy and astrophysics **521**, L47 (2010).
<http://dx.doi.org/10.1051/0004-6361/201015117>
- [50] V. Ossenkopf *et al.*, *Detection of interstellar oxidaniumyl: Abundant H_2O^+ towards the star-forming regions DR21, Sgr B2, and NGC6334*, A&A **518**, L111 (2010).
<http://dx.doi.org/10.1051/0004-6361/201014577>

- [51] Gerin, M. *et al.*, **Interstellar OH⁺, H₂O⁺ and H₃O⁺ along the sight-line to G10.6–0.4**, *A&A* **518**, L110 (2010).
<http://dx.doi.org/10.1051/0004-6361/201014576>
- [52] E. F. van Dishoeck and J. H. Black, **Comprehensive models of diffuse interstellar clouds - Physical conditions and molecular abundances**, *apjs* **62**, 109 (1986).
<http://dx.doi.org/10.1086/191135>
- [53] D. Smith, **The ion chemistry of interstellar clouds**, *Chemical Reviews* **92**, 1473 (1992).
<http://dx.doi.org/10.1021/cr00015a001>
- [54] D. J. Hollenbach and A. G. G. M. Tielens, **Dense photodissociation regions (PDRs)**, *Annual Review of Astronomy and Astrophysics* **35**, 179 (1997).
<http://dx.doi.org/10.1146/annurev.astro.35.1.179>
- [55] D. Hollenbach, M. J. Kaufman, E. A. Bergin and G. J. Melnick, **Water, O₂, and Ice in Molecular Clouds**, *The Astrophysical Journal* **690**, 1497 (2009).
<http://dx.doi.org/10.1088/0004-637X/690/2/1497>
- [56] P. R. Maloney, D. J. Hollenbach and A. G. G. M. Tielens, **X-Ray-irradiated Molecular Gas. I. Physical Processes and General Results**, *apj* **466**, 561 (1996).
<http://dx.doi.org/10.1086/177532>
- [57] H. H. Harris and J. J. Leventhal, **Ultraviolet emission in O⁺-H₂ reactive scattering**, *Journal of Chemical Physics* **64**, 3185 (1976).
<http://dx.doi.org/10.1063/1.432656>
- [58] H. Lew and I. Heiber, **Spectrum of H₂O⁺**, *Journal of Chemical Physics* **58**, 1246 (1973).
<http://dx.doi.org/10.1063/1.1679310>
- [59] M. Brommer, B. Weis, B. Follmeg, P. Rosmus, S. Carter, N. C. Handy, H. Werner and P. J. Knowles, **Theoretical spin-rovibronic**

- ${}^2\tilde{A}_1(\Pi_u)$ - ${}^2\tilde{B}_1$ *spectrum of the H_2O^+ , HDO^+ , and D_2O^+ cations*, The Journal of Chemical Physics **98**, 5222 (1993).
<http://dx.doi.org/10.1063/1.464922>
- [60] C. F. Jackels, *An abinitio potential energy surface study of several states of the water cation*, The Journal of Chemical Physics **72**, 4873 (1980).
<http://dx.doi.org/10.1063/1.439771>
- [61] D. Dehareng, X. Chapuisat, J. Lorquet, C. Galloy and G. Raseev, *Dynamical study of nonadiabatic unimolecular reactions: The conical intersection between the $\tilde{B} {}^2B_2$ and $\tilde{A} {}^2A_1$ states of H_2O^+* , The Journal of Chemical Physics **78**, 1246 (1983).
<http://dx.doi.org/10.1063/1.444862>
- [62] A. Lorquet and J. Lorquet, *Excited states of gaseous ions. V. The predissociation of the H_2O^+ ion*, Chemical Physics **4**, 353 (1974).
[http://dx.doi.org/10.1016/0301-0104\(74\)85003-2](http://dx.doi.org/10.1016/0301-0104(74)85003-2)
- [63] C. R. Brundle and D. W. Turner, *High Resolution Molecular Photoelectron Spectroscopy. II. Water and Deuterium Oxide*, Proc. R. Soc. A **307**, 27 (1968).
<http://dx.doi.org/10.1098/rspa.1968.0172>
- [64] J. Eland, *The predissociations of water ions*, Chemical Physics **11**, 41 (1975).
[http://dx.doi.org/10.1016/0301-0104\(75\)80036-X](http://dx.doi.org/10.1016/0301-0104(75)80036-X)
- [65] B. Das and J. W. Farley, *Observation of the visible absorption spectrum of H_2O^+* , The Journal of Chemical Physics **95**, 8809 (1991).
<http://dx.doi.org/10.1063/1.461215>
- [66] B. Weis, S. Carter, P. Rosmus, H. Werner and P. J. Knowles, *A theoretical rotationally resolved infrared spectrum for H_2O^+ ($\tilde{X} {}^2B_1$)*, The Journal of Chemical Physics **91**, 2818 (1989).
<http://dx.doi.org/10.1063/1.456951>

- [67] P. Perman and J. Brzozowski, **Direct measurements of lifetimes of excited levels in H_2O^+** , *Physics Letters A* **46**, 79 (1973).
[http://dx.doi.org/10.1016/0375-9601\(73\)90034-0](http://dx.doi.org/10.1016/0375-9601(73)90034-0)
- [68] J. Brzozowski, P. Erman and H. Lew, **Lifetimes of excited states in D_2O^+ and OD^+ and relative lifetimes between the normal and deuterated species**, *Chemical Physics Letters* **34**, 267 (1975).
[http://dx.doi.org/10.1016/0009-2614\(75\)85270-5](http://dx.doi.org/10.1016/0009-2614(75)85270-5)
- [69] G. Möhlmann, K. Bhutani, F. de Heer and S. Tsurubuchi, **Lifetimes of the vibronic $\tilde{\text{A}}^2\text{A}_1$ states of H_2O^+ and of the $^3\Pi_i$ ($\mu' = 0$) state of OH^+** , *Chemical Physics* **31**, 273 (1978).
[http://dx.doi.org/10.1016/0301-0104\(78\)87042-6](http://dx.doi.org/10.1016/0301-0104(78)87042-6)
- [70] J. E. Reutt, L. S. Wang, Y. T. Lee and D. A. Shirley, **Molecular beam photoelectron spectroscopy and femtosecond intramolecular dynamics of H_2O^+ and D_2O^+** , *The Journal of Chemical Physics* **85**, 6928 (1986).
<http://dx.doi.org/10.1063/1.451379>
- [71] H. B. Pedersen, D. Strasser, O. Heber, M. L. Rappaport and D. Zajfman, **Stability and loss in an ion-trap resonator**, *Phys. Rev. A* **65**, 042703 (2002).
<http://dx.doi.org/10.1103/PhysRevA.65.042703>
- [72] G. Zundel and H. Metzger, **Energiebänder der tunnelnden Überschuss-Protonen in flüssigen Säuren. Einen IR-spektroskopische Untersuchung der Natur der Gruppierungen H_5O_2^+** , *Zeitschrift für Physikalische Chemie Neue Folge* **58**, 225 (1968).
- [73] M. Eigen, **Proton Transfer, Acid-Base Catalysis, and Enzymatic Hydrolysis. Part I: ELEMENTARY PROCESSES**, *Angewandte Chemie International Edition in English* **3**, 1 (1964).
<http://dx.doi.org/10.1002/anie.196400011>
- [74] Z. Sternovsky, M. Horanyi and S. Robertson, **Collision cross sections of small water clusters**, *PHYSICAL REVIEW A* **64**, 023203

- (2001).
<http://dx.doi.org/10.1103/PhysRevA.64.023203>
- [75] D. Marx, M. E. Tuckerman, J. Hutter and M. Parrinello, ***The nature of the hydrated excess proton in water***, *Nature* **397**, 601 (1999).
<http://dx.doi.org/10.1038/17579>
- [76] Y. Xie, R. B. Remington and H. F. Schaefer, ***The protonated water dimer: Extensive theoretical studies of H₅O⁺2***, *The Journal of Chemical Physics* **101**, 4878 (1994).
<http://dx.doi.org/10.1063/1.467409>
- [77] E. S. Stoyanov and C. A. Reed, ***IR Spectrum of the H O + Cation in the Context of Proton Disolvates L-H+-L***, *J. Phys. Chem. A* **110**, 12992 (2006).
<http://dx.doi.org/10.1021/jp062879w>
- [78] G. Niedner-Schatteburg, ***Infrared Spectroscopy and Ab Initio Theory of Isolated H₅O⁺: From Buckets of Water to the Schrödinger Equation and Back***, *Angew. Chem. Int. Ed.* **47**, 1008 (2008).
<http://dx.doi.org/10.1002/anie.200703555>
- [79] M. Baer, D. Marx and G. Mathias, ***Theoretical Messenger Spectroscopy of Microsolvated Hydronium and Zundel Cations***, *Angew. Chem. Int. Ed.* **49**, 7346 (2010).
<http://dx.doi.org/10.1002/anie.201001672>
- [80] U. F. Ndongmou Taffoti, P. M. Dinh, P. G. Reinhard, E. Suraud and Z. P. Wang, ***Exploration of dynamical regimes of irradiated small protonated water clusters***, *The European Physical Journal D* **58**, 131 (2010).
<http://dx.doi.org/10.1140/epjd/e2010-00055-2>
- [81] Z. Li, M. E.-A. Madjet, O. Vendrell and R. Santra, ***Correlated Dynamics of the Motion of Proton-Hole Wave Packets in a Photoionized Water Cluster***, *Phys. Rev. Lett.* **110**, 038302 (2013).
<http://dx.doi.org/10.1103/PhysRevLett.110.038302>

- [82] Z. Li, M. E.-A. Madjet and O. Vendrell, ***Non-Born-Oppenheimer dynamics of the photoionized Zundel cation: A quantum wavepacket and surface-hopping study***, J. Chem. Phys. **138**, 094313 (2013).
<http://dx.doi.org/10.1063/1.4793274>
- [83] L. Lammich *et al.*, ***Fragmentation Pathways of $\text{H}^+(\text{H}_2\text{O})_2$ after Extreme Ultraviolet Photoionization***, Phys. Rev. Lett. **105**, 253003 (2010).
<http://dx.doi.org/10.1103/PhysRevLett.105.253003>
- [84] S. Roszak, ***An ab initio configuration interaction study of deprotonation and dehydrogenation pathways of the hydronium cation***, Chemical Physics Letters **250**, 187 (1996).
[http://dx.doi.org/10.1016/0009-2614\(95\)01452-7](http://dx.doi.org/10.1016/0009-2614(95)01452-7)